PROBABILISTIC AND GEOMETRIC SHAPE BASED SEGMENTATION METHODS

By

Melih Seref Aslan
B.Sc. 2000, Electronics Engineering, Fatih University
M.Sc. 2005, ECE, University of South Alabama

A Dissertation
Submitted to the Faculty of the
J. B. Speed School of Engineering of the University of Louisville
in Partial Fulfillment of the Requirements
for the Degree of

Doctor of Philosophy

Department of Electrical and Computer Engineering
University of Louisville
Louisville, Kentucky

May 2012

PROBABILISTIC AND GEOMETRIC SHAPE BASED SEGMENTATION METHODS

By

Melih Seref Aslan
B.Sc. 2000, Electronics Engineering, Fatih University
M.Sc. 2005, ECE, University of South Alabama

A Dissertation Approved on

_____

by the Following Reading and Examination Committee:

_____
Aly A. Farag, Ph.D., Dissertation Director

_____
Ben Arnold, Ph.D.

_____
Tamer Inanc, Ph.D.

_____
Chin Ng, Ph.D.

_____
Hossam Abdelmunim, Ph.D.

DEDICATION

To my wife, Sule, who supports me during the journey of this study, and to my son, Burak Selim.

ACKNOWLEDGMENTS

I would like to express my deepest gratitude to my advisor Dr. Aly A. Farag for his guidance, support, and encouragement to pursue a Ph.D. degree in the medical imaging field. His motivation lies in the sentence that ”Sky is the limit”.

I would like to thank all my dissertation committee members Dr. Ben Arnold, Dr. Chin Ng, Dr. Tamer Inanc, and Dr. Hossam Abdelmunim for all the fruitful and valuable discussions we had regarding this research work. Special thanks go to Dr. Asem Ali, Dr. Dongqing Chen and Dr. Rachid Fahmi not only for their friendship, but also their great assistance and fruitful discussions.

Also, I would like to thank to Mr. Mike Miller, Mr. Chuck Sites and all CVIP Lab members for their friendship and assistance. I will miss Dr. Ham Rara, Dr. Moumen Elmelegy, Mr. Eslam Mostafa, Mr. Ahmed Shalaby, Mr. Cambron Cartor, Mr. Roserio Pusatery, Mr. Aly Abdelrahim, Mr. Mostafa Abdelrahman, Mr. Ahmed El Barkouky, Mr. Ali Mahmoud, Mr. Travis Gault, Ms. Shireen Elhabia, Ms. Marwa Ismail, and Ms. Amal Farag.

Very special thanks go to my father *Ahmet*, my mother *Neceha*, my brother *Necdet*, my sister, *Neslihan*, my wife *Sule*, and her family for their encouragement and prayers. My special love goes to my dearest son, *Burak Selim*. Finally, words cannot describe how I am indebted to my wife and my family for their pain, suffering and sacrifices made during the journey of this study.

ABSTRACT

PROBABILISTIC AND GEOMETRIC SHAPE BASED SEGMENTATION METHODS

Melih S. Aslan

April, 26, 2012

Image segmentation is one of the most important problems in image processing, object recognition, computer vision, medical imaging, etc. In general, the objective of the segmentation is to partition the image into the meaningful areas using the existing (low level) information in the image and prior (high level) information which can be obtained using a number of features of an object. As stated in [1, 2], the human vision system aims to extract and use as much information as possible in the image including but not limited to the intensity, possible motion of the object (in sequential images), spatial relations (interaction) as the existing information, and the shape of the object which is learnt from the experience as the prior information. The main objective of this dissertation is to couple the prior information with the existing information since the machine vision system cannot predict the prior information unless it is given.

To label the image into meaningful areas, the chosen information is modelled to fit progressively in each of the regions by an optimization process. The intensity and spatial interaction (as the existing information) and shape (as the prior information) are modelled to obtain the optimum segmentation in this study. The intensity information is modelled using the Gaussian distribution. Spatial in-

teraction that describes the relation between neighboring pixels / voxels is modeled by assuming that the pixel intensity depends on the intensities of the neighboring pixels. The shape model is obtained using occurrences of histogram of training shape pixels or voxels. The main objective is to capture the shape variation of the object of interest. Each pixel in the image will have three probabilities to be an object and a background class based on the intensity, spatial interaction, and shape models. These probabilistic values will guide the energy (cost) functionals in the optimization process.

This dissertation proposes segmentation frameworks which has the following properties: i) original to solve some of the existing problems, ii) robust under various segmentation challenges, and iii) fast enough to be used in the real applications. In this dissertation, the models are integrated into different methods to obtain the optimum segmentation: 1) variational (can be considered as the spatially continuous), and 2) statistical (can be considered as the spatially discrete) methods.

The proposed segmentation frameworks start with obtaining the initial segmentation using the intensity / spatial interaction models. The shape model, which is obtained using the training shapes, is registered to the image domain. Finally, the optimal segmentation is obtained using the optimization of the energy functionals. Experiments show that the use of the shape prior improves considerably the accuracy of the alternative methods which use only existing or both information in the image. The proposed methods are tested on the synthetic and clinical images / shapes and they are shown to be robust under various noise levels, occlusions, and missing object information. Vertebral bodies (VBs) in clinical computed tomography (CT) are segmented using the proposed methods to help the bone mineral density measurements and fracture analysis in bones. Experimental results show that the proposed solutions eliminate some of the existing problems in the VB segmentation. One of the most important contributions of this study is to offer a segmentation framework which can be suitable to the clinical works.

TABLE OF CONTENTS

DEDICATION iii
ACKNOWLEDGMENTS iv
ABSTRACT v
TABLE OF CONTENTS vii
LIST OF TABLES x
LIST OF FIGURES xi
List of Algorithms xx
CHAPTER
I. INTRODUCTION 1
A. Problem Statement 4
1. Energy Formulation Using Bayes' Rule 6
B. Shape Representation 7
C. Shape Based Segmentation 8
D. Shape/Image Registration 11
E. Related Works 13
1. Variational (Spatially Continuous Methods) Approach . . . 14
2. Statistical (Spatially Discrete) Approach 15
3. Algorithms on Vertebral Body Segmentation 16
F. Contributions of this Dissertation 16
G. Dissertation Organization 18
II. A PROBABILISTIC SHAPE-BASED SEGMENTATION METHOD USING LEVEL SETS 19
A. General Level Sets Formulation and Derivation 19
B. Related Works 21
C. Contribution of This Study 25
D. Method 26
1. Shape Model Reconstruction 26
a. Shape Representation 26
b. Principle Component Analysis (PCA) on the Training Shapes (Offline) 28
c. The Dynamic Shape Based Probability Density Function 29
2. Intensity Segmentation 35
3. Embedding Shape Model with the Image Domain 38
E. Experiments and Discussion 40
1. Experiments on Synthetic Shapes 41
2. Experiments on Vertebral Body Images 42
a. Validation Using the Phantom 42
b. Experimental Results on VB 54
F. Conclusion 54

III. STATISTICAL SHAPE BASED SEGMENTATION OF VERTEBRAL BODIES . . . 61
A. Spinal Bone Anatomy and Osteoporosis . . . 61
1. Anatomy of the Spine Column . . . 61
2. What is osteoporosis? . . . 61
3. How to Diagnose Osteoporosis . . . 65
B. Introduction . . . 65
C. Motivation . . . 72
D. Contribution of this Study . . . 72
E. Overview of Intensity, Spatial Interaction, and Shape Models . . . 73
a. Intensity Model . . . 74
b. Spatial Interaction Model . . . 75
c. Shape Model . . . 76
F. Proposed Framework . . . 76
1. CT Data Information . . . 79
2. Shape Model Construction (Training) . . . 79
a. The Registration of Training Shapes . . . 79
b. Shape Modeling . . . 80
3. Spine Cord Extraction . . . 83
4. Vertebrae Separation . . . 85
a. Manual . . . 85
b. Automatic . . . 90
5. Segmentation . . . 92
a. Initial Segmentation . . . 93
b. Embedding the Shape Model . . . 93
c. Final Energy Minimization Using Three Models: Intensity, Spatial Interaction, and Shape . . . 94
G. Experiments and Results . . . 98
1. CT Data Information . . . 98
2. Segmentation Measurements . . . 99
3. Validation Using the Phantom . . . 100
4. Results on Clinical CT Images . . . 106
H. Discussion and Conclusion . . . 114
IV. EXTENSION STUDY OF SEGMENTATION USING GRAPH CUTS . 117
A. Method . . . 117
a. 3D Shape Model Construction (Offline): . . . 119
1. Initial Segmentation . . . 123
2. Variational Registration Approach . . . 124
3. Statistical Segmentation Approach . . . 125
B. Experiments and Discussion . . . 128
V. CONCLUSION AND FUTURE WORK . . . 134
A. What is Accomplished . . . 134

B. Directions to Future Works 135
REFERENCES 137
APPENDIX
I. 144
1. Spatial Interaction Model 144
CURRICULUM VITAE 149
A. CONTACT INFORMATION 149
B. RESEARCH INTERESTS 149
C. EDUCATION 149
D. HONORS AND AWARDS 150
E. PUBLICATIONS 150
F. REVIEWER 151
G. SOFTWARE PROGRAMMING 151
H. BIOGRAPHY 151
I. LANGUAGES 152
J. MEMBERSHIP 152

LIST OF TABLES

TABLE . PAGE

1. Average segmentation accuracy of the proposed VB segmentation on 252 CT images (including 12 ESP images). The size of each image is 512x512 (After each VB is detected, the size is reduced to 120x120). . . 53
2. Classification of clinical data sets used in the experiments: There are totally 18 data sets in the data base. Class A, B, and C have 7, 5, and 6 data sets, respectively. 107
3. Segmentation Results of Each Data Class Based on Different Measures. (The measurements are based on data sets with $120\mathbf{x}120\mathbf{x}Z$ size where Z represents number of slices.) 108
4. Relative Comparison 109
5. Average Execution Time of the Framework: The average time calculation is based on 12 VBs / 96 CT slices.) 113
6. Comparison of two proposed methods described in Chapter 2 and 3 . 114
7. Graph Weights 129
8. Accuracy and time performance of the VB segmentation on 10 data sets. . . . 132

LIST OF FIGURES

FIGURE . PAGE

1. Examples of the image segmentation into the meaningful areas. The blue color shows the contour of the desired segmentation region. . . . 2
2. An image of horses in a background of partially snowy ground. (This image is ascribed to Bev Doolittle.) 2
3. An example for the shape definition. The shape in the figure is a duck even the shape is translated, rotated, and scaled. 3
4. An example for the shape registration. After the source and target shapes are registered, the shape variability is modeled. 3
5. An example segmentation with coupling the existing and prior information. The gray level image has problems such as noise and occlusion. The intensity modeling is not enough only to solve the noise and occlusion problems. The spatial interaction coupling with the intensity information is able to solve the noise but not the occlusion problem. Shape modeling coupling with the existing information is able to solve both the noise and occlusion problems. 9
6. Examples of the image segmentation into the meaningful areas when the image has occlusion, missing information, and noise problems. The blue color shows the contour of the desired segmentation region. 10
7. Registration example of a point from the source to the target image. . . 12
8. The general framework is shown. The steps can listed as follows: 1) Obtain shape projections to define the shape variability. 2) The intensity based segmentation. The yellow contour shows the automatic segmentation region. 3) The shape based segmentation with iterative shape reconstruction. 27
9. An example representation of signed distance function. (a) A vertebral body (VB) shape, (b) signed distance function as an image intensity representation, (c) level set representation of SDF. 27
10. The training VB images. In this experiment, 80 VB shapes which are obtained from 20 different patients and different regions (such as cervical, thoracic, and lumbar spine bone sections) are used. These images are processed using the PCA method to obtain most important projections which are enough to represent the shape variation in the vertebral body. 30
11. Projections of 80 training VB shapes shown in Figure 43. First to last rows (from $i = 1$ to $i = 4$) correspond to the projected shapes of the first to fourth strongest eigenvector representation. Projected shapes with corresponding eigenvalues are shown in (a) $\phi^t_{\{i,-3\}} = \phi_M + \mathbf{Ub}_{\{i,-3\}}$, (b) $\phi^t_{\{i,-1\}} = \phi_M + \mathbf{Ub}_{\{i,-1\}}$, (c) $\phi^t_{\{i,0\}} = \phi_M + \mathbf{Ub}_{\{i,0\}}$, (d) $\phi^t_{\{i,1\}} = \phi_M + \mathbf{Ub}_{\{i,1\}}$, and (e) $\phi^t_{\{i,3\}} = \phi_M + \mathbf{Ub}_{\{i,3\}}$. 30

12. Implicit shape representation of 1st projections. Shapes with corresponding eigenvalues are shown in (a) $\phi^t_{\{1,-3\}}$, (b) $\phi^t_{\{1,-1\}}$, (c) $\phi^t_{\{1,0\}}$, (d) $\phi^t_{\{1,1\}}$, and (e) $\phi^t_{\{1,3\}}$. The first row shows the binary images. The second and third rows show the SDF shape representation in 2D and 3D, respectively. 31
13. Sampling up to 3 standard deviations (from $\mathbf{b}_{\{i,-3\}}$ to $\mathbf{b}_{\{i,3\}}$) along the first four principle components (p.c.) (where $i = \{1, 2, 3, 4\}$ for the first four p.c.) from the mean for a set of jet airplane, number "four", and 80 training vertebral body (VB) shapes. 32
14. The shape models of each data that are used in the experiments. The green color shows the background region which does not have any intersection with any training shape. The blue color shows the object region which is the intersection of all projected training shapes. (i) The gray color represents the variability region that can be described as the union of all projected training shapes minus the intersection of those shapes. In this variability region, the object and background probabilistic shapes are defined. (ii) The red color shows the average shape ($\phi_{\mathbf{p}}$). (iii) The object (p^s_o) and (iv) background (p^s_b) shapes are modelled in the variability region which the pixel values are defined in $(0 : 1)$. 33
15. The constructed object (p^s_o in the first row) and background (p^s_b in the second row) models. The red squares show the same location in both images. The numbers shown in the right side are the pixel information at each pixel $\mathbf{x}$ in the red square. 34
16. An example of the initial labeling. (a) Original CT image, (b) detection of the VB region, (c) the initial labeling, $\mathbf{f}^*$, and (d) the SDF of the initial segmentation ($\mathbf{f}^*$) which is used in the registration phase. 37
17. Shape based segmentation results on another subject at each iteration with different initialization. The results at each iteration are shown in (a)-(d). (First row) The source shape is initialized with $\theta = 30^o$ rotation degrees. (Second row) The source shape is initialized with $\theta = -30^o$ rotation degrees and $s_x = 1.2,\ s_y = 1.2$ scaling factors. (Third row) The source shape is initialized with $s_x = 1.2,\ s_y = 1.2$ scaling factors and $t_x = 20,\ t_y = -20$ translation factors. 43
18. Example 1: The effects of each component of Eq. 37 on different jet shapes with different initializations. (a) The initialization of the shape model. (b) The results using only the first term. (c-Proposed) The result using all terms. 44
19. Example 2: The effects of each component of Eq. 37 on a jet shape with different initializations. (a) The initialization of the shape model. (b) The results using only the first term. (c-Proposed) The result using all terms. 45

20. Example 3: Segmentation results of a synthetic jet airplane images with different missing information and initializations. (a) The only intensity based segmentation results. (b) Different shape model initialization. (c) The results using only the first term of Eq. 37. (d) The segmentation of the proposed method (the red and yellow colors show the contour of the ground truth shape region, and the contour of the automatically segmented region, respectively). 46
21. Example 4: Segmentation results of a synthetic jet airplane images with different missing information and initializations. (a) The only intensity based segmentation results. (b) Different shape model initialization. (c) The results using only the first term of Eq. 37. (d) The segmentation of the proposed method (the red and yellow colors show the contour of the ground truth shape region, and the contour of the automatically segmented region, respectively). 47
22. Example 5: (number ”4”): Segmentation results on a synthetic number ”4” with occlusions and different shape initializations. (a) The image with occlusions. (b) The segmentation results using only intensity information. (c) Different shape model initializations. (d-Proposed) The result of the proposed method (the red and yellow colors show the contour of the ground truth shape region, and the contour of the automatically segmented region, respectively). 48
23. Example comparison 1: Comparison with two closest works described in [14, 67]. Testing shapes with (i) homogeneous and (ii-iv) inhomogeneous scaling factors. (i) $s_x = 1.0, s_y = 1.0$, (ii) $s_x = 0.7 s_y = 1.3$, (iii) $s_x = 1.2, s_y = 0.7$, (iv) $s_x = 0.4, s_y = 0.7$. (The red and yellow colors show the contour of the ground truth shape region, and the contour of the automatically segmented region, respectively). 49
24. Example comparison 2: Comparison with two closest works described in [14, 67]. Testing shapes with (i) homogeneous and (ii-iv) inhomogeneous scaling factors. (i) $s_x = 1.0, s_y = 1.0$, (ii) $s_x = 0.7 s_y = 1.3$, (iii) $s_x = 1.2, s_y = 0.7$, (iv) $s_x = 0.4, s_y = 0.7$ (the red and yellow colors show the contour of the ground truth shape region, and the contour of the automatically segmented region, respectively). 50
25. Example comparison 3: Comparison with two closest works described in [14, 67]. Testing shapes with (i) homogeneous and (ii-iv) inhomogeneous scaling factors. (i) $s_x = 1.0, s_y = 1.0$, (ii) $s_x = 0.7 s_y = 1.3$, (iii) $s_x = 1.2, s_y = 0.7$, (iv) $s_x = 0.4, s_y = 0.7$ (the red and yellow colors show the contour of the ground truth shape region, and the contour of the automatically segmented region, respectively). 51
26. (a) A vertebra in an axial CT. (b) Regions of the vertebra: The blue color shows the VB region which is the region of interest to be segmented. Spinal processes and ribs which should not be included in the BMD measurements are shown. As seen in the figure, the separation of the ribs and processes are not an easy task. This problem is solved by the proposed method. 52

27. Segmentation results of an ESP CT slice with (a) no noise, noise variances (b) σ_n^2=0.1, (c) σ_n^2=0.25, and (d) σ_n^2=0.5. The first row shows the original images. The second and third row show the results of the AAM and the proposed method, respectively. The yellow color shows the contour of the segmented region. As seen in the figure, the proposed method is robust under various noise levels. 53
28. Segmentation results of clinical CT images. (a) Only intensity based segmentation results. (b) Different initialization of the shape model. (c) The proposed segmentation results (the red color shows the contour of the ground truth shape region, the yellow color shows the contour of the automatically segmented region). 55
29. Segmentation results of clinical CT images. (a) Only intensity based segmentation results. (b) Different initialization of the shape model. (c) The proposed segmentation results (the red color shows the contour of the ground truth shape region, the yellow color shows the contour of the automatically segmented region). 56
30. Segmentation results of clinical CT images. (a) Only intensity based segmentation results. (b) Different initialization of the shape model. (c) The proposed segmentation results (the red color shows the contour of the ground truth shape region, the yellow color shows the contour of the automatically segmented region). 57
31. Segmentation results on the clinical VB images with various shape initializations. In this figure, i) shows the shape initialization, ii) the results of AAM [9] when the shape model is initialized at the same location as shown in (i), and iii) shows the proposed segmentation results. (The red and yellow colors show the contour of the ground truth of objects and the contour of the segmented region, respectively.) 58
32. 3D result of the segmentation results. (a) 3D CT data before the segmentation. (b)-(c) The segmentation results on different views. As seen in the figure, the proposed method is able to extract the spinal processes, ribs, and other surrounding soft tissues. It should be noted that adjacent VBs are assumed to be separated in advance. 59
33. The sagittal view of the spine column. There are five regions of the spine column: cervical, thoracic, lumbar, sacrum, and coccyx. 62
34. Differences of the healthy and osteoporosis bone. (This image is adopted from [72].) 63
35. Three different bone tissues. (a) Healthy, (b) osteopenia, and (c) osteoporosis bones. (These images are adopted from [73].) 64
36. Based on the Surgeon general report (a) shows the current and estimated the number of people having low bone mass in 2002, 2010, and 2020, and (b) shows several consequences of having low bone mass. (These images are adopted from [74]). 64
37. (a) Low bone mass (osteopenia) and osteoporosis cause severe fractures on vertebrae, hip, and wrist. (b) With increasing age, the incident of vertebral fractures are higher than the incidents of hip and wrist. (These images are adopted from [74] and [75], respectively). . . 65

38. More examples for the VB region definition. i) The original CT images show different vertebrae. ii) The blue contour shows vertebral body which is the region of interest. VBs are required to be separated from the ribs and spinal processes which have similar gray level information. 66
39. Typical challenges for vertebrae segmentation. (a) Inner boundaries. (b) Osteophytes. (c) Bone degenerative disease. (d) Double boundary. 71
40. More challenges on sagittal and coronal axes such as weak bone edges, osteophytes, and low resolution (from the left column to the right column, respectively). 71
41. Two different CT data sets. (a) The resolution is good, hence separation and segmentation of a VB is straightforward. (b) The resolution is low which makes the separation and segmentation of a VB difficult. 72
42. The general segmentation framework. (Prior to this framework, it is required to obtain the shape model). In the first phase, the spinal cord is extracted, processes, and ribs roughly using the Matched filter. Also, the data size is reduced to minimize the execution time. In the second phase, the VBs are separated with two choices: i) manual, ii) automatic. In the third phase, a new shape based ICM method is proposed to segment the VBs. 78
43. (a)The training VB images. In this experiment, 80 VB shapes which are obtained from 20 different patients and different regions (such as cervical, thoracic, and lumbar spine bone sections) are proposed. (b) The average shape of all training VB images. The darker color represents the higher object probability. 81
44. The shape model. The green color shows the background region which does not have any intersection with any training shape. The blue color shows the object region which is the intersection of all training shapes. (a) The gray color represents the variability region that can be described as the union of all projected training shapes subtracted by the intersection of those shapes. In this variability region, the object and background probabilistic shapes are defined. (b) The red color shows the outer contour of the variability region. (c) The object ($p(\mathbf{d} \mid \mathbf{f} = 1)$) and (d) background ($p(\mathbf{d} \mid \mathbf{f} = 0)$) shapes are modelled in the variability region in which the pixel values are defined in $(0 : 1)$. 82
45. The shape model is shown in 3D (when propagating 2D shape model into 3D). The outer volume represents the variability region, the inner volume represents the object region. 83
46. (a) The template used for the Matched filter, (b-d) a few images of automatic VB detection. The green line shows the detection of VB region. 85

47. In the first step, the MF is run on each slice of the 3D data. The output of this process is the detected points of each CT slices as shown with the blue dot. After the center points are detected, a mask is used to refine the data to specify the region of interest (ROI). In the mask, it is accepted that $a = 50$, $b = 60$, and $c = 20$. Any user can change these values. But the user should be careful to extract the spinal processes and ribs roughly. Then, another mask can be used to crop the ROI using the average center points (the red color) of all slices of 3D data. $d = 60$ is accepted to capture the VB region. 86
48. The extraction of the spinal cord on a data set (Example-1). (i) Sagittal view of each data. (ii) The detected VB region. (iii) The refined data to extract the spinal processes and ribs. (iv) The cropped data to reduce the size of the image. 87
49. The extraction of the spinal cord on a data set (Example-3). (i) Sagittal view of each data. (ii) The detected VB region. (iii) The refined data to extract the spinal processes and ribs. (iv) The cropped data to reduce the size of the image. 88
50. The extraction of the spinal cord on a data set (Example-5). (i) Sagittal view of each data. (ii) The detected VB region. (iii) The refined data to extract the spinal processes and ribs. (iv) The cropped data to reduce the size of the image. 89
51. The separation of each VB in a data set. Two choices are given to the user: The Manual and automatic options. Each option has its own advantages and disadvantages which are described the section. (a) An image which has 3 adjacent VBs. (b) The manual separation process with 6 points selected by a user. (c) The automatic separation method which was proposed by Aslan et al. in [86]. 90
52. The separation of the VB region. (a) 3D view of three adjacent VB, (b) automated placement of four seeds on cortical bone and disc, (c) separation of VB shown with red color. 91
53. The VB separation: The green volume shows the four four seeds. The red lines correspond to the number of voxels whose gray level are bigger than 200 HU. The black lines correspond to the threshold written in Eq. 60. 92
54. An example of the initial labeling. (a) Original CT images, (b) detection of the VB region and refinement, (c) the cropped VB region, (d) the initial labeling, $\mathbf{f}^*$ using only the intensity and spatial interaction models, and (e) the final segmentation using three models. 95
55. Embedding the shape model to the image domain and the final segmentation. (i) A CT data after the extraction of spinal cord. (ii) Shape model initialization (the blue color show the outer surface of the variability region $\mathbf{J}$). The contour $\mathbf{J}$ is placed equally in every slice using the obtained ROI. (iii) Embedding the shape model to the image domain. (iv) Final segmentation using three models: The intensity, spatial interaction, and shape information. Images and results are shown in the (a) sagittal, (b) coronal, and (c) axial views. 96

56. Embedding the shape model to the image domain and the final segmentation. (i) A CT data after the extraction of spinal cord. (ii) Shape model initialization (the blue color show the outer surface of the variability region **J**). The contour **J** is placed equally in every slice using the obtained ROI. (iii) Embedding the shape model to the image domain. (iv) Final segmentation using three models: The intensity, spatial interaction, and shape information. Images and results are shown in the (a) sagittal, (b) coronal, and (c) axial views. 97
57. In the segmentation quality measurements, there are 4 regions to be considered as: True positive (TP), false positive (FP), true negative (TN), and false negative (FN). The reference and test regions represent the ground truth and automatic segmented regions. 99
58. Good Initialization: Segmentation comparison under (a) no noise, noise variances (b) σ_n^2=0.1, (c) σ_n^2=0.25, and (d) σ_n^2=0.5. (i) Initialization. The results of (ii) $A1$, (iii) $A2$, (iv) $A3$ and (v) the proposed method. (The red and yellow colors show the contour of the ground truths and segmented regions, respectively.) 102
59. Worse Initialization: Segmentation comparison under (a) no noise, noise variances (b) σ_n^2=0.1, (c) σ_n^2=0.25, and (d) σ_n^2=0.5. (i) Initialization. The results of (ii) $A1$, (iii) $A2$, (iv) $A3$ and (v) the proposed method. (The red and yellow colors show the contour of the ground truths and segmented regions, respectively.) 103
60. Average segmentation accuracy of the VB segmentation on 12 CT images (ESP) with respect to the various noise levels. 104
61. The effect of the initialization on the segmentation accuracy of 12 CT images (ESP) using $A1$, $A3$, and the proposed. x_0 and y_0 represent the initial point in the X-direction and Y-direction respectively w.r.t the center of the object. 104
62. Segmentation results of an ESP CT slice with (a) no noise, noise variances (b) σ_n^2=0.1, (c) σ_n^2=0.25, and (d) σ_n^2=0.5. (i) The original gray level image with various noise levels. The results of (ii) only the intensity based segmentation, (iii) the initial segmentation $\mathbf{f}^*$ based on the intensity and spatial interaction models, (iv) proposed method integrating three models (intensity, interaction, and shape). 105
63. Average segmentation accuracy of the VB segmentation method on 12 ESP CT images . The size of each image is 512x512. (After each VB is detected, the size is reduced to 120x120). 105
64. The shape registration process and segmentation results of end-plate slices of VBs. (i) The shape model is registered to the initial segmented region. The blue color shows the contour of the registered variability region, **J**. (ii) Final segmentation results. The yellow color shows the contour of the segmented region. 108
65. Some of segmentation results are shown in the axial view. The yellow color shows the contour of the segmented region. 109

66. The shape embedding and final segmentation results are shown in 3D views. (a) A CT data is shown in the sagittal axis (without the refinement). (b) The initial location of the shape models. 2D shape models are propagated in z-axis to form 3D models. The blue color (outer volume) shows the variability region, whereas the yellow color (inner volume) represents the object region. (c) The shape model after registration. (d) The final segmentation results using the three models. 110
67. The shape embedding and final segmentation results are shown in 3D views. (a) A CT data is shown in the sagittal axis (without the refinement). (b) The initial location of the shape models. 2D shape models are propagated in z-axis to form 3D models. The blue color (outer volume) shows the variability region, whereas the yellow color (inner volume) represents the object region. (c) The shape model after registration. (d) The final segmentation results using the three models. 111
68. The shape embedding and final segmentation results are shown in 3D views. (a) A CT data is shown in the sagittal axis (without the refinement). (b) The initial location of the shape models. 2D shape models are propagated in z-axis to form 3D models. The blue color (outer volume) shows the variability region, whereas the yellow color (inner volume) represents the object region. (c) The shape model after registration. (d) The final segmentation results using the three models. 112
69. Some segmentation results examples on coronal (the first row) and sagittal (the second row) views of 3D segmentation. 113
70. Effects of each information is shown in 2D / 3D example. The Matched filter is employed to detect the VB region. (a) The segmentation result if only the intensity model is used. (b) The segmentation result if the intensity and spatial interaction models are used. (c) The segmentation result if the intensity, spatial interaction, and shape models are used. This is the proposed framework. 118
71. Segmentation framework. There are two parts: Offline stage is the training step to obtain the 3D shape prior and probabilistic model. Online stage is the testing step to segment a clinical CT data. 120
72. Obtaining the shape prior volume. {VB1,...,VBn} training CT slices of different data sets. (n represents the number of training data). The last column shows the shape prior slices with variability volume. . . . 121
73. Views of the 3D shape prior. The inner volume (the green color) shows the object volume $\mathcal{O}$, the outer volume (the yellow color) shows the variability volume $\mathcal{V}$. In (c) and (d) the variability volume is represented with several iso-surfaces. 122

74. (a-b) The 3D shape prior with object (the green color) and variability (iso-surfaces) volume. The green color represents the object volume, $\mathcal{O}$, the surface of the object volume represents the object/variability surface, $\mathbf{C}_{\mathcal{OV}}$, the waves represent the iso-surfaces, $\mathbf{C}_{d_p}$. (c) The probability of the object and background in the variability volume, $\mathcal{V}$, respect to each iso-surface, $\mathbf{C}_{d_p}$. 123
75. An example of the initial labeling. (a) Original CT image, (b) detection of the VB region, (c) the initial labeling, $\mathbf{f}^*$, and (d) the VDF of the initial segmentation which is used in the registration phase ($\Phi_{\mathbf{I}}$). Red color shows the zero level contour. 124
76. The registration step. (a) The testing image (or initially segmented image) as shown with the pink color. The testing and 3D shape prior before and after the registration are shown in (b) and (c), respectively. Each row shows different views. 126
77. An overall segmentation steps with 2D/3D example. The Matched filter is employed to detect the VB region. Then, the initial segmentation using the LCG model is obtained. Finally the graph cuts method which integrates the LCG, MGRF, and shape probabilistic model is used to obtain the final segmentation. 129
78. An example of the graph $\mathcal{G} = \{\mathcal{U}, \mathcal{E}\}$. All vertices represented as $\mathcal{U} = \{\textit{source}, \textit{sink}, a, b, c, d, e, f, g, h, i\}$. *p-vertices* (pixels) are {a,...,i}. *l-vertices* (terminals or labels) are source (s) and sink (t). $\mathcal{E}$ is represented as lines connecting vertices. Lines connecting *p-vertices* to *l-vertices* represents *t-links*. Lines connecting each *p-vertex* with its neighboring *p-vertices* represent *n-links*. *n-links* are constructed for 4-neighboring system. (In the graph, the pixel e represents p in the equations.) 130
79. 3D results of a clinical data set. (M1) The result of the proposed method, (M2) results of graph cuts without shape prior, (M3) results of the Level sets, and (M4) results of the b-spline based interpolation. The red color shows the segmentation errors. 133
80. Order of the neighboring system 145
81. Second order of the neighboring system. 145
82. Cliques types of the second order neighborhood. 145

List of Algorithms

ALGORITHM PAGE

1 Proposed framework 77
2 Training stage (Obtaining Probabilistic Shape Model) 80
3 Optimization of Three Models 98
4 Proposed framework 119
5 Probabilistic 3D Shape Model Reconstruction (More Detailed) 120
6 Proposed VB segmentation framework 131

CHAPTER I

INTRODUCTION

Segmentation can be defined as partitioning the image into the meaningful areas using the existing (low level) information in the image and prior (high level) information which can be obtained using a number of features of an object. Figure 1 shows some examples of the segmentation of images into the meaningful areas. Figure 2 shows an example of horses in a background of a snowy ground. The human vision system aims to extract and use as much as possible information in the image [1,2]. The possible information includes the intensity, possible motion of the object (in sequential images), spatial relations (interaction) as the existing information, and the shape of the object which is learnt from the experience as the prior information. The horses cannot be separated from the background using only the existing information in the image. After a while, the human visual system combines the existing information (such as intensity and spatial interaction) and prior information (such as shape) which is learnt from experience. However, the machine visual system cannot predict the prior information unless it is supplemented. Hence, any prior cue can be specified beforehand to enhance the segmentation or to obtain the desired segmentation. If the prior information of the object is not given beforehand to the machine vision task, the segmentation method may not give desired results due to noise, occlusion, and missing information in the image.

This dissertation deals with the coupling the existing (intensity, spatial interaction) and prior (shape) information to obtain the desired segmentation. The intensity information is modeled using the histogram of gray levels of the image. The model estimates the marginal density for each class. The spatial interaction in-

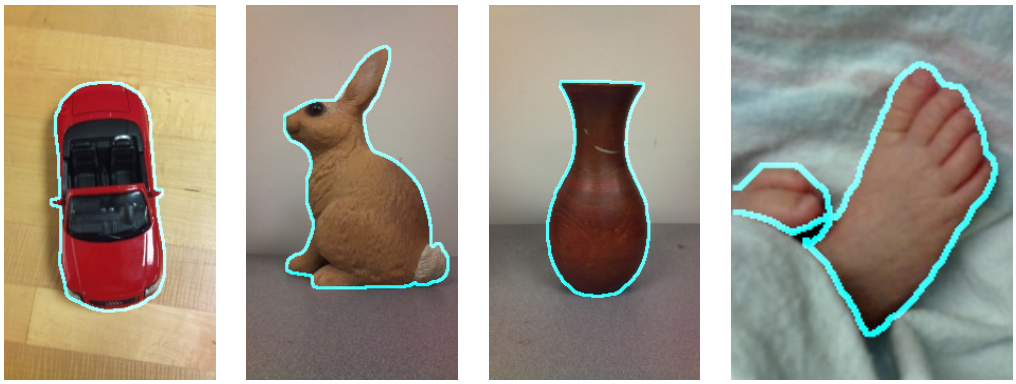

FIGURE 1 – Examples of the image segmentation into the meaningful areas. The blue color shows the contour of the desired segmentation region.

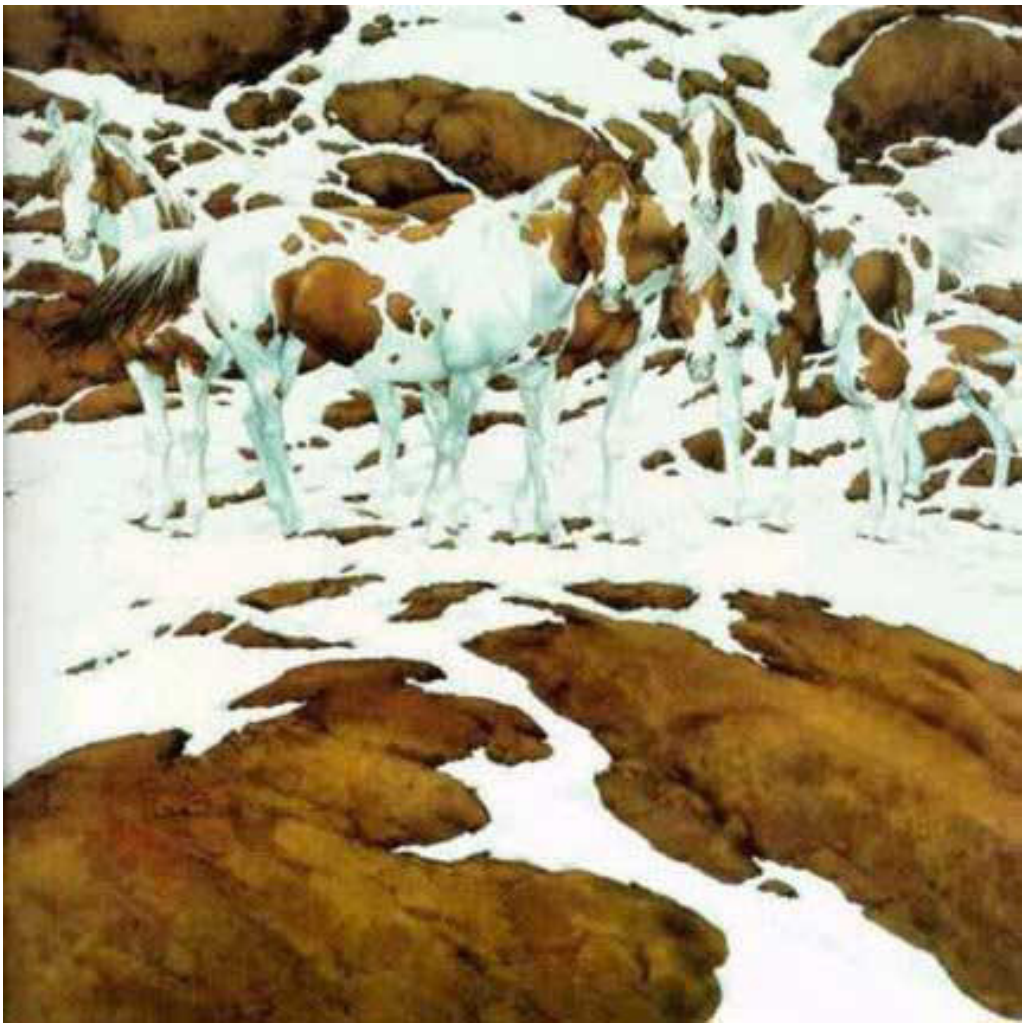

FIGURE 2 – An image of horses in a background of partially snowy ground. (This image is ascribed to Bev Doolittle.)

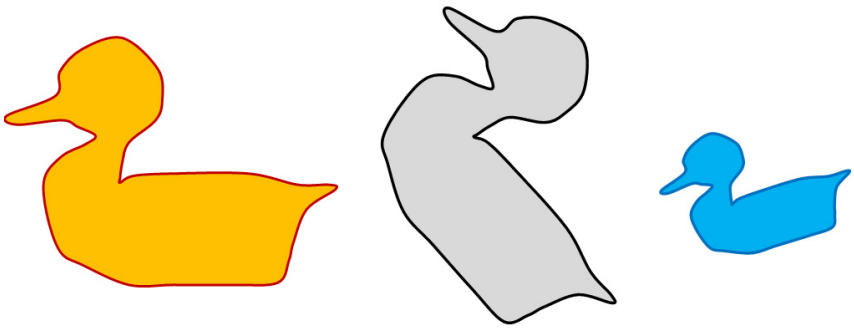

FIGURE 3 – An example for the shape definition. The shape in the figure is a duck even the shape is translated, rotated, and scaled.

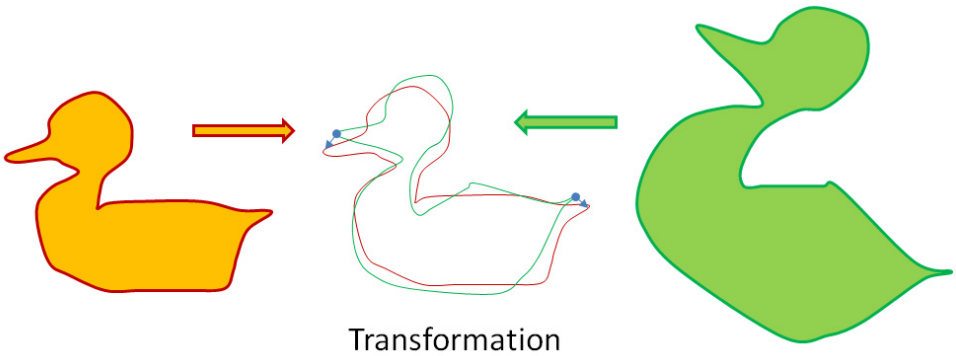

FIGURE 4 – An example for the shape registration. After the source and target shapes are registered, the shape variability is modeled.

formation is modeled using the relationship between the neighboring pixels. The spatial interaction model assumes that the pixel intensity depends on the intensities of the neighboring pixels. For the shape definition, mathematician and statistician D. G. Kendall writes: ”All the geometrical information that remains when location, scale, and rotational effects are filtered out from an object.” Hence, the shape information is modeled after the sample shapes are transformed into the reference space. Finally, the shape variability is modeled using the occurrences of the transformed shapes. Figures 3 shows the same shapes with different scale, rotation, and translation factors. Figure 4 shows an example of the registration process from the source to the target image / shape. The following section presents problem statement.

A. Problem Statement

This dissertation deals with object labeling using segmentation and registration methods. The problem can be described as follows: Given an image, it is required to obtain / extract the region-of-interest (ROI) using the existing information in the image (such as the intensity, edge, curvature, and etc.) and prior information about the object / shape. A labeling problem can be described in terms of a set of pixel and a set of labels. The description of each variables can be written as follows: Let

- $\mathbf{I}$ be an $n-D$ image (where $\mathbf{I} : R^n \rightarrow R$ and usually $n = 2$ or $n = 3$).
- $\Omega \subset R^n$ be an image domain.
- $\mathbf{G} = \{0, \ldots, Q-1\}$ be a set of pixel intensity value where Q is the number of gray levels and $Q \in N^+$. For instance, for gray level image by 2^8, the set of pixel intensity value can be written as $\mathbf{G} = \{0, \ldots, 255\}$ where $Q = 256$.
- $\mathcal{L} = \{0, \ldots, K-1\}$ be a set of labels where K is the number of labels and $K \in N^+$. For instance, assume that the desired classes / regions are 4. Then, the set of labels can be written as $\mathcal{L} = \{0, 1, 2, 3\}$ where $K = 4$.

As given the descriptions above, the image can defined as

$$\mathbf{I} : \Omega \rightarrow \mathbf{G} \quad , \quad \Omega \subset R^n. \tag{1}$$

Labeling is assigning a label from the label set $\mathcal{L}$ to each pixel in Ω, and it can be shown as

$$\mathbf{f} : \Omega \rightarrow \mathcal{L}. \tag{2}$$

In this dissertation, three pieces of information (intensity, spatial interaction, and shape) are modelled to obtain the optimum segmentation. The intensity information is modelled using the Gaussian distribution. The data is assumed to have two classes: background and object regions which are represented as "b" or "0" and

"o" or "1", respectively. The parameters of distributions ($\Theta = \mu_o, \sigma_o, \pi_o, \mu_b, \sigma_b, \pi_b$ for the mean, standard deviation, and prior probability, respectively) are estimated. Spatial interaction that describes the relation between pixels is modeled using a Markov-Gibbs random field (MGRF). This dissertation deals with the homogeneous isotropic Potts model proposed by Geman et al. [3] which is similar to the Derin-Elliot model in [4]. The shape variability is described using a new probabilistic function. The shape models are obtained using histogram of occurrences of training shape pixels or voxels and formulated by new formulations. The objective is to capture the shape variation of the object of interest. Using the intensity, spatial interaction, and shape modelling, each pixel in the image will have intensity, spatial interaction, and shape based probabilities to be an object or a background class.

The segmentation process can be achieved by minimizing an energy formulation which can be written as follows:

$$E = E(\mathbf{I}, \mathbf{I}_{shape}, \mathbf{T}, \Theta, \gamma, \mathbf{w}) \tag{3}$$

where

- $\mathbf{I}_{shape}$ represents the shape prior, which is obtained using a number of training shapes and a chosen function,
- $\mathbf{T}$ represents the required transformation matrix to embed the shape prior to the image domain,
- Θ is the intensity model parameters,
- γ is the spatial interaction parameters,
- $\mathbf{w}$ is the shape model parameters.

In the energy optimization process, the parameters which should be estimated can be written in a formulation as:

$$\mathbf{f}^*, \Theta^*, \gamma^*, \mathbf{w}^*, \mathbf{T}^* = \arg \min_{\mathbf{f}, \Theta, \gamma, \mathbf{w}, \mathbf{T}} E. \tag{4}$$

In this dissertation, the energy functionals are optimized using three different approaches which have different advantages: i) the level sets which uses the gradient descent and simplex optimizations, ii) the iterated conditional modes (ICM), and iii) Graph cuts . The detailed descriptions will be given in the following chapters.

Overall, in the shape based segmentation, the following problems should be answered:

- Determining the best / appropriate model for each information.
- Defining the shape transformation type (such as rigid, affine, or local types).
- Defining a dissimilarity measure between two shapes (such as intensity difference and etc.) and its formulation.
- Estimating the shape transformation matrix.
- Optimization type (such as gradient descent, simplex methods, and etc).

This dissertation will address these problems.

1. Energy Formulation Using Bayes' Rule

Many image segmentation approaches are modeled in a probabilistic framework [1]. Given an image, the posterior probability is maximized using the Bayes' rule as follows:

$$p(\mathbf{f} \mid \mathbf{I}) = \frac{p(\mathbf{I} \mid \mathbf{f})p(\mathbf{f})}{p(\mathbf{I})}, \tag{5}$$

where $p(\mathbf{I} \mid \mathbf{f})$ is a conditional distribution of the input image given the desired labeling, $p(\mathbf{f})$ and $p(\mathbf{I})$ are unconditional probability distributions of the desired labeling and the given image, respectively. Maximizing the conditional probability of desired labeling, $\mathbf{f}$, given the image, $\mathbf{I}$, is equivalent to minimizing its negative logarithm as shown follows:

$$-\log p(\mathbf{f} \mid \mathbf{I}) = -\log p(\mathbf{I} \mid \mathbf{f}) - \log p(\mathbf{f}) + \textit{constant}. \tag{6}$$

Using the same idea, the conditional probability of desired labeling, $\mathbf{f}$, given the image, $\mathbf{I}$, and the prior shape information of the object, $\mathbf{I}_{shape}$ can be given as follows:

$$-\log p(\mathbf{f} \mid \mathbf{I}, \mathbf{I}_{shape}) = -\log p(\mathbf{I} \mid \mathbf{f}) - \log p(\mathbf{f}) - \log p(\mathbf{I}_{shape} \mid \mathbf{f}, \mathbf{I}) + \textit{constant}. \quad (7)$$

Finally, the energy can be written in terms of the posterior probability as defined as follows:

$$E = -\log p(\mathbf{f} \mid \mathbf{I}, \mathbf{I}_{shape}) \simeq -\log p(\mathbf{I} \mid \mathbf{f}) - \log p(\mathbf{f}) - \log p(\mathbf{I}_{shape} \mid \mathbf{f}, \mathbf{I}). \quad (8)$$

Eq. 8 summarizes the main energy formulation which is being optimized in this dissertation. Note that each chapter has its own derivation of Eq. 8.

B. Shape Representation

Human anatomical structures such as spine bones, kidneys, livers, hearts, and eyes may have similar shapes [5]. These shapes usually do not differ greatly from one individual to another. There are many works which represent and model the shape variability. The objective of a shape representation is to describe the desired features of the shape of interest and serve the shape descriptor to be a good classifier to differentiate among all the shapes involved [6]. Also, the shape representation significantly affect the shape registration algorithm. In general, the shape representations methods can be folded into three categories:

(a) Landmark based,

(b) Contour (edge) based, and

(c) Region based methods.

This section briefly reviews these three shape representation and modeling categories. One of the most important studies for the landmark based shape representation and modeling is the active shape models (ASM) and active appearance models (AAM) proposed by Cootes et al. [7–9]. The active contour models method is a contour (edge) based method proposed by Kass et al [10]. This method is also

categorized as the explicit shape representation which requires parameterizations of the contour. Also, Fourier descriptors, shape signatures, wavelet descriptors are some of the contour based shape representations. Landmark and contour based representations, which can be called as the explicit shape representation, suffer when applied to shape modeling since they do not allow the shape to undergo topological changes. Also, these representations requires point-wise correspondence between training shapes.

This dissertation represents shapes using the regions based methods. Medial axis, convex hull, and level sets representations are some of the region based shape representations. The shape representation using the level sets method [11] is known as the implicit representation which does not need contour parameterizations and does handle the topological changes of shapes. Leventon et al. [12], Rousson et al. [13] and Tsai et al. [14], Abdelmumin [5] proposed shape models which are obtained using a signed distance function (SDF) of the training data. Eigenmodes of implicit shape representations are used to model the shape variability. Their method does not require point correspondences. Their shape model is obtained using a coefficient of each training shape. Cremers [15] et al. proposed a simultaneous kernel shape based segmentation algorithm with a dissimilarity measure and statistical shape priors. This method is validated using various image sets in which objects are tracked successfully. For more information about the shape representation and modeling, refer to [16–18]. In this dissertation, the object shape variability is analyzed using probabilistic models which guide the energy optimization.

C. Shape Based Segmentation

Shape based segmentation has been handled in different manners in many applications like segmentation, shape recognition, and tracking. Shape based segmentation can be defined as the integrating the prior shape model into the seg-

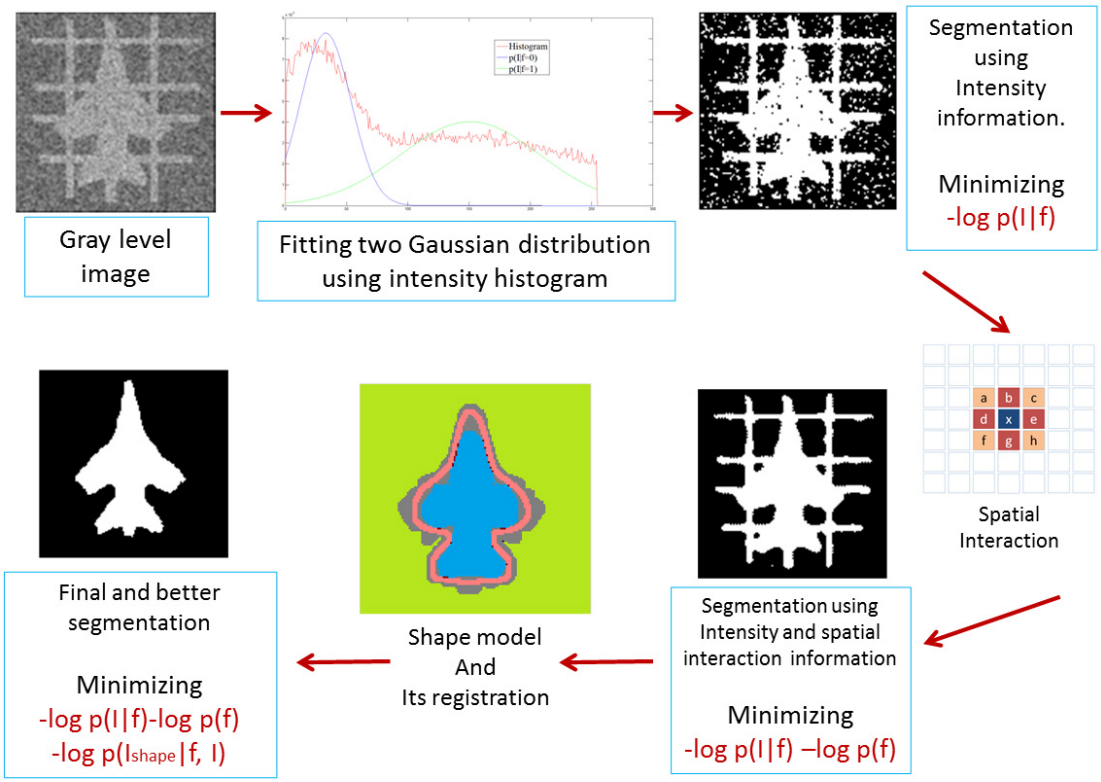

FIGURE 5 – An example segmentation with coupling the existing and prior information. The gray level image has problems such as noise and occlusion. The intensity modeling is not enough only to solve the noise and occlusion problems. The spatial interaction coupling with the intensity information is able to solve the noise but not the occlusion problem. Shape modeling coupling with the existing information is able to solve both the noise and occlusion problems.

mentation via shape registration process. In this matter, the prior shape model is obtained in advance using a number of training shapes of the object of interest.

Figures 5 and 6 show example segmentations using the existing and prior information when images have noise, missing information, and occlusion problems. Traditional approaches such as thresholding [19–22] using only the gray level information will not work to solve the noise problem. Edge-and-contour based variational methods [10, 11, 23–25] and spatially discrete optimization methods [26–29] using only the existing information (intensity and / or spatial interaction) may work well to solve the noise problem. However, these methods will not be able to obtain desired segmentation when there is occlusion problem in the image. To solve the possible problems in the image, the shape prior information

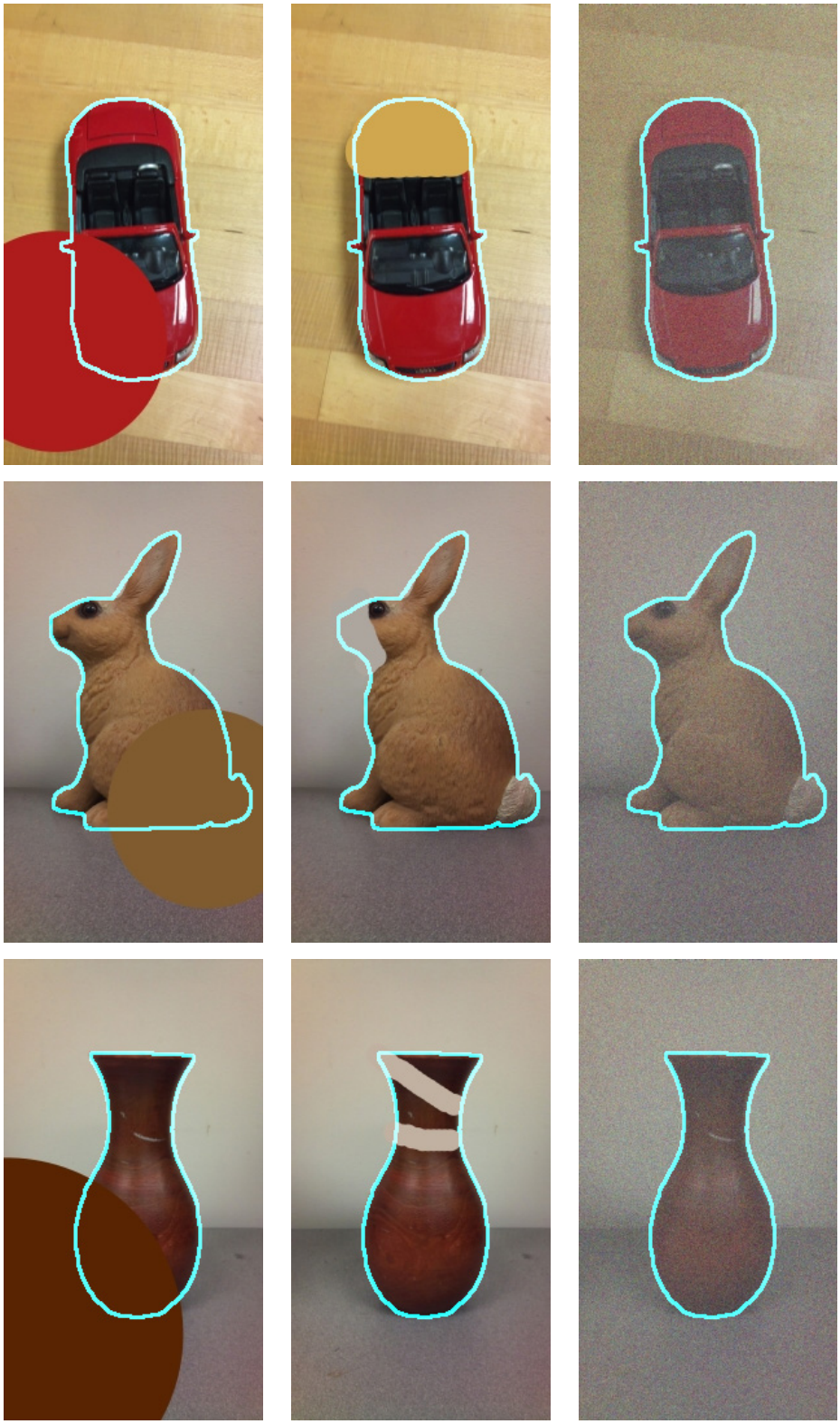

FIGURE 6 – Examples of the image segmentation into the meaningful areas when the image has occlusion, missing information, and noise problems. The blue color shows the contour of the desired segmentation region.

is integrated in the segmentation process. Refer to [1, 2, 5, 7, 9, 12–15, 30–44] for publication of the shape based segmentation methods.

D. Shape/Image Registration

Registration is the important method for shape-based segmentation, shape recognition, tracking, feature extraction, image measurements, and image display. Shape registration can be defined as the process of aligning two images of a scene [5, 45]. Image registration requires transformations, which are mappings of points from the source (reference) image to the target (sensed) image [46]. The registration problem is formulated such that a transformation that moves a point from a given source image to another target image according to some dissimilarity measure, needs to be estimated [47]. The dissimilarity measure can be defined according to either the curve or to the entire region enclosed by the curve. Figures 7 shows an example of the registration process from the source to the target image / shape. The source and target images and transformation can be defined as follows:

- Source (I_s): Image which is kept unchanged and is used as a reference. This image can be written as a function $I_s : R^2 \rightarrow R$ for $\forall \mathbf{x} \in \Omega_s$.
- Target (I_t): Image which is geometrically transformed to the source image. This image can be written as a function $I_t : R^2 \rightarrow R$ for $\forall \mathbf{y} \in \Omega_t$.
- Transformation ($\mathbf{T}$): The function is used to warp the target image to take the geometry of the reference image [45]. The transformation can be written as a function $\mathbf{T} : R^2 \rightarrow R^2$ which is applied to a point $\mathbf{x}$ in I_s to produce a transformed point which is calculated as $\mathbf{X} = \mathbf{T}(\mathbf{x})$. The registration error is calculated as $\mathbf{T}(\mathbf{x}) - \mathbf{y}$ for each transformed pixel.

Steps in the registration can be categorized in 5 different ways such as:
i) Preprocessing: Image smoothing, deblurring, edge sharpening, edge detection, and etc.

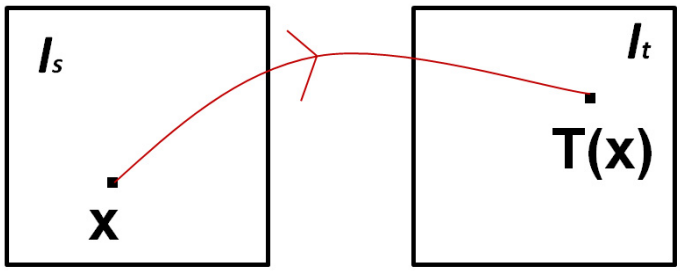

FIGURE 7 – Registration example of a point from the source to the target image.

ii) Feature selection: Points, lines, regions and etc. from an the source and target image.

iii) Feature correspondence: The correspondence between two images.

iv) The transformation functions: Affine, rigid, projective, curved and etc.

v) Resampling: Transformed image should be resampled in the new image domain.

In general, there are three categories of the registration methods: rigid, affine, and elastic transformation. In literature the rigid and affine transformations are classified as global transformations and elastic transformations are as local transformation [48]. A transformation is global if it is applied to the entire image. A transformation is local if it is a composition of two or more transformations determined on different domains (sub-images) of the image.

- A rigid body transformation is the most fundamental transformation and is useful especially when correcting misalignment in the scanner. This transformation allows only translation and rotations, and preserves all lengths and angles in an image.

- An affine transformation allows translation, rotation, and scaling. Some authors defined the affine transformation as the rigid transformation plus scaling. Affine transformations involving shearing (projection) are called projective transformation. An affine transformation will map lines and planes into lines and planes but does not preserve length and angles.

- An elastic transformation allows local translation, rotation, and scaling, and it has more number of parameters than affine transformations. It can map straight lines into curves. An elastic registration is also called as a non-linear or curved transformation. This transformation allows different regions to be transformed independently.

A global transformation is used to register I_s to I_t with scale, rotation, and translation parameters. For the 2D case, assume that the transformation has scaling, rotation, and translation components represented as follows:

$$\mathbf{S} = \begin{bmatrix} s_x & 0 \\ 0 & s_y \end{bmatrix}, \ \mathbf{R} = \begin{bmatrix} cos(\theta) & -sin(\theta) \\ sin(\theta) & cos(\theta) \end{bmatrix}, \ \mathbf{Tr} = [t_x, t_y]^t. \tag{9}$$

The transformation will be in the form:

$$\mathbf{T}(\mathbf{x}) = \mathbf{X} = \mathbf{SRx} + \mathbf{Tr}. \tag{10}$$

This dissertation uses the global registration (more specifically affine transformation) using the signed distance function which is widely used in the registration methods and shape models and point correspondence.

E. Related Works

The motivation and contribution of this dissertation can be folded in three sections: 1) Variational (Spatially continuous) method. 2) Statistical (spatially discrete) method. 3) Algorithms on vertebral body segmentation. The following sections overview related works. The weaknesses of existing are addressed in the following three subsections. (It should be notes that the material in each subsection will be revisited in the related chapter.)

1. Variational (Spatially Continuous Methods) Approach

Variational approaches segment shapes through an energy minimization framework that controls the evolution of an implicit / explicit contour / surface. The active contour models proposed by Kass et al. [10] and level sets proposed by Osher and Sethian [11] are the most important variational methods in the literature. The active contour models minimizing the energy formulation using the explicit shape representation which requires parameterizations of the contour. As discussed already explicit shape representations suffer when applied to shape modeling since they do not allow the shape to undergo topological changes.

The level sets method is one of the efficient and accurate method in the segmentation despite it is fact that it has still some disadvantages which will be discussed in this dissertation. The level sets method has also been used in the shape-based segmentation problem. The implicit shape representation which does not need contour parameterizations and does handle the topological changes of shapes is used. In this area, embedding the shape model into the image domain is the key issue and depends on the registration of the given shape to the image. Paragios et al. [47] firstly proposed a global and local registration method using the implicit representation (the signed distance function) of target and source shapes. Their method does not require point correspondences which is very important contribution in the automatic shape registration field.

The related works can be listed as follows:

- The level sets formulations, which are based on only the intensity and / or edge information (such as what Chen-Vase [23], Li et al. [25], Gao et al. [49] proposed) fail when the image has noise or the object has various missing parts and occlusions.

- In the shape registration methods, the dissimilarity measures proposed by Paragios et al. [47], Rousson et al. [13], Tsai et al. [14], and Huang et al. [31],

and etc. have limitations to capture the object-of-interest if the source and target shapes have inhomogeneous scale differences. Limited shape model embedding transformation (homogeneous scales) is used.

- Active appearance models method, which was originally proposed by Cootes et al. [9], has been used in many applications. However, the shape model should be initialized very close to the object-of-interest for the originally proposed method. It should be noted that there have been improvements on AAM to eliminate the dependency on the shape initialization. In this dissertation, the originally proposed AAM method is referred.

2. Statistical (Spatially Discrete) Approach

Although the spatially continuous methods work very well, they usually take higher execution time to obtain the optimum segmentation than some of spatially discrete optimization methods such as iterated conditional modes (ICM) and graph cuts. The related works can be listed as follows:

- The original ICM method is a local optimization technique as proved in [50]. Also, ICM optimization without shape model fails if the object interest has missing information and occlusions.

- Graph cuts, proposed by Boykov et al. [29], is very powerful and fast energy minimization approach. In this method, each edge of the graph, which connects neighboring pixels in the image and connects the pixels with terminals (or labels), should be assigned a cost or a penalty term. Often, the penalty term is estimated using simple functions that are inversely proportional to the gray scale difference between the two pixels and their distance, and one may need to adapt the optimum cost coefficient to obtain a desired segmentation.

3. Algorithms on Vertebral Body Segmentation

The previously reported methods can be categorized as fully automatic, and semi-automatic (with manual interactions). In this work, a segmentation method with a semi/fully-automatic option is proposed. The related works and contributions can be listed as follows:

- In one of the semi-automatic works, Mastmeyer et al. [51] proposed a hierarchical segmentation approach only for the lumbar spine bone. Such works are restricted to the specific regions of spine bone column as such lumbar, thoracic, and others.

- Klinder et al. [36] proposed a fully automatic solution for detecting, identifying, and segmenting vertebrae in CT images. The authors reported that the execution time for 12 vertebrae identification was 2192 seconds (36.5 min) on average. Also, Mastmeyer et al. [51] reported that complete analysis of 3 vertebrae took approximately 10 minutes in 2006 on a high standard PC system.

- The methods proposed by Yao et al. [52], and Klinder et al. do not extract the spinous/spinal processes,pedicles, ribs, ant other anatomical bones from the VB. In other works, such as [51], spinal processes are eliminated with an additional high execution time.

- In CT spinal images, different partial regions are scanned. For instance, some CT data have only 4-5 thorocic VBs, some of them have 2-3 lumbar VBs, and etc. A framework which is dependent of the identification of VBs in a dataset can cause high execution time.

F. Contributions of this Dissertation

This section overviews the contributions of the dissertation specifically. It should be noted that the material in each subsection will be revisited in the related chapter. The contributions of this dissertation can be listed as follows:

- This dissertation solves problems caused by noise, occlusion, and missing information of the object by integrating the prior shape information.
- In this dissertation, the conventional shape based segmentation results are enhanced by proposing a new probabilistic shape models and a new energy functional to be minimized. The shape variations are modelled using a probabilistic functions. The proposed method is tested on the synthetic and clinical images / shapes and it is shown to be robust under various noise levels, occlusions, and missing object information.
- The proposed shape based segmentation methods are less variant to the initialization.
- To optimize the energy functional, the original ICM method, which was originally proposed by Besag [53], is extended by integrating the shape prior. With integrating the shape model to the original ICM method, possible local minimums of the energy functional are eliminated as much as possible, and enhance the results. Also, similar framework using graph cuts energy minimization is tested in this study.
- One of the most important contributions of this study is to offer a segmentation framework which can be suitable to the clinical works with acceptable results. If the proposed method in this dissertation is compared most published bone segmentation methods (such as in [36,51,54]), the large execution time is reduced effectively.
- Many works are restricted to the specific regions of spine bone column as

such lumbar, thoracic, and others. In this dissertation, there is no any region restriction, and the proposed framework is processed on different regions.

- The proposed framework and the new probabilistic shape model extract the spinal processes and ribs which should not be included in the bone mineral density measurements.
- This work is not dependent on any identification step thanks to the new universal shape model and its embedding step.

G. Dissertation Organization

This dissertation has 4 more chapters as follows:

Chapter II presents mathematical background of the level sets method which has been used for segmentation and registration algorithms in the literature. In this chapter, a new probabilistic shape based segmentation method is proposed and tested on various synthetic and clinical images with occlusions, missing information, and noise. The proposed method is a generic method which can be suitable to segment any object in the image.

Chapter III introduces a new shape based iterated ICM method. The proposed method is a specific segmentation method which is fully focused on the vertebral body segmentation. In this chapter, some of drawbacks existing in the vertebral body segmentation are solved with a new statistical framework.

Chapter IV presents an extension study of previously published method. In [55, 80], the shape model is assumed to be registered in advance. In this dissertation, the probabilistic shape model is registered automatically to the image domain.

Chapter V summarizes the main component of the proposed works and presents possible future improvements.

CHAPTER II

A PROBABILISTIC SHAPE-BASED SEGMENTATION METHOD USING LEVEL SETS

In this chapter, a new dynamic and probabilistic shape based segmentation method using level sets method is proposed. The shape prior is coupled with the intensity information in this chapter. In the first phase, the intensity based segmentation is obtained using a basic statistical level set method. In the second phase, in which this work's contribution lies, the shape model is constructed using the implicit representation of the training shapes. The resulting probability density functions are used to embed the shape model into the image domain with a new energy functional. The proposed method's invariance to parameter initialization is evaluated through validation. Various synthetic and clinical shape segmentation examples are illustrated. Experiments show that the proposed algorithm overcomes segmentation challenges, and is robust under various noise levels, severe occlusions, and missing information.

A. General Level Sets Formulation and Derivation

The level sets formulation was first introduced by Osher and Sethian [11]. Topology changes like merging and splitting, are handled naturally without the need of parametrization. This section mainly focuses on the general level sets formulation

Given a curve C, it can be embedded into a higher dimension function ϕ as $C = \{\mathbf{x} : \phi(\mathbf{x}) = 0\}$. Then the curve is defined as the zero level of the implicit function. If the time t is added to the function, curve evolution function is changed to $\phi = \phi(\mathbf{x}, t)$. Topology changes, such as merging or splitting, are almost impossible

to be handled by the conventional explicit deformable models. However, topology changes can be tracked naturally by implicit level sets. The surface function ϕ evolves with the time and the evolution front is always represented as the zero level. The following equation can be written as a general description:

$$\phi(\mathbf{x}, t) = 0. \tag{11}$$

Taking derivative on both sides of the above equation, it leads to:

$$\frac{\partial \phi(\mathbf{x}, t)}{\partial t} = 0. \tag{12}$$

In terms of chain rule, the above equation can be written as follows:

$$\frac{\partial \phi}{\partial t} + \frac{\partial \phi}{\partial \mathbf{x}} \bullet \frac{\partial \mathbf{x}}{\partial t} = 0. \tag{13}$$

Eq. 13 can be written as follows:

$$\phi_t + \nabla \phi \bullet \mathbf{B} = 0. \tag{14}$$

where $\nabla \phi$ represents the gradient of ϕ and $\mathbf{B}$ represents the velocity vector which is defined as $\mathbf{B} = \frac{\partial \mathbf{x}}{\partial t}$. The velocity vector contains the tangent and normal vectors as $\mathbf{B} = B_T \overrightarrow{\mathbf{T}} + B_N \overrightarrow{\mathbf{N}}$ resulting the following formulation:

$$\phi_t + \nabla \phi (B_T \overrightarrow{\mathbf{T}} + B_N \overrightarrow{\mathbf{N}}) = 0. \tag{15}$$

By the definition, the normal vector of the evolving function can be written as $\overrightarrow{\mathbf{N}} = \frac{\nabla \phi}{|\nabla \phi|}$. Then substituting for $\nabla \phi = |\nabla \phi| \overrightarrow{\mathbf{N}}$ gives the following:

$$\phi_t + |\nabla \phi| \overrightarrow{\mathbf{N}} (B_T \overrightarrow{\mathbf{T}} + B_N \overrightarrow{\mathbf{N}}) = 0. \tag{16}$$

Since the multiplication of the normal and tangent lines produces 0, the formulation can be written as follows:

$$\phi_t + B_N |\nabla \phi| = 0. \tag{17}$$

In the iterative process of the level sets, the curve evolution can be obtained using the following formulations as follows:

$$\frac{\phi(t + \triangle t) - \phi(t)}{\triangle t} + B_N |\nabla \phi| = 0, \tag{18}$$

since $\phi_t = \frac{\phi(t+\triangle t)-\phi(t)}{\triangle t}$. Then, multiply each components by $\triangle t$,

$$\phi(t+\triangle t) - \phi(t) + \triangle t B_N |\nabla \phi| = 0, \tag{19}$$

Finally the next evolution of ϕ is obtained as follows:

$$\phi(t+\triangle t) = \phi(t) - \triangle t B_N |\nabla \phi| = 0, \tag{20}$$

In the literature, the final level sets formulation is defined as follows:

$$\phi(t+\triangle t) = \phi(t) - F|\nabla \phi| \triangle t = 0. \tag{21}$$

In the literature, there has been various methods to model the speed function, F. In this dissertation, a new method which is integrating the intensity and prior shape information is proposed. The next section describes the proposed level sets formulation.

B. Related Works

Shape based segmentation is an important and complex problem in computer vision, computer graphics and medical imaging. It has been handled using different methods in many applications like segmentation, shape recognition, and tracking. Segmentation using only image intensity may fail in the presence of strong noise and partial occlusions. Therefore, a prior shape is necessary to enhance the segmentation results.

Level sets method has been used previously in the shape based segmentation problem. Paragios et al. [47] firstly proposed a global and local registration method using signed distance function (SDF) of target and source images / shapes. They seek a transformation that creates pixel-wise intensity correspondences between the source and the target shape representations. The registration parameters are obtained using the gradient descent optimization. Their method is tested with partial occlusions, local deformations, and random motion between the source and

target. To guarantee stability, the numerical method requires a small time step which results in high execution time as the authors agreed.

In [31] the distance function is used to implicitly represent open/closed shapes (structures). The images of distance functions are registered using the mutual information approach. The signed distance function is used for closed shapes, whereas open structures are represented by using only the distance transform without any sign. In addition to global registration, they used a b-spline based incremental Free Form Deformation (IFFD) to minimize a dissimilarity measure. The local registration is used to obtain smooth, continuous, and one-to-one correspondences.

Tsai et al. [14] proposed a new shape model which is obtained using a signed distance function of the training data. Eigenmodes of implicit shape representations are used to model the shape variability. Their method does not require point correspondences. They proposed a new shape prior which was obtained using a coefficient of each training shape. The shape model described in their paper is used to register the shape model globally to the object of interest.

Taron et al. [32] proposed an invariant representation of shapes, and computing uncertainties on the registration process. Also, in this study the shape is represented implicitly. They proposed a novel dimensionality reduction technique to lower the cost of the density estimate computation of kernel based shape model.

Cremers et al. [15] proposed a simultaneous kernel shape based segmentation algorithm with a dissimilarity measure and statistical shape priors. This method is validated using various image sets which objects are tracked successfully. However, parameter optimization of the shape priors may have high execution time if the training set is large.

Mahmoodi [56] proposed a shape-based active contours for fast video segmentation. Their level sets implement is based on Mumford-Shah [57] and Chan-Vese [23] methods. They compared their method with only intensity based segmentation method.

Gao et al. [58] proposed a method to segment prostate magnetic resonance (MR) imagery. To model the large variations of prostate shapes, they used point clouds to represents training shapes.

Zhu et al. [59] proposed a shape and temporal based segmentation algorithm for cardiac MR imagery. They developed a subject-specific dynamical model that handles temporal dynamics and inter-subject variability and deformation. They modelled the temporal dynamics of a cardiac sequence. Their method is eligible to model the motion in patient imaging.

Heckel et al. [60] discussed variational interpolation for segmentation of medical images with respect to applications in tumor and liver segmentation from CT scans. However, interpolation methods are still time consuming and they have high computational cost as the authors documented. Mahdavi et al. [38] proposed a semi-automatic segmentation for prostate interventions. In this method manual initialization of the shape priors makes use of the physicians experience. Schmid et al. [39] proposed a new statistical shape models for MRI bone segmentation. They devised an initialization of deformable models for the challenging hip joint MRI images. Tsechpenakis and Chatzis [40] proposed a probabilistic shape and appearance-based segmentation method using deformable models. Gao et al. [49] proposed a relay level sets method for segmentation.

Yan et al. [41] proposed a local shape models for segmentation of ultrasound prostate images. They proposed a new energy functional which has three terms: i) the first energy attracts the contour toward the prostate boundary, ii) the second energy preserves the geometric shape of the contour during deformation by applying the constraints of continuity and curvature, iii) the third term applies the shape constraint derived from a priori shape statistics to the segmented contour. They applied their algorithm on ultrasound prostate images.

Saha et al. [42] proposed an osteophyte segmentation method using a partial shape model. They proposed a method primarily based on the active shape model (ASM). Their objective is to solve a common challenge when a diseased bone shape

is significantly altered at regions with osteophyte. Osteophytes are segmented by subtracting partial-ASM-derived shape from the overall diseased shape.

Pu et al. [43] proposed a shape analysis strategy termed ”break-and-repair” to overcome segmentation challenges such as various organ diseases, image noise or uncertainties. The basic idea is to remove problematic regions and then estimate a smooth surface by representing the remaining regions. They used the principle curvature analysis to identify and remove the problematic regions. The performance of their method was tested on CT lung images.

Feulner et al. [44] proposed a probabilistic model for automatic segmentation of the esophagus in 3D CT images. The shape model is incorporated using a Markov chain model. The model is nonrigidly deformed to fit the boundary of an object.

Shen et al. [61] proposed an active volume models (AVMs) for object boundary extraction. The dynamic model includes a deformed curve or surface representing a shape, a volumetric appearance statistics, and an embedded object / background classifier. Compared with active contours and active shape / appearance models, the AVM is a generative object modelling that does not require offline training but generates useful appearance priors about the object.

Dawoud [62] proposed a shape based lung segmentation in chest radiographs. Their approach is based on integrating the shape model into intensity based thresholding in an iterative framework.

Lee at al. [63] proposed an automatic segmentation of the lumbar pedicle in CT images to help spinal fusion surgery. Their objective is to help spinal fusion process which requires pedicle screw placement. They emphasized the segmentation challenges of spine bones in CT images due to weak edges and boundary discontinuities.

C. Contribution of This Study

In this work, a new dynamic and probabilistic shape model which is reconstructed using implicit representation of shapes. New shape based probability density functions are proposed to enhance the conventional global registration energy functionals. Second, a new probabilistic dissimilarity measure on the space of level set function is proposed. With this proposed method, the conventional global registration results are enhanced, and hence better shape-based segmentation results are obtained. More specifically the motivation and contribution of this chapter can be written as follows:

i.) The level sets formulations, which are based on only the intensity and / or edge information (such as what Chen-Vase [23], Li et al. [25], Gao et al. [49] proposed) fail when the image has noise or the object has various missing parts and occlusions. This dissertation solves common problems with integrating the prior shape information.

ii.) In the shape registration methods, the dissimilarity measures proposed by Paragios et al. [47], Rousson et al. [13], Tsai et al. [14], and Huang et al. [31], and etc. have limitations to capture the object-of-interest if the source and target shapes have inhomogeneous scale differences. Limited shape model embedding transformation (homogeneous scales) is used. In this dissertation, the geometrical scaling is proposed as an approximation, since the signed distance function (SDF) is not invariant to inhomogeneous scaling. The proposed approximation may not be enough to perfectly align the shapes. Hence, the other shape probability density function (PDF) term, which will be explained in detail in the following section, is required. The shape variations are modelled using a probabilistic functions. New probabilistic shape models are proposed to enhance the conventional shape based segmentation results.

iii.) Active appearance models method, which was originally proposed by Cootes et al. [9], has been used in many applications. However, the shape model

should be initialized very close to the object-of-interest for the originally proposed method. It should be noted that there have been improvements on AAM to eliminate the dependency on the shape initialization. In this dissertation, the originally proposed AAM method is referred.

D. Method

In this work, two energy functionals are proposed to be minimized as published in [30]. The first functional is to extract object regions using image intensities only with a statistical level set evolution as described in [24]. This step is needed to obtain the image feature to be used in the shape registration process. The second functional depends on the dissimilarity measure between the shape model and the resulting contour which is obtained in the first phase. The weighting coefficients of the dynamic shape model and transformation matrix are estimated using the simplex optimization method. The proposed methods are described in the following three sections: i) Shape model reconstruction, and ii) initial segmentation using only intensity model, and iii) proposed shape model registration process. The proposed framework is shown in Figure 8.

1. Shape Model Reconstruction

a. Shape Representation In this work, the shape is represented using the signed distance function which is used firstly in registration by Paragios et al. [47]. Let $\mathbf{I} : \Omega \rightarrow R$ be an $n - D$ image usually $n = 2$ or $n = 3$, $\phi : \Omega \rightarrow R$ be a function that refers to a distance function representation for a given shape / contour $\mathcal{S}$ where $\Omega \subset R^n$ be an image domain which is bounded. The shape can be represented as follows:

$$\phi_{\mathcal{S}}(x, y) = \begin{cases} 0, & (x, y) \in \mathcal{S} \\ -ED((x, y), \mathcal{S}) > 0, & (x, y) \in \mathcal{R}_{\mathcal{S}} \\ +ED((x, y), \mathcal{S}) < 0, & (x, y) \in \Omega - [\mathcal{R}_{\mathcal{S}}] \end{cases} \tag{22}$$

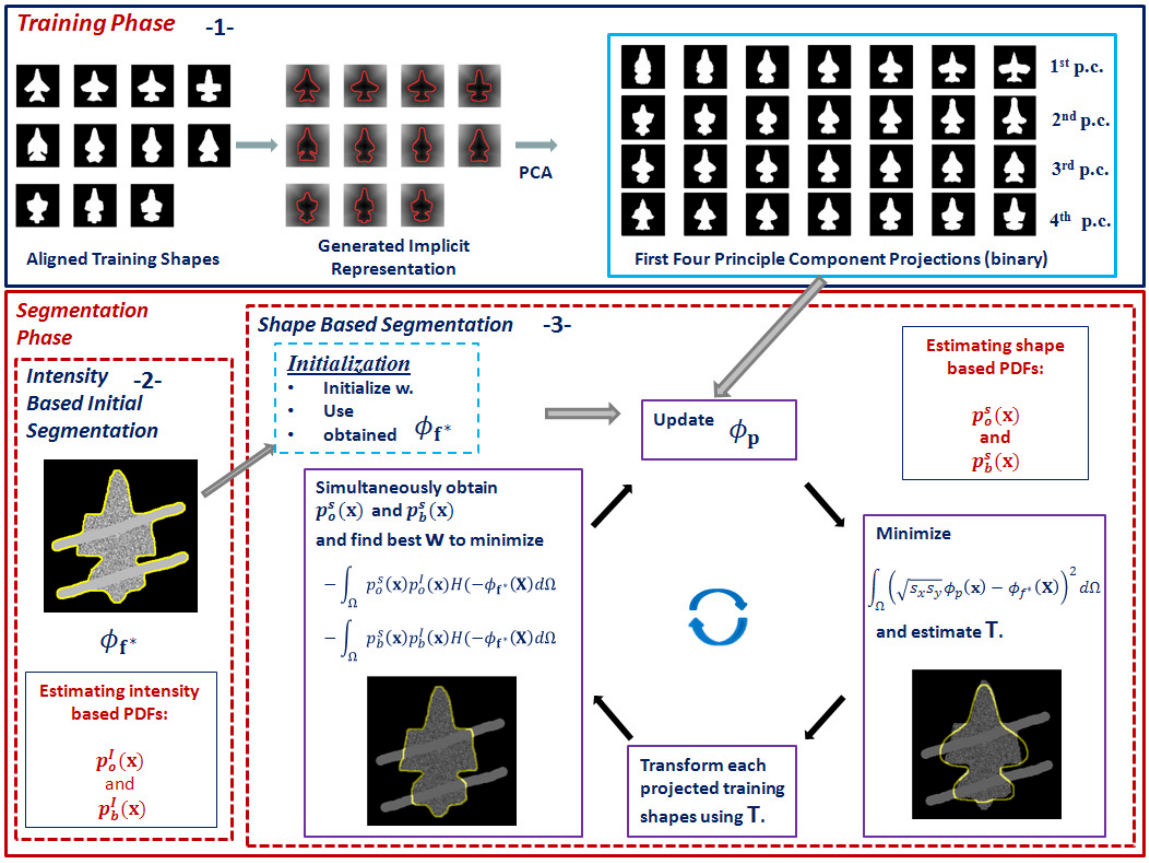

FIGURE 8 – The general framework is shown. The steps can listed as follows: 1) Obtain shape projections to define the shape variability. 2) The intensity based segmentation. The yellow contour shows the automatic segmentation region. 3) The shape based segmentation with iterative shape reconstruction.

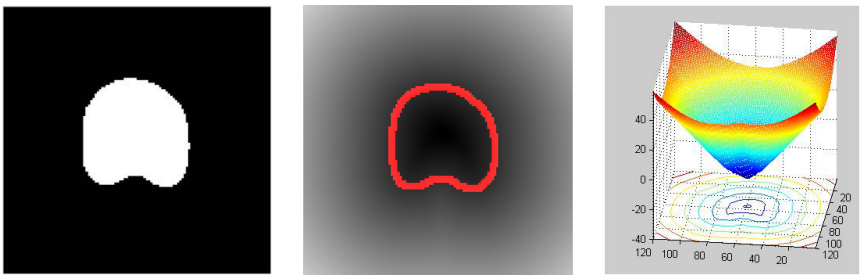

(a) (b) (c)

FIGURE 9 – An example representation of signed distance function. (a) A vertebral body (VB) shape, (b) signed distance function as an image intensity representation, (c) level set representation of SDF.

where $\mathcal{R}_{\mathcal{S}}$ represents the inside region of the shape $\mathcal{S}$. Let (u, v) represents an pixel location on $\mathcal{S}$. For $\forall(x, y) \in \phi$, the distance between any (x, y) point and its nearest surface point can be calculated as follows:

$$ED((x, y), \mathcal{S}) = \min_{(u,v)\in\mathcal{S}} \sqrt{(u-x)^2 + (v-y)^2}. \tag{23}$$

Figure 9 shows an example of a shape representation using the distance function.

b. Principle Component Analysis (PCA) on the Training Shapes (Offline) In this step, the objective is to globally obtain the most important information of training shapes. Let the training set consists of a set of aligned training shapes $\{C_1, \ldots, C_Z\}$; with SDFs $\{\widehat{\phi}_1^t, \ldots, \widehat{\phi}_Z^t\}$. An example is shown in Figure 43. Using the technique developed in [12], the mean level set function of the training shapes is obtained, ϕ_M, as the average of these Z signed distance functions, $\phi_M = (1/Z)\sum \widehat{\phi}_i^{\,t}$. To extract the shape variabilities, ϕ_M is substracted from each of the training SDFs. The obtained mean-offset functions can be represented as $\{\widetilde{\phi}_1^t, \ldots, \widetilde{\phi}_Z^t\}$. These new functions are used to measure the variabilities of the training shapes.

The shape variability matrix Ψ is defined as $\Psi = [\widetilde{\phi}_1^t, \ldots, \widetilde{\phi}_Z^t]$. It should be noted that, $\widetilde{\phi}_i^t$ is the vector representation of ϕ_i^t. Let λ_i be each eigenvalue of the shape variability matrix $\mathcal{V} = \frac{1}{Z}\Psi^T\Psi$. To retrain r percent of the variation in the training set, K modes can be chosen satisfying

$$\sum_{i=1}^{K} \lambda_i \geq \frac{r}{100} \sum_{i=1}^{Z} \lambda_i. \tag{24}$$

The projected training shapes is obtained as follows:

$$\phi_{\{i,h\}}^t = \phi_M + \mathbf{U}\mathbf{b}_{\{i,h\}} \tag{25}$$

where $\mathbf{U}$ is the matrix which contains K number of eigenvectors, and $\mathbf{b}$ is the set of model parameters which can be described as

$$\mathbf{b}_{\{i,h\}} = h\sqrt{\lambda_i} \tag{26}$$

where $i = \{1, \ldots, K\}$, $h = \{-\alpha, \ldots, \alpha\}$, and α is a constant which can be chosen arbitrarily.

The new SDF of training shapes are represented as $\{\phi_1^t, \ldots, \phi_N^t\}$ instead of $\{\phi_{\{1,h\}}^t, \ldots, \phi_{\{K,h\}}^t\}$ where N is the multiplication of K and standard deviation in eigenvalues (the number of elements in h). Also, the number of K and standard deviation in eigenvalues can be selected by trail-and-error. The shape model is required to capture the variations in the training set. In this study, it is accepted that $\alpha = 3$ which means that $h = \{-3, -2, -1, 0, 1, 2, 3\}$, and $K = 4$. These number are chosen to obtain the shape variability well.

An example projections of training images are shown in Figures 11-12. Figure 11 shows obtained projections of 80 training images with respect to four modes (shown in each row). The representation of shape projection is shown in Figure 12. In this figure, the representation of only the 1st projection component (p.c.s) is shown. The shape variation of the first and fourth p.c.s is shown in 13. The shape variation decreases from the first to the fourth (or last) p.c. respectively. Hence, selection of 'K' value with Eq. 24 helps to capture the necessary shape variation with minimum information.

c. The Dynamic Shape Based Probability Density Function The weighted shape model is considered to be a weighted sum of the transformed signed distance maps as follows:

$$\phi_{\mathbf{p}} = \sum_{j=1}^{N} w_j \phi_j^t, \tag{27}$$

where ϕ_j^t represents the map of the training shapes marked by t after the PCA method. Shape weighting coefficient vector is represented as $\mathbf{w} = [w_1, \ldots, w_N]^T$. By varying these weights, $\phi_{\mathbf{p}}$ can cover all values of the projected training distance maps, hence, the shape model changes according to all of the given shapes and weights.

In this study, a new probabilistic and dynamic shape model is synthesized using the first four p.c. as described in II.D.1.b. Two shape probability density

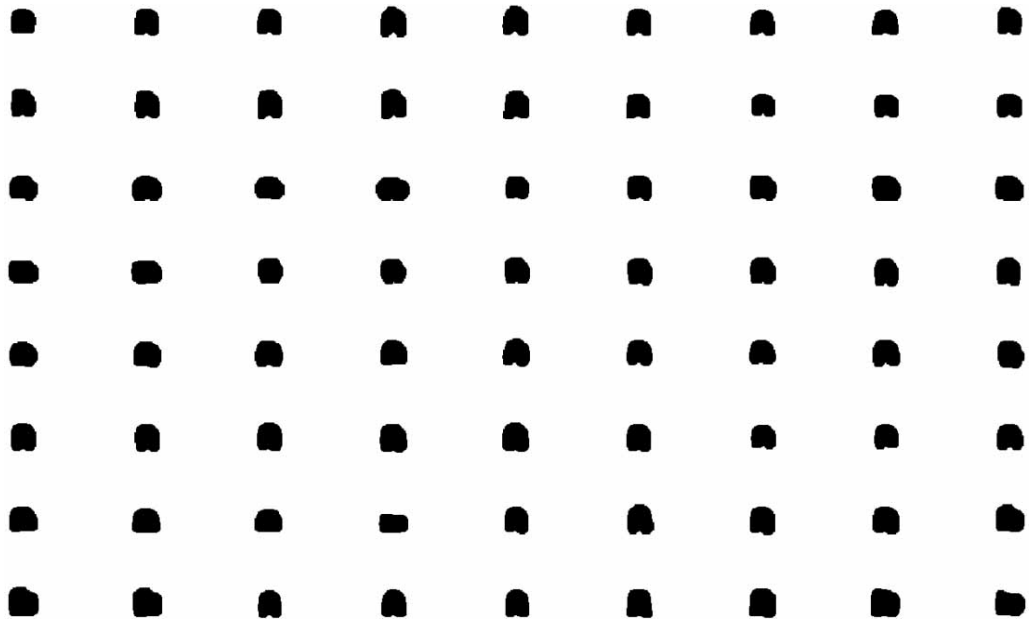

FIGURE 10 – The training VB images. In this experiment, 80 VB shapes which are obtained from 20 different patients and different regions (such as cervical, thoracic, and lumbar spine bone sections) are used. These images are processed using the PCA method to obtain most important projections which are enough to represent the shape variation in the vertebral body.

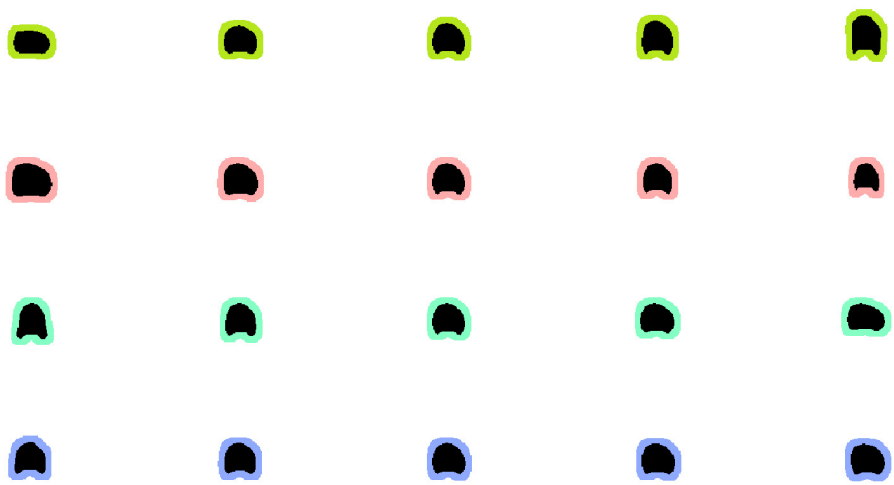

(a) (b) (c) (d) (e)

FIGURE 11 – Projections of 80 training VB shapes shown in Figure 43. First to last rows (from $i = 1$ to $i = 4$) correspond to the projected shapes of the first to fourth strongest eigenvector representation. Projected shapes with corresponding eigenvalues are shown in (a) $\phi^t_{\{i,-3\}} = \phi_M + \mathbf{U}\mathbf{b}_{\{i,-3\}}$, (b) $\phi^t_{\{i,-1\}} = \phi_M + \mathbf{U}\mathbf{b}_{\{i,-1\}}$, (c) $\phi^t_{\{i,0\}} = \phi_M + \mathbf{U}\mathbf{b}_{\{i,0\}}$, (d) $\phi^t_{\{i,1\}} = \phi_M + \mathbf{U}\mathbf{b}_{\{i,1\}}$, and (e) $\phi^t_{\{i,3\}} = \phi_M + \mathbf{U}\mathbf{b}_{\{i,3\}}$.

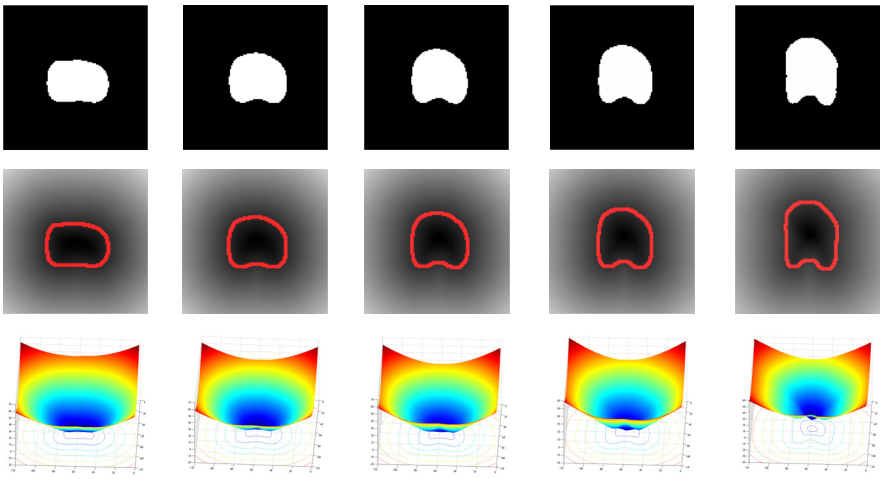

(a) (b) (c) (d) (e)

FIGURE 12 – Implicit shape representation of 1st projections. Shapes with corresponding eigenvalues are shown in (a) $\phi^t_{\{1,-3\}}$, (b) $\phi^t_{\{1,-1\}}$, (c) $\phi^t_{\{1,0\}}$, (d) $\phi^t_{\{1,1\}}$, and (e) $\phi^t_{\{1,3\}}$. The first row shows the binary images. The second and third rows show the SDF shape representation in 2D and 3D, respectively.

functions which represent the probability of i) the object (inside of a boundary) and ii) background regions (outside of a boundary) are obtained as follows:

$$p^s_o(\mathbf{x}) = \frac{\sum_{j=1}^{N} w_j |\phi^t_j(\mathbf{x})| H(-\phi^t_j(\mathbf{x}))}{\sum_{j=1}^{N} w_j |\phi^t_j(\mathbf{x})|}, \tag{28}$$

$$p^s_b(\mathbf{x}) = \frac{\sum_{j=1}^{N} w_i |\phi^t_j(\mathbf{x})| H(\phi^t_j(\mathbf{x}))}{\sum_{j=1}^{N} w_j |\phi^t_j(\mathbf{x})|}, \tag{29}$$

where $H(.)$ is the Heaviside step function as a smoothed differentiable version of the unit step function. This step is integrated to the registration step which is described in section II.D.3, hence the shape model is dynamically reconstructed in the registration process.

Figure 14 shows the detailed description of the shape model where the shape weighting coefficients are normalized, i.e. $\mathbf{w} = \{w_1, \ldots, w_N\} = \{1/N, \ldots, 1/N\}$. The green color shows the background region which does not have any intersection with any training shape. The blue color shows the object region which is the

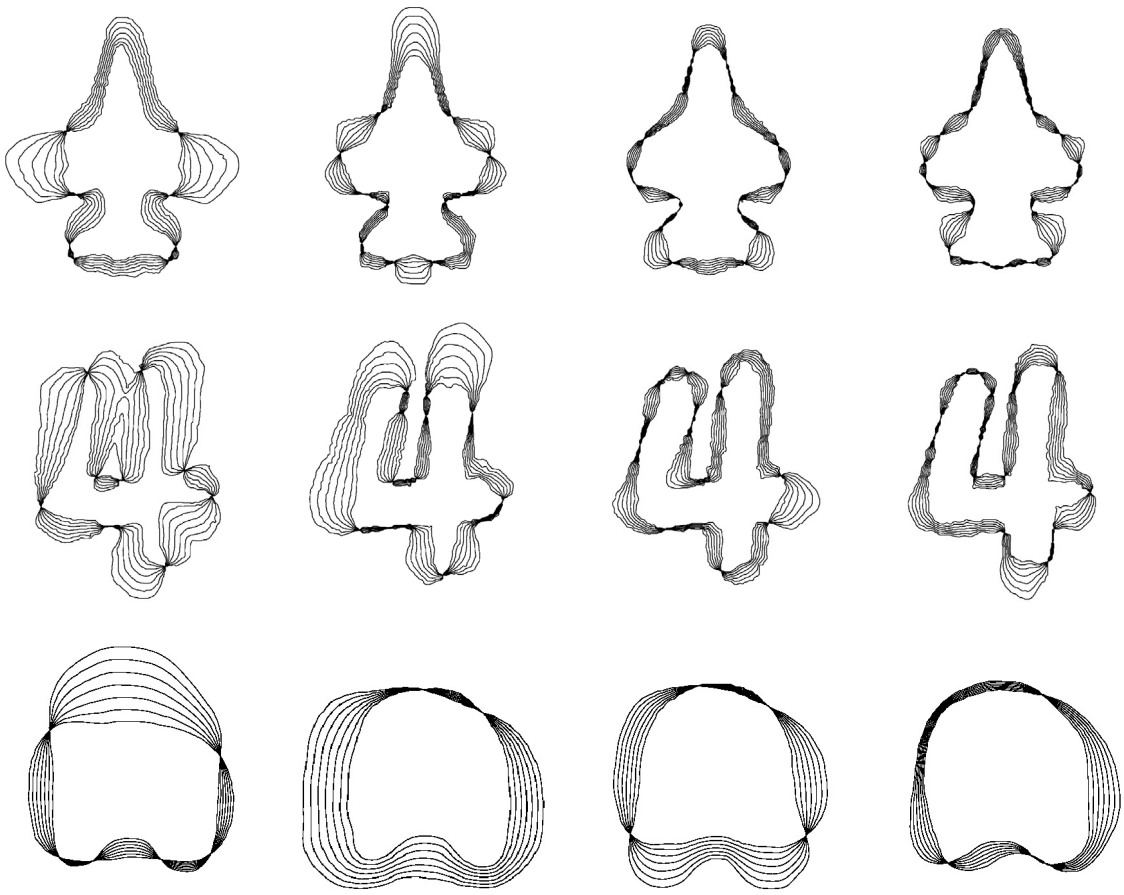

1st p.c. 2nd p.c. 3rd p.c. 4th p.c.

FIGURE 13 – Sampling up to 3 standard deviations (from $\mathbf{b}_{\{i,-3\}}$ to $\mathbf{b}_{\{i,3\}}$) along the first four principle components (p.c.) (where $i = \{1, 2, 3, 4\}$ for the first four p.c.) from the mean for a set of jet airplane, number "four", and 80 training vertebral body (VB) shapes.

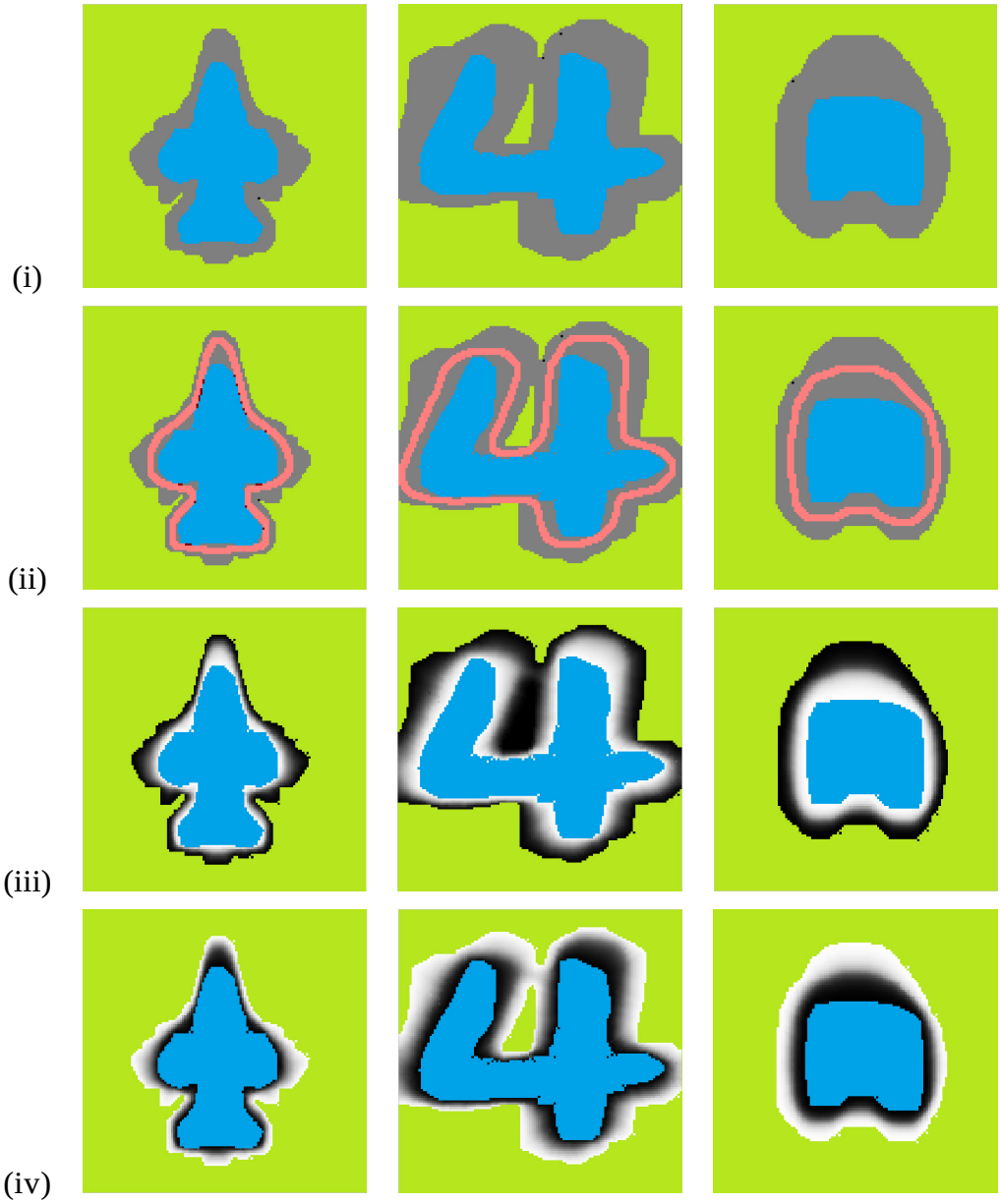

(Jet airplane) (Number ”4”) (Vertebral body)

FIGURE 14 – The shape models of each data that are used in the experiments. The green color shows the background region which does not have any intersection with any training shape. The blue color shows the object region which is the intersection of all projected training shapes. (i) The gray color represents the variability region that can be described as the union of all projected training shapes minus the intersection of those shapes. In this variability region, the object and background probabilistic shapes are defined. (ii) The red color shows the average shape ($\phi_{\mathbf{p}}$). (iii) The object (p_o^s) and (iv) background (p_b^s) shapes are modelled in the variability region which the pixel values are defined in $(0:1)$.

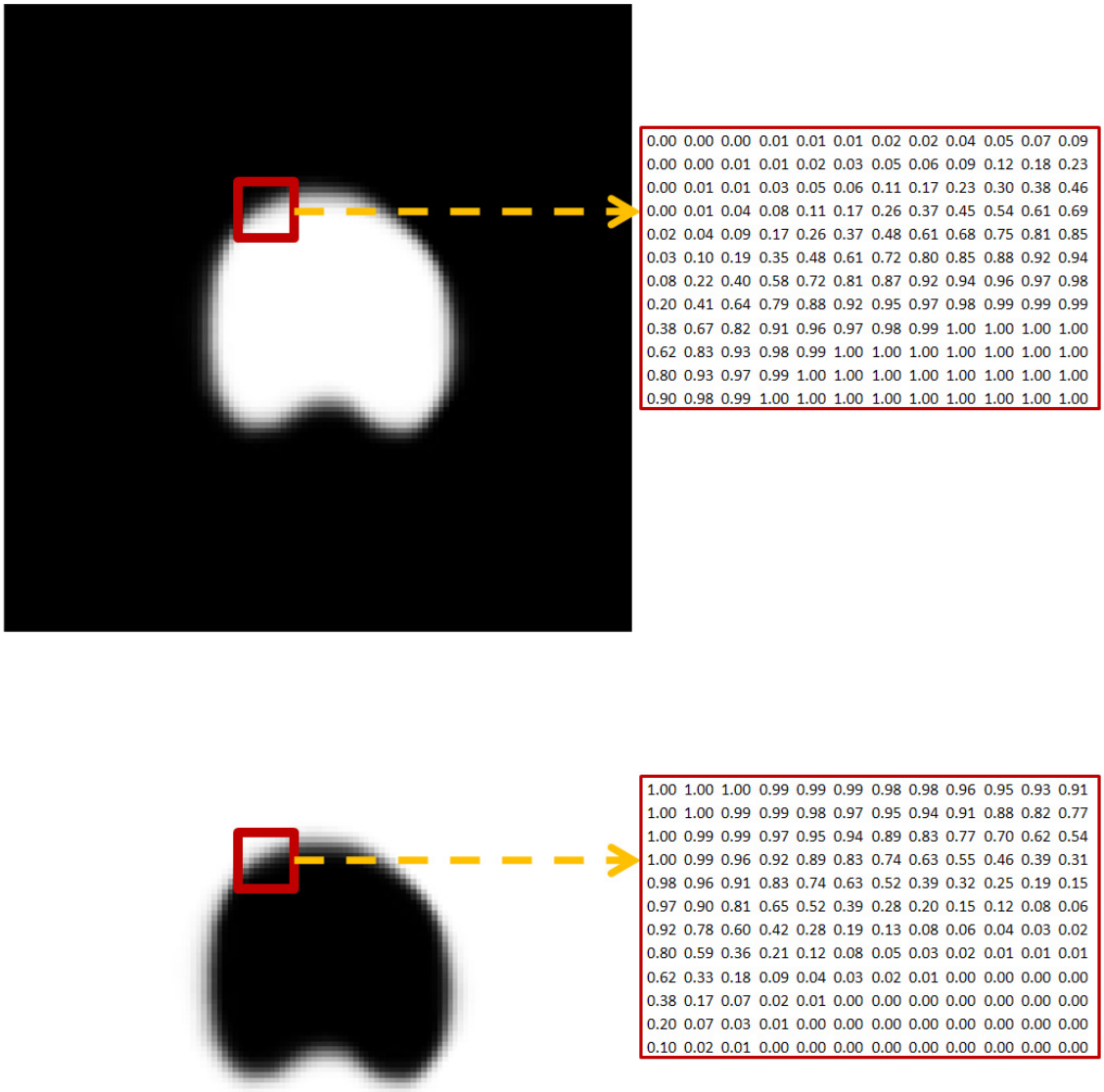

FIGURE 15 – The constructed object (p_o^s in the first row) and background (p_b^s in the second row) models. The red squares show the same location in both images. The numbers shown in the right side are the pixel information at each pixel $\mathbf{x}$ in the red square.

intersection of all projected training shapes. In (i), the gray color represents the variability region that can described as the union of all projected training shapes minus the intersection of those shapes. In this variability region, the object and background probabilistic shapes are defined. The red color, in (ii), shows the average shape representation ($\phi_{\mathbf{p}}$) for normalized values of $\mathbf{w}$. This shape model is used to estimate the registration parameters using the proposed dissimilarity measure. The object (p_o^s) and background (p_b^s) shapes are modelled in the variability region. These probability density functions (PDFs) are used to obtain the shape weighting coefficients and enhance the global registration results. It should be noted that $\phi_{\mathbf{p}}$, p_o^s, and p_b^b are reconstructed at each registration iteration. An example of the probabilistic shape models in real values is shown in Figure 15.

In the next section, the initial segmentation using only the intensity based segmentation is described. The shape model is to be embedded into the image domain. In the registration step, the shape model is embedded to the initially segmented region by minimizing the new energy function described in section II.D.3.

2. Intensity Segmentation

The level set segmentation framework contains a moving front, denoted by $\mathcal{C}$, which is implicitly represented by the zero level of a higher dimensional functional, ϕ, that is: $\mathcal{C}(t) = \{\mathbf{x} : \phi(\mathbf{x}, t) = 0\}$. It is assumed that the data to be segmented consists of two classes: object and background. Suppose that the intensity probability density function (pdf) within each of these two regions, denoted as p_o^I and p_b^I, can be modeled using a Gaussian probability distribution whose parameters are adaptively updated during the course of evolution of the level set function. The segmentation process starts by initializing the level set function as the signed distance function of a circle centered at a seed point(s) that is placed automatically using the Matched filter [64] or with manual annotation. Then, the statistical parameters corresponding to the *pdf* for the object and background are estimated as

follows:

$$\mu_o = \frac{\int_\Omega I(\mathbf{x})H(-\phi_{\mathbf{f}^*}(\mathbf{x}))d\Omega}{\int_\Omega H(-\phi_{\mathbf{f}^*}(\mathbf{x}))d\Omega}, \quad \mu_b = \frac{\int_\Omega I(\mathbf{x})H(\phi_{\mathbf{f}^*}(\mathbf{x}))d\Omega}{\int_\Omega H(\phi_{\mathbf{f}^*}(\mathbf{x}))d\Omega}, \tag{30}$$

$$\sigma_o^2 = \frac{\int_\Omega (I(\mathbf{x}) - \mu_o)^2 H(-\phi_{\mathbf{f}^*}(\mathbf{x}))d\Omega}{\int_\Omega H(-\phi_{\mathbf{f}^*}(\mathbf{x}))d\Omega}, \quad \sigma_b^2 = \frac{\int_\Omega (I(\mathbf{x}) - \mu_b)^2 H(\phi_{\mathbf{f}^*}(\mathbf{x}))d\Omega}{\int_\Omega H(\phi_{\mathbf{f}^*}(\mathbf{x}))d\Omega}, \tag{31}$$

$$\pi_o = \frac{\int_\Omega H(-\phi_{\mathbf{f}^*}(\mathbf{x}))d\Omega}{\int_\Omega d\Omega}, \quad \pi_b = \frac{\int_\Omega H(\phi_{\mathbf{f}^*}(\mathbf{x}))d\Omega}{\int_\Omega d\Omega}, \tag{32}$$

where μ, σ, and π are the mean, standard deviation, and prior probability of the corresponding pdf [24]. Here, $H(z)$ is the Heaviside step function as a smoothed differentiable version of the unit step function, and ϕ represents the signed distance function of the evolving contour. Object and background regions are represented by $H(-\phi)$ and $H(\phi)$, respectively. The pixel position, (x, y), is represented as $(\mathbf{x})$. The intensity based energy term is modeled to maximize posterior probability of each region as follows:

$$E_{intensity}(\phi_{\mathbf{f}^*}) = -\int_\Omega p_o^I(I(\mathbf{x}))H(-\phi_{\mathbf{f}^*})d\Omega - \int_\Omega p_b^I(I(\mathbf{x}))H(\phi_{\mathbf{f}^*})d\Omega + \epsilon L, \tag{33}$$

where L is the front length of the surface area and ϵ is a constant between 0 and 1. The change of the level set function with time is calculated by the Euler-Lagrange with the gradient descent given as :

$$\frac{\partial \phi_{\mathbf{f}^*}}{\partial t} = -\frac{\partial E_{intensity}}{\partial \phi_{\mathbf{f}^*}} = \delta(\phi_{\mathbf{f}^*})[p_o^I(I) - p_b^I(I)] + \epsilon\kappa, \tag{34}$$

where κ is the curvature of the evolving contour (or derivative of L) and δ is the derivative of the Heaviside step function. By solving this gradient descent formulation, the initial segmented region ($\phi_{\mathbf{f}^*}$) is obtained as shown in Figure 75(c). In the next section, how the shape model is used is defined in Eqs. 27, 56, and 57 by minimizing the shape energy function (E_{shape}).

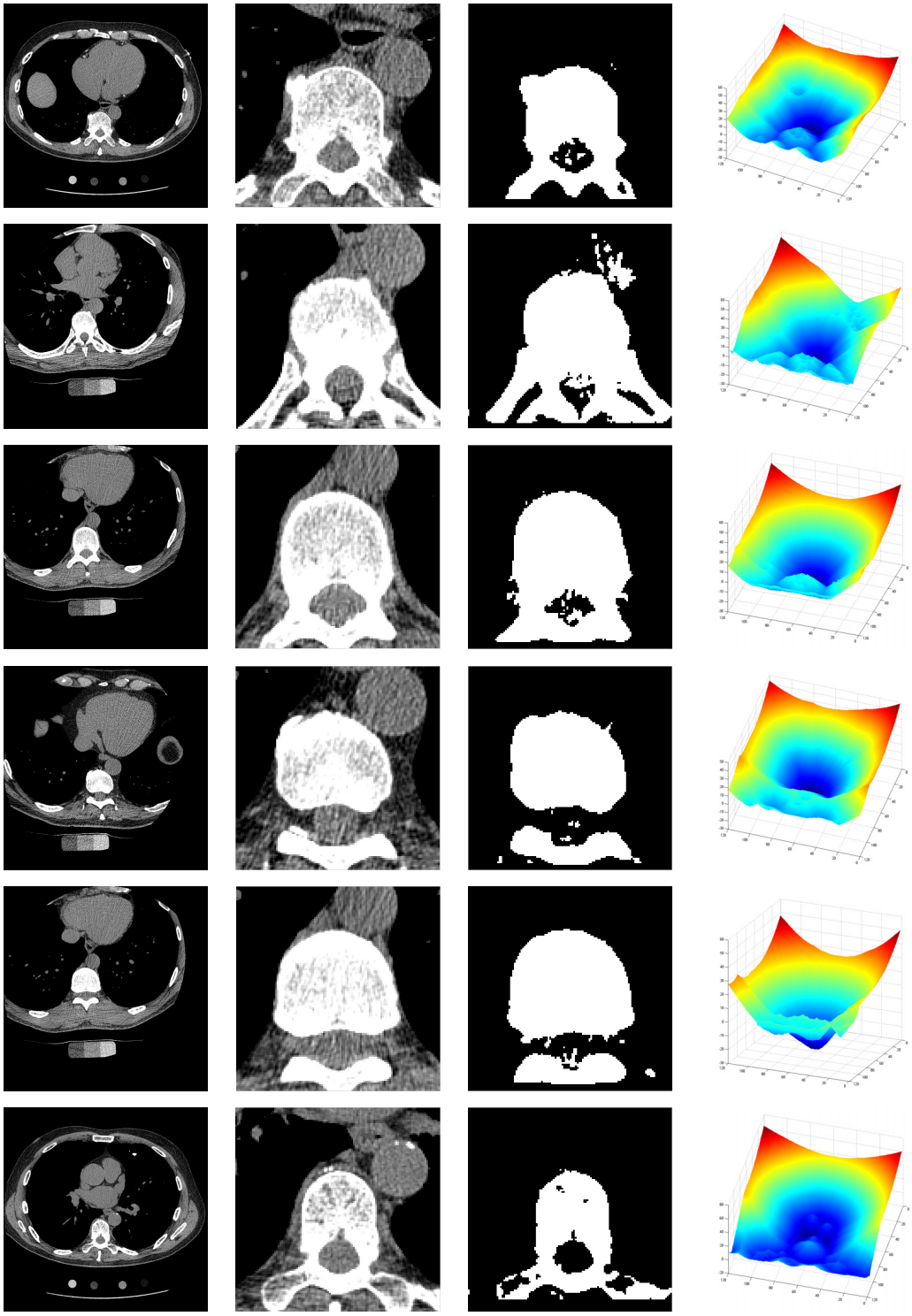

(a) (b) (c) (d)

FIGURE 16 – An example of the initial labeling. (a) Original CT image, (b) detection of the VB region, (c) the initial labeling, $\mathbf{f}^*$, and (d) the SDF of the initial segmentation ($\mathbf{f}^*$) which is used in the registration phase.

3. Embedding Shape Model with the Image Domain

After the object region is initially segmented, the shape model is embedded into this domain by minimizing the new energy functional. It should be noted that the shape representation used in this work changes the problem from a 2D/3D shape to higher dimensional vector representation. A transformation matrix, $\mathbf{T}$, that gives pixelwise correspondences between the two shape representations ϕ_{source} and ϕ_{target} is required. The source and target shapes and transformation can be defined as follows:

- Source shape ($\phi_{\mathbf{p}}$): Shape which is kept unchanged and is used as a reference. This shape can be written as a function $\phi_{\mathbf{p}} : R^2 \rightarrow R$ for $\forall \mathbf{x} \in \Omega_{\mathbf{p}}$.

- Target shape ($\phi_{\mathbf{f}^*}$): Shape which is geometrically transformed to the source shape. This information can be written as a function $\phi_{\mathbf{f}^*} : R^2 \rightarrow R$ for $\forall \mathbf{y} \in \Omega_{\mathbf{f}^*}$.

- Transformation ($\mathbf{T}$): The function is used to warp the target image to reform to the geometry of the reference image. The transformation can be written as a function $\mathbf{T} : R^2 \rightarrow R^2$ which is applied to a point $\mathbf{x}$ in $\phi_{\mathbf{p}}$ to produce a transformed point which is calculated as $\mathbf{X} = \mathbf{T}(\mathbf{x})$.

In this study, an affine transformation, which allows translation, rotation, and scaling is used. Some authors defined the affine transformation as the rigid transformation plus scaling. Affine transformations involving shearing (projection) are called projective transformation. The affine transformation will map lines and planes into lines and planes but does not preserve length and angles. The transformation is used to register $\phi_{\mathbf{p}}$ to $\phi_{\mathbf{f}^*}$ with scale, rotation, and translation parameters. For the 2D case, the transformation has scaling, rotation, and translation components are represented as follows:

$$\mathbf{S} = \begin{bmatrix} s_x & 0 \\ 0 & s_y \end{bmatrix}, \ \mathbf{R} = \begin{bmatrix} cos(\theta) & -sin(\theta) \\ sin(\theta) & cos(\theta) \end{bmatrix}, \ \mathbf{Tr} = [t_x, t_y]^t. \tag{35}$$

The transformation will be in the form:

$$\mathbf{T}(\mathbf{x}) = \mathbf{X} = \mathbf{SRx} + \mathbf{Tr} \tag{36}$$

where $\mathbf{X} \in \phi_{\mathbf{f}^*}$ and $\mathbf{x} \in \phi_{\mathbf{p}}$.

The proposed dissimilarity measure is

$$E_{shape}(\phi) = \rho E_1 + E_2, \tag{37}$$

where ρ is the normalization constant which controls the relationship between the first and second terms which can be described as follows:

$$E_1(\mathbf{T} \mid \phi_{\mathbf{p}}, \phi_{\mathbf{f}^*}) = \int_{\Omega} (\sqrt{s_x s_y}\phi_{\mathbf{p}}(\mathbf{x}) - \phi_{\mathbf{f}^*}(\mathbf{X}))^2 d\Omega, \tag{38}$$

$$\begin{aligned} E_2(\mathbf{w} \mid \phi_{\mathbf{f}^*}, p_{o,\,b}^{s,I}) = &- \int_{\Omega} p_o^s(\mathbf{x}) p_o^I(\mathbf{x}) H(-\phi_{\mathbf{f}^*}(\mathbf{X})) d\Omega \\ &- \int_{\Omega} P_b^s(\mathbf{x}) p_b^I(\mathbf{x}) H(\phi_{\mathbf{f}^*}(\mathbf{X})) d\Omega. \end{aligned} \tag{39}$$

The first term of the proposed energy formulation is the (sum-of-squared distance) SSD of matched distances. Distance changes anisotropically in x-y directions. Thats why the geometric mean between s_x and s_y as an approximation is proposed, since the SDF is not invariant to inhomogeneous scaling. The first term helps to estimate the registration parameters ($s_x,\ s_y,\ \theta,\ t_x,\ t_y$), iteratively. This approximation may not be enough to perfectly align the shapes. Hence, it is needed to add the other shape PDF term. After the registration parameters are estimated the shape model, $\phi_{\mathbf{p}}$, and the projected training shapes, $\{\phi_1^t, \ldots, \phi_N^t\}$, are registered to the target domain using the affine transformation. Using this process, all prior shapes are transformed into the image domain and will be used to enhance global registration results. This also maximized the posterior probability with respect to shape object / background region.

When transforming the shape model into the image domain, a pixel inside the shape needs to have bigger object probability. At the same time, this pixel needs to have smaller background probability as well. So, the second term maximizes the probability for object pixels to be correctly classified as internal points. The same will happen for the background points. This step helps to estimate the shape weighting coefficients ($\mathbf{w} = w_1, \ldots, w_N$) and to refine the result of the first component more accurately. To minimize the second term, new probabilistic shape models are reconstructed based on estimated $\mathbf{w}$ at each iteration. After the optimum shape parameter $\mathbf{w}$ is found, $\phi_{\mathbf{p}}$ is updated and another general iteration begins. It should be noted that, in the general iterative process, each energy minimization step has its own iterative optimization.

The registration and weighting parameters ($s_x,\ s_y,\ \theta,\ t_x,\ t_y,\ w_1, \ldots,\ w_N$) are computed to minimize E_{shape} using the Nelder-Mead simplex optimization method which was first proposed by Nelder and Mead [65] and proved using theoretical results by Lagarias et al [66]. The Nedler-Mead method aims to minimize a scalar-valued nonlinear function of n variables using function values, hence it is one of the direct search methods. For more information see [65, 66].

E. Experiments and Discussion

To assess the accuracy and robustness of the proposed framework, it is tested using clinical data sets as well as synthetic and phantom images. All algorithms are implemented on a PC with a 3Ghz AMD Athlon 64 X2 Dual processor, with 3GB RAM. First, the experimental results on synthetic images are described. Second, validation on European Spine Phantom (ESP) with various noise levels will be shown. Effect of initialization will be evaluated. Finally, the VB segmentation results with different initializations are shown.

1. Experiments on Synthetic Shapes

The initialization of the source shape is a very crucial step in the shape registration process. If the initial position, scale, and rotation are far from the desired parameters, the resulting shape would not be acceptable. The parameter initialization effect on synthetic images are validated. Figure 17 shows results of shape based segmentation with different initialization. Shape registration results at each iteration with different initialization are shown. The first row shows the results when the source shape is initialized with $\theta = 30^o$ rotation degrees. The second row shows the results when the source shape is initialized with $\theta = -30^o$ rotation degrees and $s_x = 1.2,\ s_y = 1.2$ scaling factors. The third row shows the results when the source shape is initialized with $s_x = 1.2,\ s_y = 1.2$ scaling factors and $t_x = 20,\ t_y = -20$ translation factors. It should be noted that these initial parameters are chosen arbitrarily.

Also, each component of Eq. 37 affects the segmentation results. Figures 18-19 show different results using only the first as well as all components in this equation respectively. As seen in the results, the first component is useful for an approximate transformation of the shape model. The second component of the proposed dissimilarity measure (Eq. 37) enhances the segmentation. Hence, the proposed dissimilarity measure is able to improve the global registration results.

The proposed method is also validated with occlusions and missing information of shapes. Shape based segmentation is useful when the target shape has some occlusions and missing information. Figures 20 and 22 show results on syntectic jet airplane and number four images with some missing information and occlusions. Experimental results prove that the desired shape information is captured. In these figures, the segmentation results using only intensity information are shown. The results show that occlusions and missing information mislead those methods based only on intensity model. Using the shape prior information the desired shapes are recovered. For each case the source shape is initialized with

transformation factors.

The proposed method is compared with two closest works described in [14, 47]. In these methods, the dissimilarity measures have limitations to capture the object-of-interest if the source and target shapes have inhomogeneous scale differences. Limited shape model embedding transformation (homogeneous scale) is used. Figures 23-25 show the results when the target shapes have (i) homogeneous, and (ii-iv) inhomogeneous scale differences. Because dissimilarity measures of two alternative methods discard a possible scale difference in x or y directions, they fail when the target shapes are scaled inhomogeneities in x-y directions. For instance, in (i) the target shape has scaling factors as $s_x = 1, s_y = 1$ which is homogeneous scaling difference. However, in (ii)-(iv), the scaling factors are $s_x = 0.7, s_y = 1.3$, $s_x = 1.2, s_y = 0.7$, and $s_x = 0.4, s_y = 0.7$ which are inhomogeneous scaling differences. Thats why the geometric mean between s_x and s_y as an approximation is proposed, since the SDF is not invariant to inhomogeneous scaling. The results prove that the proposed method overcomes the problems existing in two closest works.

2. Experiments on Vertebral Body Images

In the experiments, the proposed method is tested on clinical CT images to segment vertebral bodies (VBs) as well as synthetic images. The vertebra consists of the VB and spinal processes. (See Figure 26 for the region of interest). The vertebral BMD measurements and fracture analysis are restricted to the vertebral bodies. Spinal processes and ribs should not be included in the BMD measurements. As seen in the images, the VB segmentation is not an easy task and VBs need to be separated from the ribs and spinal processes which have similar gray level information.

a. Validation Using the Phantom In the experiments, the ESP, which is an accepted standard for quality control [68] in bone densitometry, is used to validate

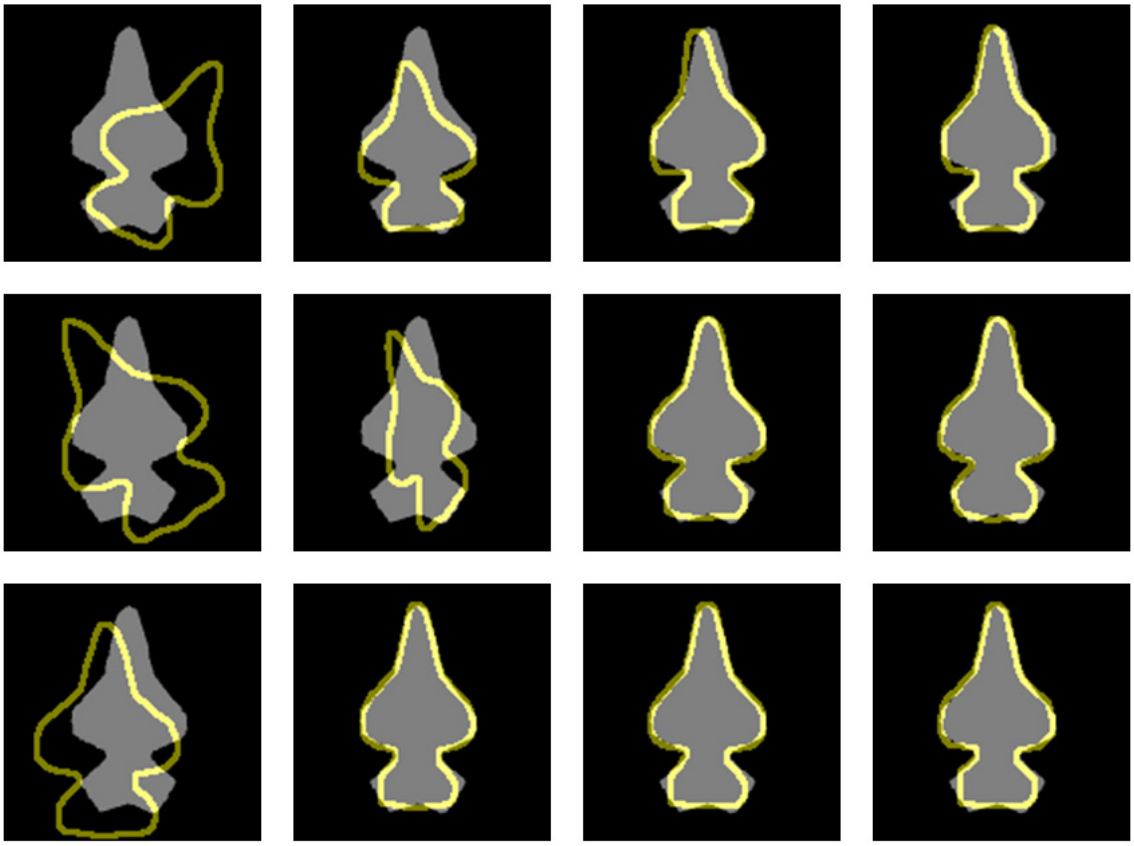

(a) (b) (c) (d)

FIGURE 17 – Shape based segmentation results on another subject at each iteration with different initialization. The results at each iteration are shown in (a)-(d). (First row) The source shape is initialized with $\theta = 30^o$ rotation degrees. (Second row) The source shape is initialized with $\theta = -30^o$ rotation degrees and $s_x = 1.2,\ s_y = 1.2$ scaling factors. (Third row) The source shape is initialized with $s_x = 1.2,\ s_y = 1.2$ scaling factors and $t_x = 20,\ t_y = -20$ translation factors.

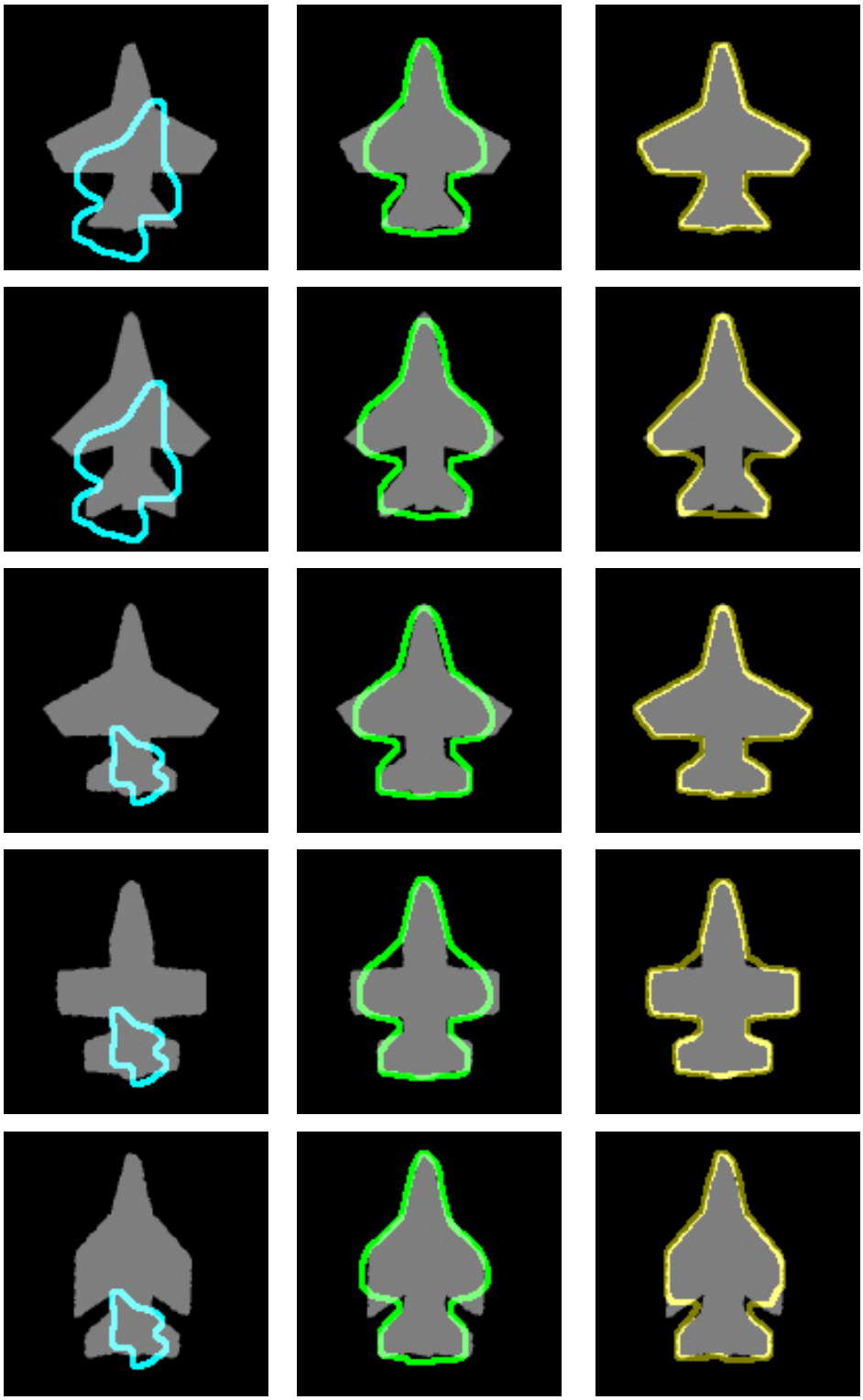

(a: Initialization) (b: 1st term of Eq. 37) (c: All terms of Eq. 37)

FIGURE 18 – Example 1: The effects of each component of Eq. 37 on different jet shapes with different initializations. (a) The initialization of the shape model. (b) The results using only the first term. (c-Proposed) The result using all terms.

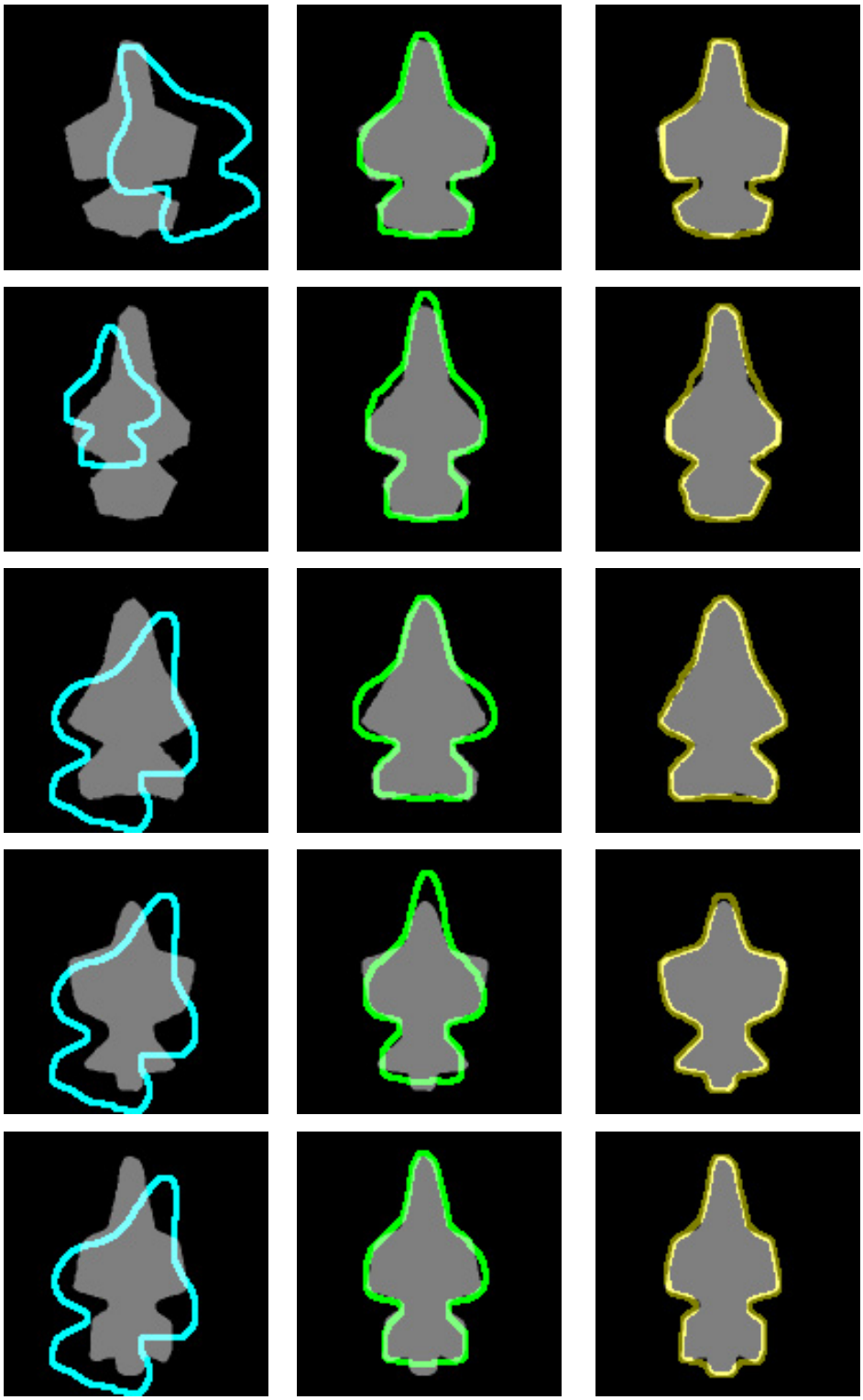

(a: Initialization) (b: 1st term of Eq. 37) (c: All terms of Eq. 37)

FIGURE 19 – Example 2: The effects of each component of Eq. 37 on a jet shape with different initializations. (a) The initialization of the shape model. (b) The results using only the first term. (c-Proposed) The result using all terms.

(a: Intensity) (b: Initialization) (c: 1st term of Eq. 37) (d: All terms of Eq. 37)

FIGURE 20 – Example 3: Segmentation results of a synthetic jet airplane images with different missing information and initializations. (a) The only intensity based segmentation results. (b) Different shape model initialization. (c) The results using only the first term of Eq. 37. (d) The segmentation of the proposed method (the red and yellow colors show the contour of the ground truth shape region, and the contour of the automatically segmented region, respectively).

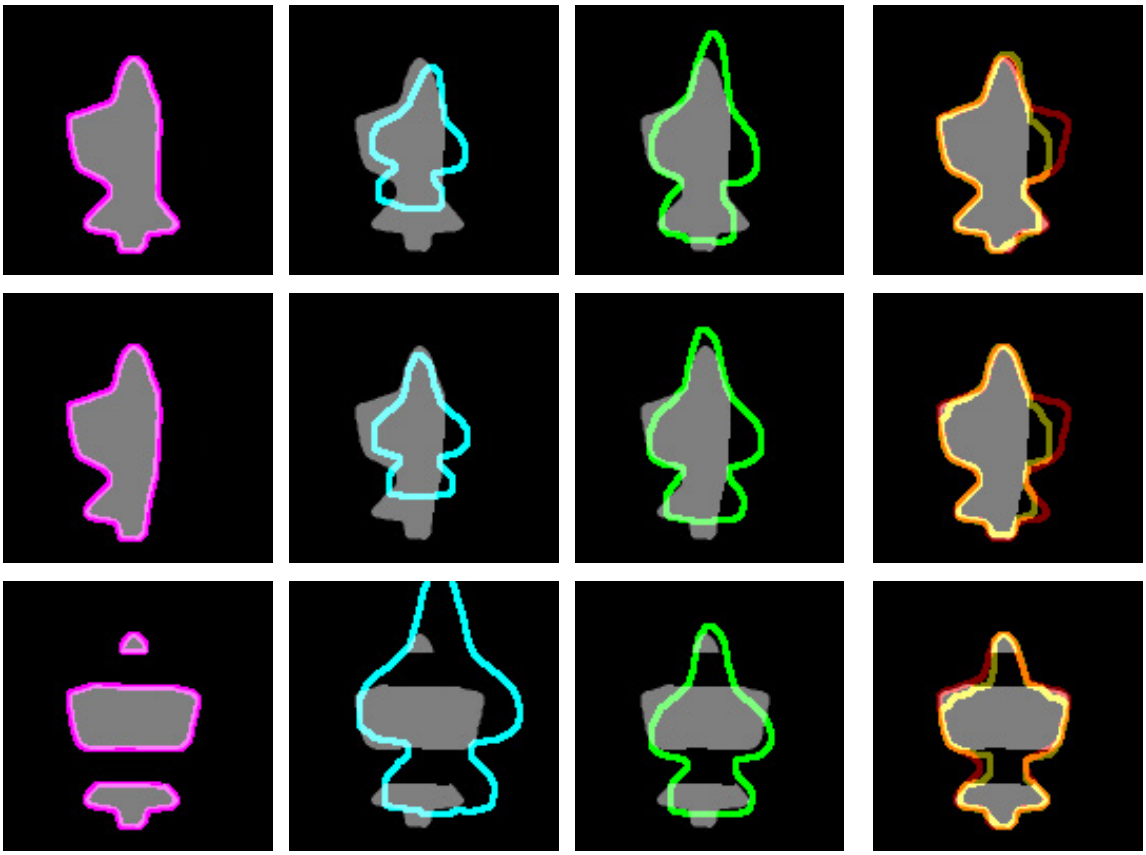

(a: Intensity) (b: Initialization) (c: 1st term of Eq. 37) (d: All terms of Eq. 37)

FIGURE 21 – Example 4: Segmentation results of a synthetic jet airplane images with different missing information and initializations. (a) The only intensity based segmentation results. (b) Different shape model initialization. (c) The results using only the first term of Eq. 37. (d) The segmentation of the proposed method (the red and yellow colors show the contour of the ground truth shape region, and the contour of the automatically segmented region, respectively).

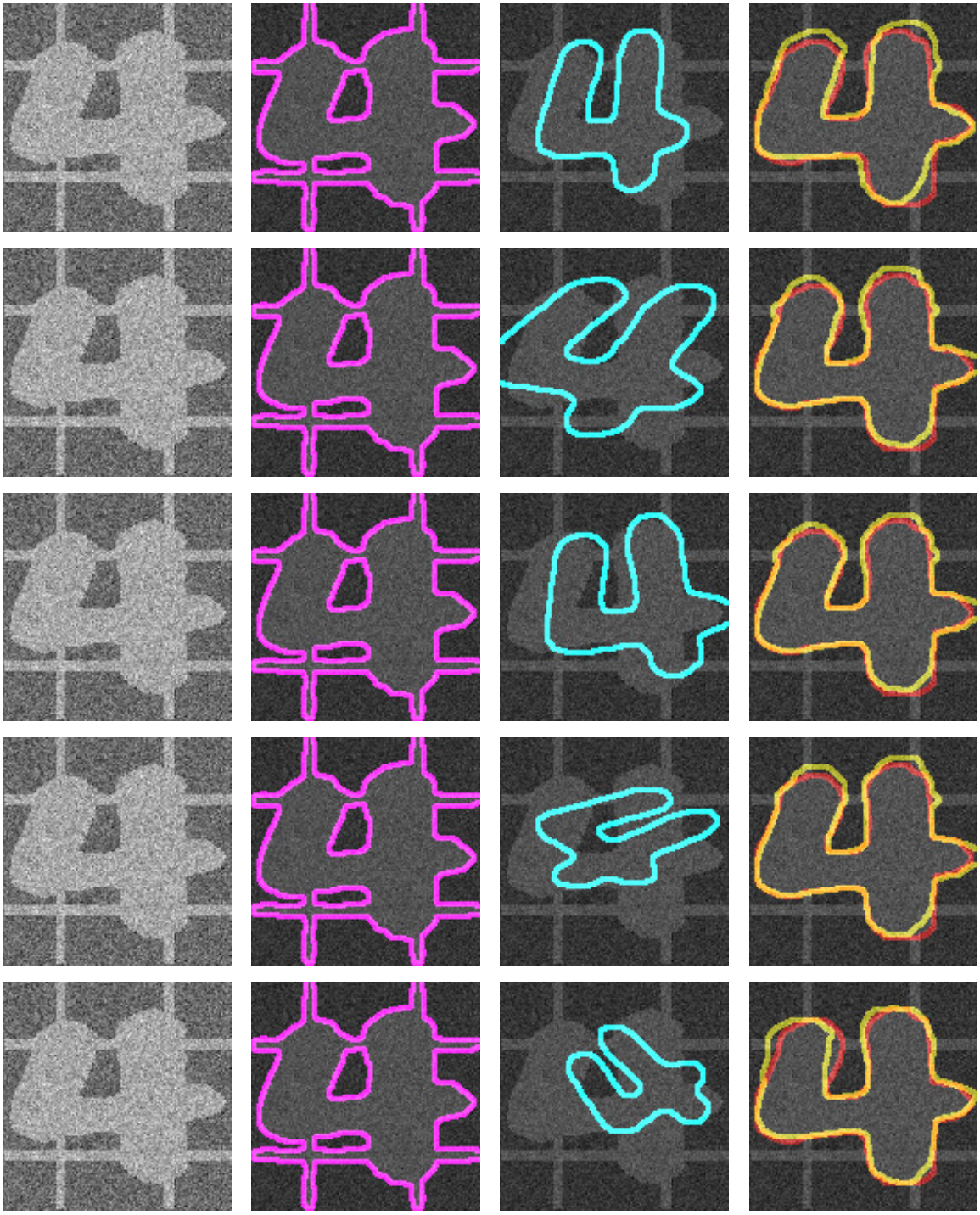

(a: Image) (a: Intensity) (b: Initialization) (d: Proposed)

FIGURE 22 – Example 5: (number ”4”): Segmentation results on a synthetic number ”4” with occlusions and different shape initializations. (a) The image with occlusions. (b) The segmentation results using only intensity information. (c) Different shape model initializations. (d-Proposed) The result of the proposed method (the red and yellow colors show the contour of the ground truth shape region, and the contour of the automatically segmented region, respectively).

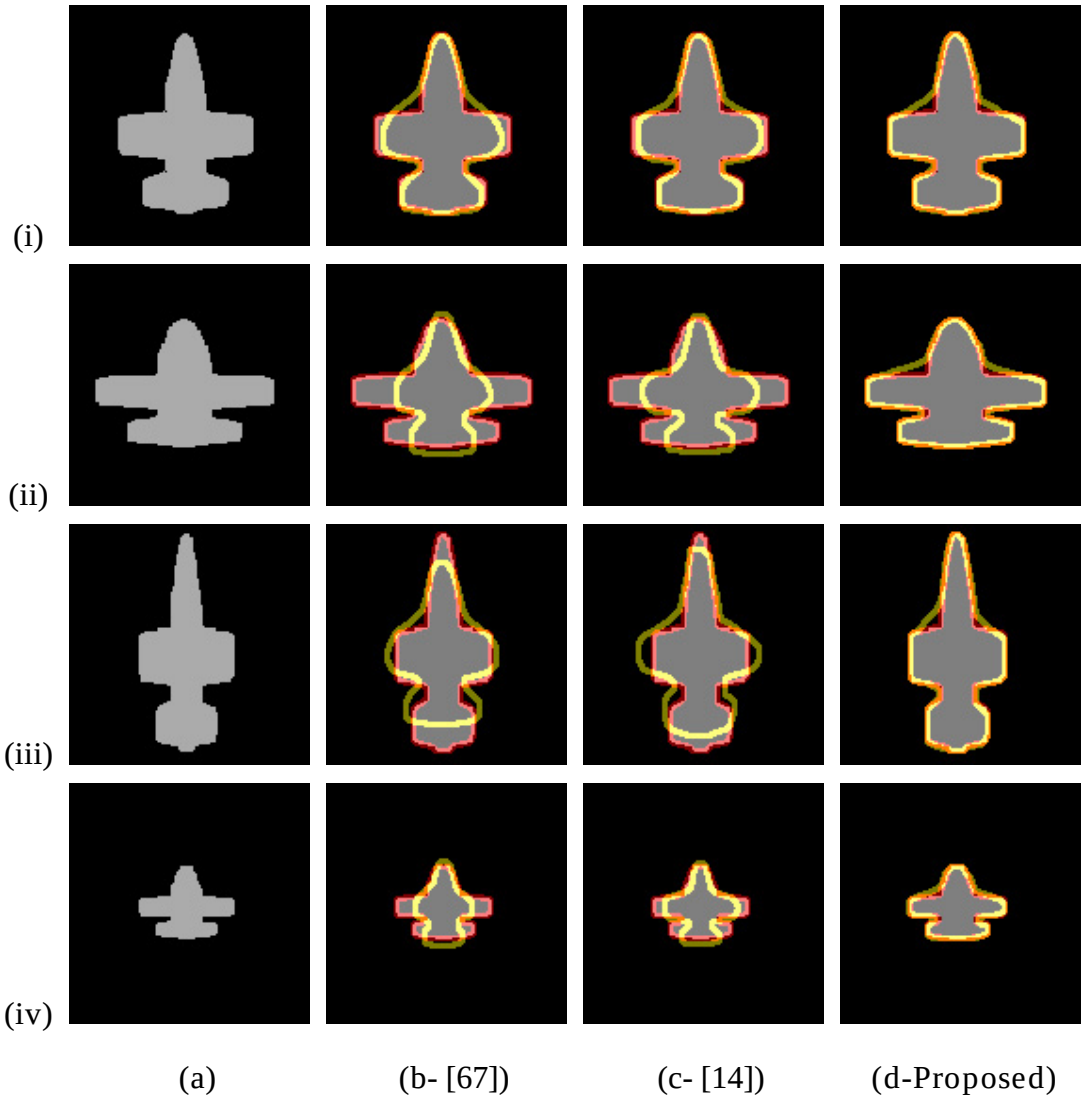

FIGURE 23 – Example comparison 1: Comparison with two closest works described in [14,67]. Testing shapes with (i) homogeneous and (ii-iv) inhomogeneous scaling factors. (i) $s_x = 1.0, s_y = 1.0$, (ii) $s_x = 0.7 s_y = 1.3$, (iii) $s_x = 1.2, s_y = 0.7$, (iv) $s_x = 0.4, s_y = 0.7$. (The red and yellow colors show the contour of the ground truth shape region, and the contour of the automatically segmented region, respectively).

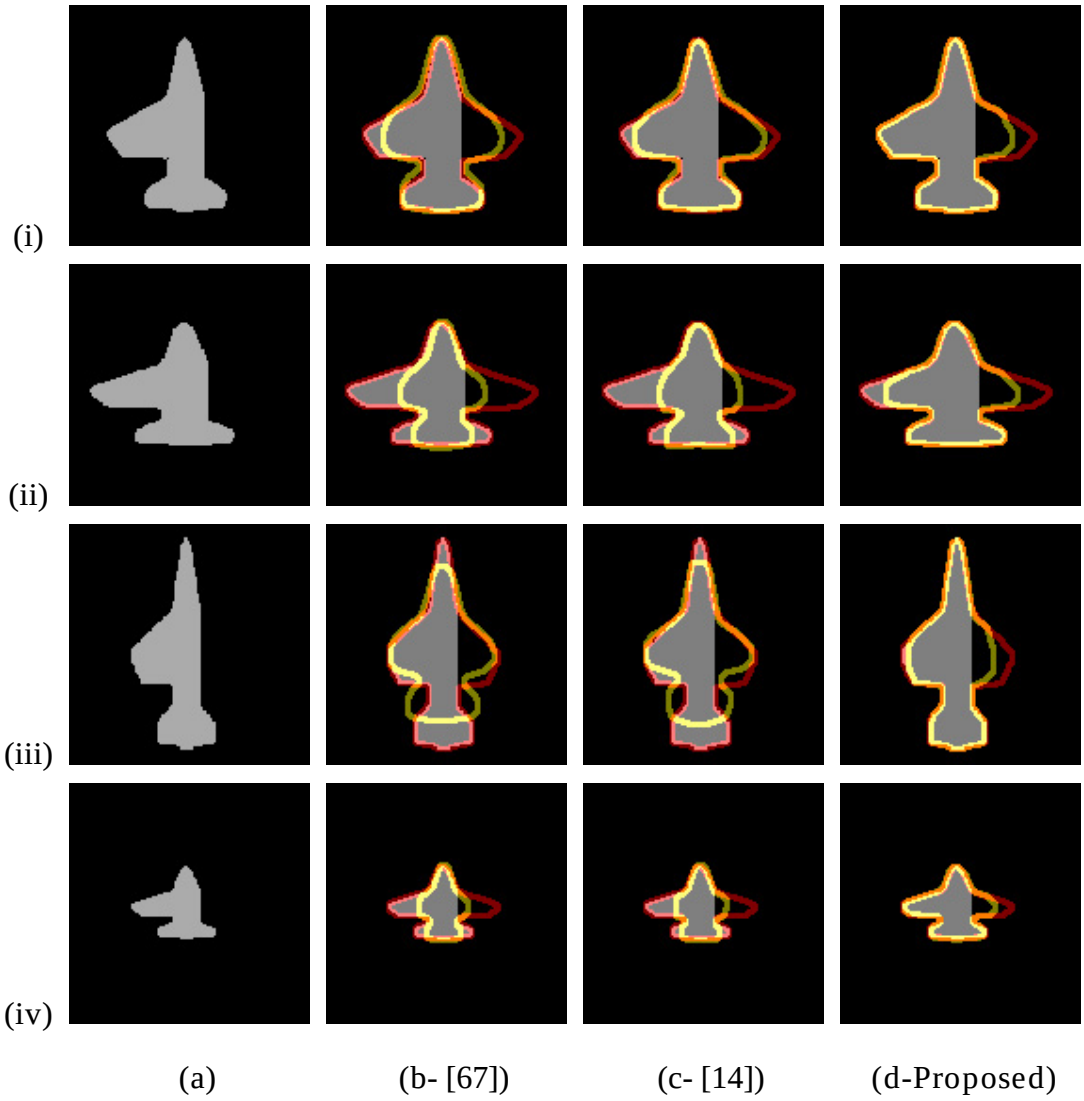

FIGURE 24 – Example comparison 2: Comparison with two closest works described in [14,67]. Testing shapes with (i) homogeneous and (ii-iv) inhomogeneous scaling factors. (i) $s_x = 1.0, s_y = 1.0$, (ii) $s_x = 0.7 s_y = 1.3$, (iii) $s_x = 1.2, s_y = 0.7$, (iv) $s_x = 0.4, s_y = 0.7$ (the red and yellow colors show the contour of the ground truth shape region, and the contour of the automatically segmented region, respectively).

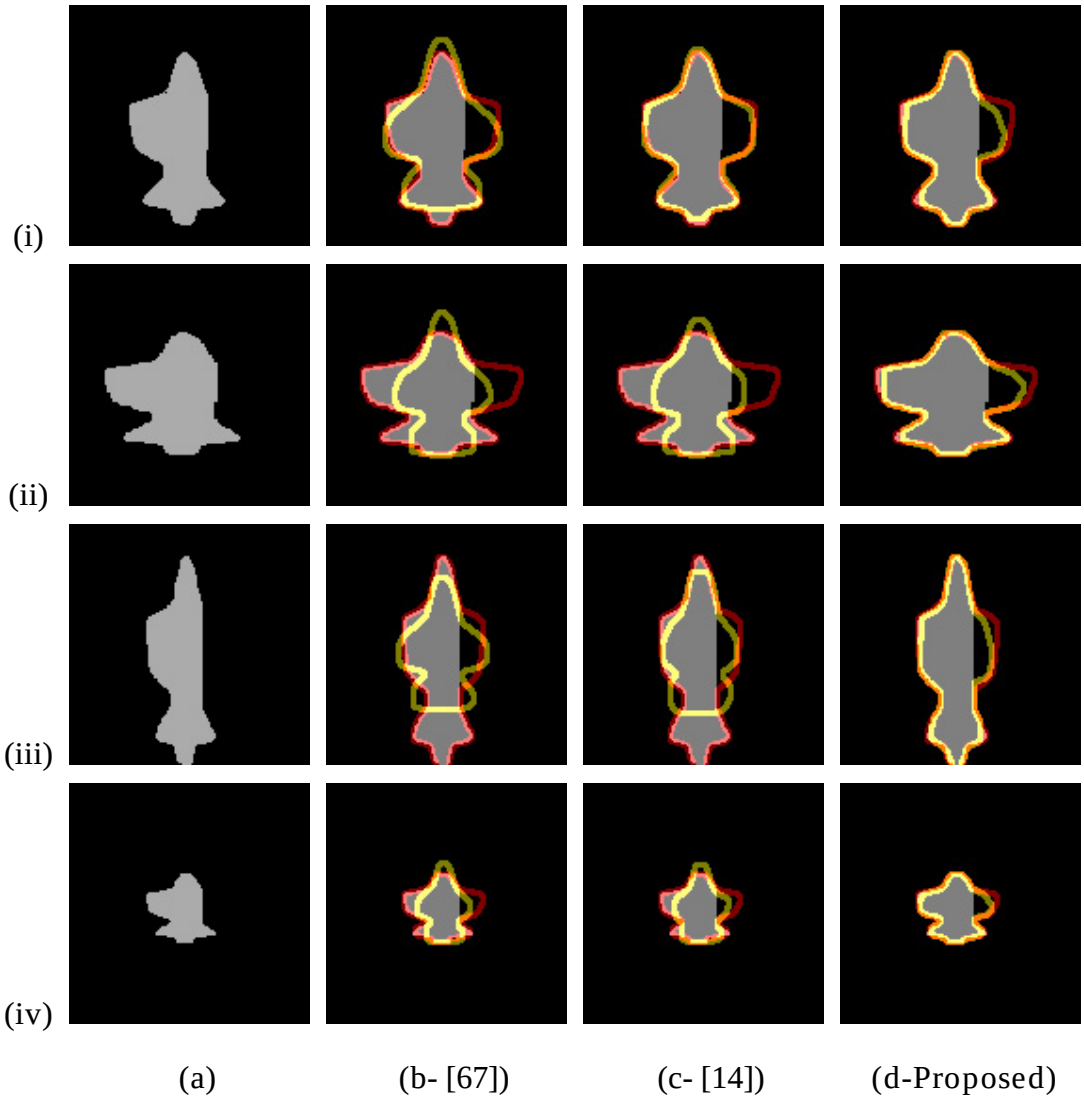

FIGURE 25 – Example comparison 3: Comparison with two closest works described in [14,67]. Testing shapes with (i) homogeneous and (ii-iv) inhomogeneous scaling factors. (i) $s_x = 1.0, s_y = 1.0$, (ii) $s_x = 0.7 s_y = 1.3$, (iii) $s_x = 1.2, s_y = 0.7$, (iv) $s_x = 0.4, s_y = 0.7$ (the red and yellow colors show the contour of the ground truth shape region, and the contour of the automatically segmented region, respectively).

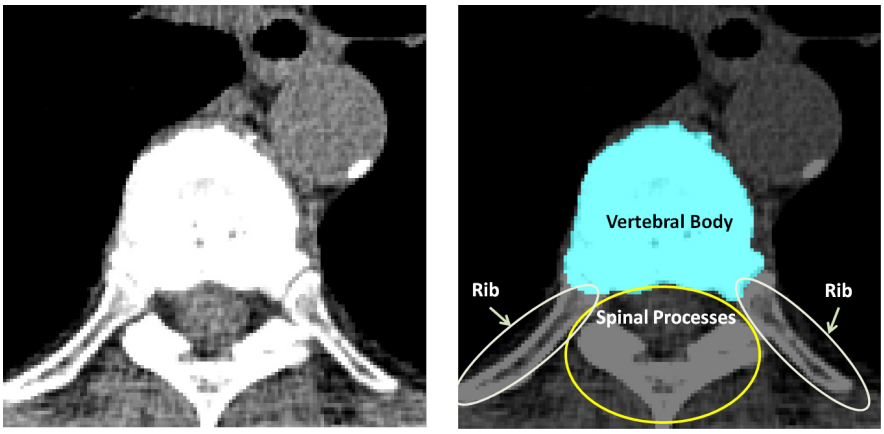

(a) (b)

FIGURE 26−(a) A vertebra in an axial CT. (b) Regions of the vertebra: The blue color shows the VB region which is the region of interest to be segmented. Spinal processes and ribs which should not be included in the BMD measurements are shown. As seen in the figure, the separation of the ribs and processes are not an easy task. This problem is solved by the proposed method.

the segmentation algorithms. To assess the proposed method under various challenges, a zero mean Gaussian noise with different variance σ_n^2 values (from 0 to 0.5) was added to the CT images.

To compare the proposed method with another alternative, VBs are subsequently segmented using the active appearance model (AAM) [9]. Segmentation accuracy is measured for each method using the ground truths (expert segmentation). To evaluate the results, the percentage segmentation accuracy (A) is calculated as follows:

$$A\% = \frac{100 * (number\ of\ correctly\ segmented\ pixels)}{Total\ number\ of\ \mathbf{VB}\ voxels}. \tag{40}$$

The proposed algorithm is tested on 12 ESP slices. The segmentation accuracy is shown in Table 1. The segmentation results on the ESP are shown in Fig 27. The results show that the proposed method is robust under various noise levels and segmentation challenges. In the next section, the algorithm is tested on clinical CT images to segment vertebral bodies.

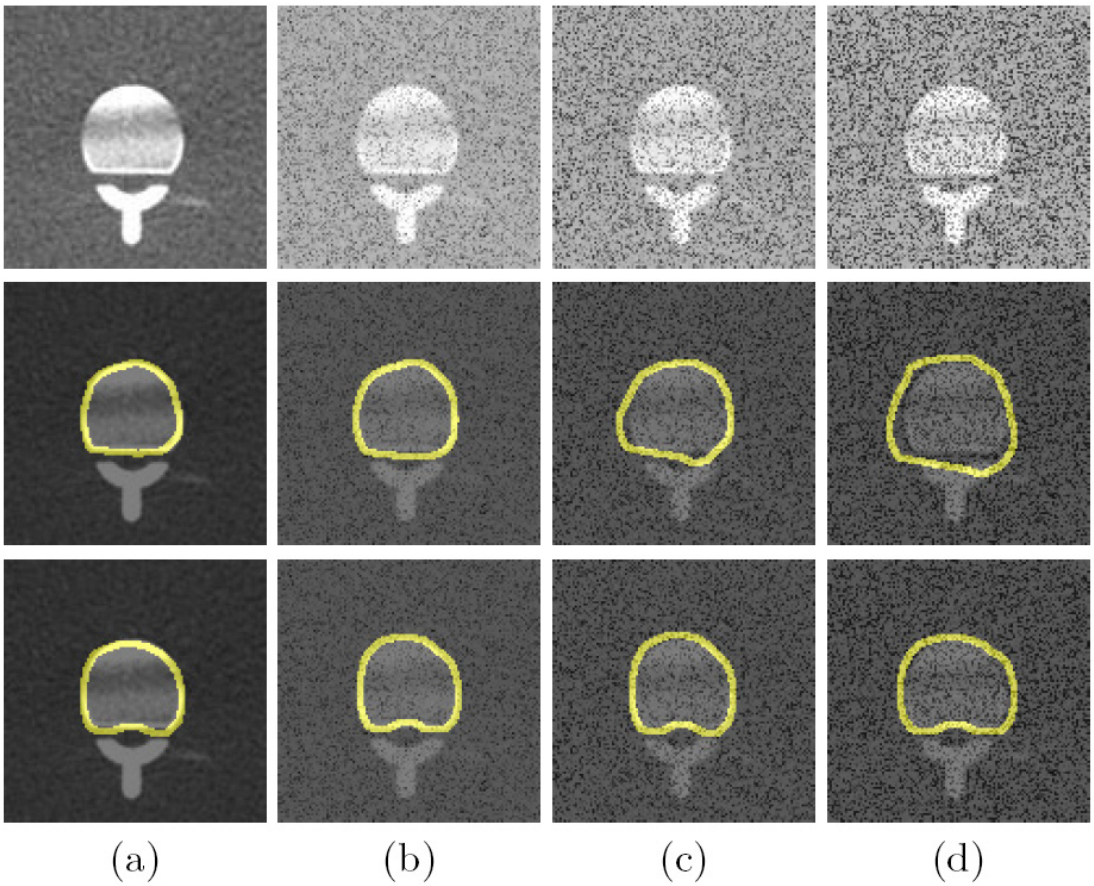

FIGURE 27 – Segmentation results of an ESP CT slice with (a) no noise, noise variances (b) σ_n^2=0.1, (c) σ_n^2=0.25, and (d) σ_n^2=0.5. The first row shows the original images. The second and third row show the results of the AAM and the proposed method, respectively. The yellow color shows the contour of the segmented region. As seen in the figure, the proposed method is robust under various noise levels.

TABLE 1
AVERAGE SEGMENTATION ACCURACY OF THE PROPOSED VB SEGMENTATION ON 252 CT IMAGES (INCLUDING 12 ESP IMAGES). THE SIZE OF EACH IMAGE IS 512X512 (AFTER EACH VB IS DETECTED, THE SIZE IS REDUCED TO 120X120).

	$\sigma_n^2 = 0$	$\sigma_n^2 = 0.1$	$\sigma_n^2 = 0.25$	$\sigma_n^2 = 0.5$	sec. / slice
Intensity based, %	72.4	69.5	65.2	59.2	5.6
AAM [9], %	87.2	86.5	83.1	81.4	7.2
Proposed, %	92.24	91.12	90.67	89.24	11.1

b. Experimental Results on VB The clinical data sets were scanned at 120kV and 2.5mm slice thickness. In this experiment, 240 testing CT slices (totals to 15 VBs) which are obtained from 13 different patients and different spine bone regions (i.e. lumbar, thoracic, and etc.) are tested. The objective is to segment the VB region correctly.

First, the results on shape registration with different initialization are shown. Figures 28-30 show the segmentation results of the proposed framework with different scaling, translation, and rotation initializations. Using the shape model, the spinal processes are eliminated automatically without any computational cost and execution time. This contribution is very important for the BMD measurements which are restricted to the VBs.

Figure 31 shows the segmentation results of the proposed and AAM methods with different shape model initialization. This test proves that the proposed method is robust under different shape initialization. AAM results show that when the shape model is initialized close enough to the object, the results are acceptable. However, when the shape model is initialized slightly far away from the object, the AAM method fails to capture the object of interest. Also, 3D results of segmentation results are shown in Figure 32.

F. Conclusion

A new shape based segmentation method is proposed by minimizing new dissimilarity measures using the dynamic and probabilistic shape model. Two energy terms are proposed to be minimized: i) intensity and ii) shape terms. The contribution is mainly on the second energy term. The algorithm is tested on synthetic images, the ESP with various noise levels, and clinical CT images. The method is validated with different shape initialization parameters, target shapes/images with occlusions or missing information, and noise. The effects of each term in the dissimilarity measure are analyzed. Experiments on the data sets show that the

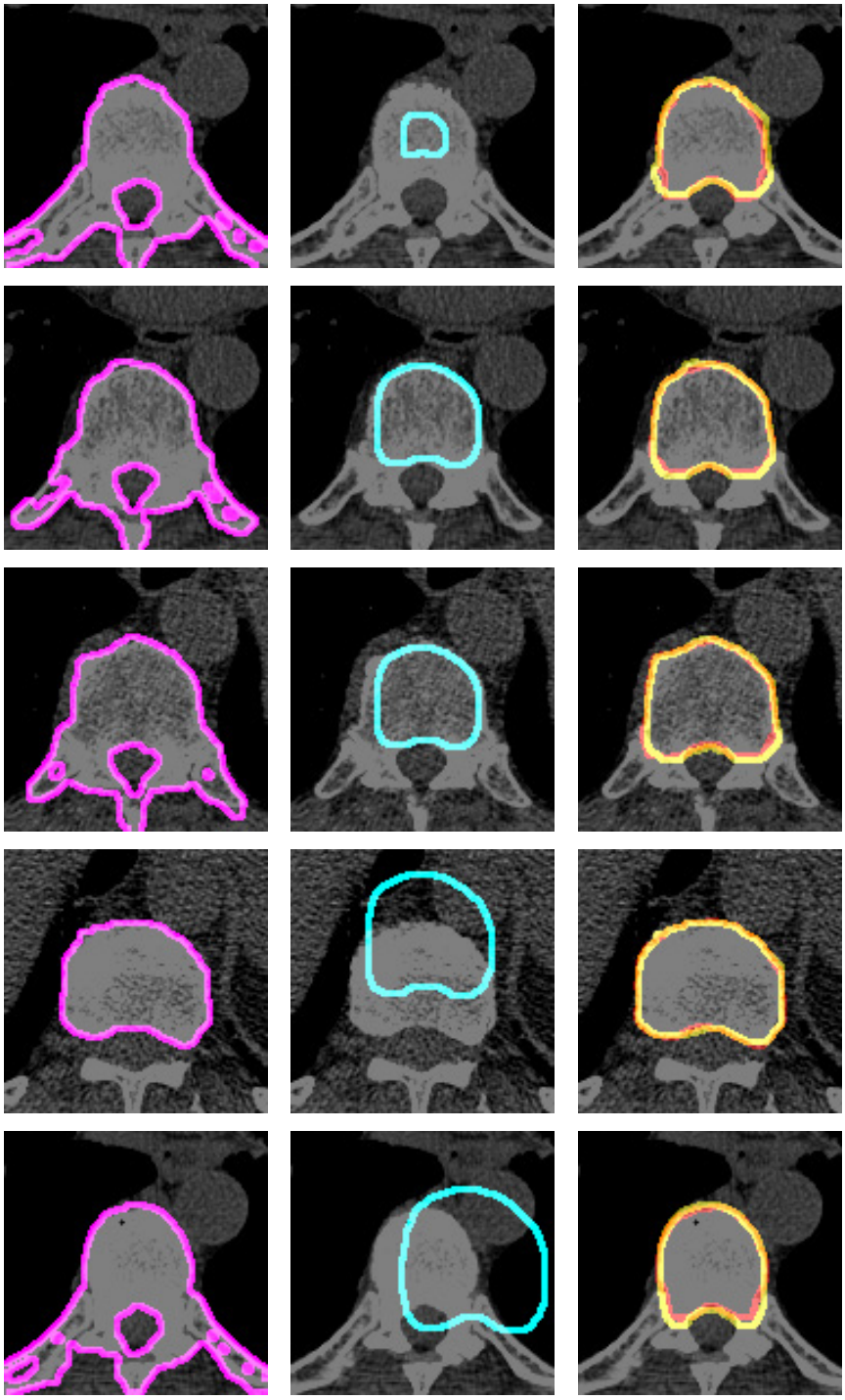

(a) (b) (c)

FIGURE 28 – Segmentation results of clinical CT images. (a) Only intensity based segmentation results. (b) Different initialization of the shape model. (c) The proposed segmentation results (the red color shows the contour of the ground truth shape region, the yellow color shows the contour of the automatically segmented region).

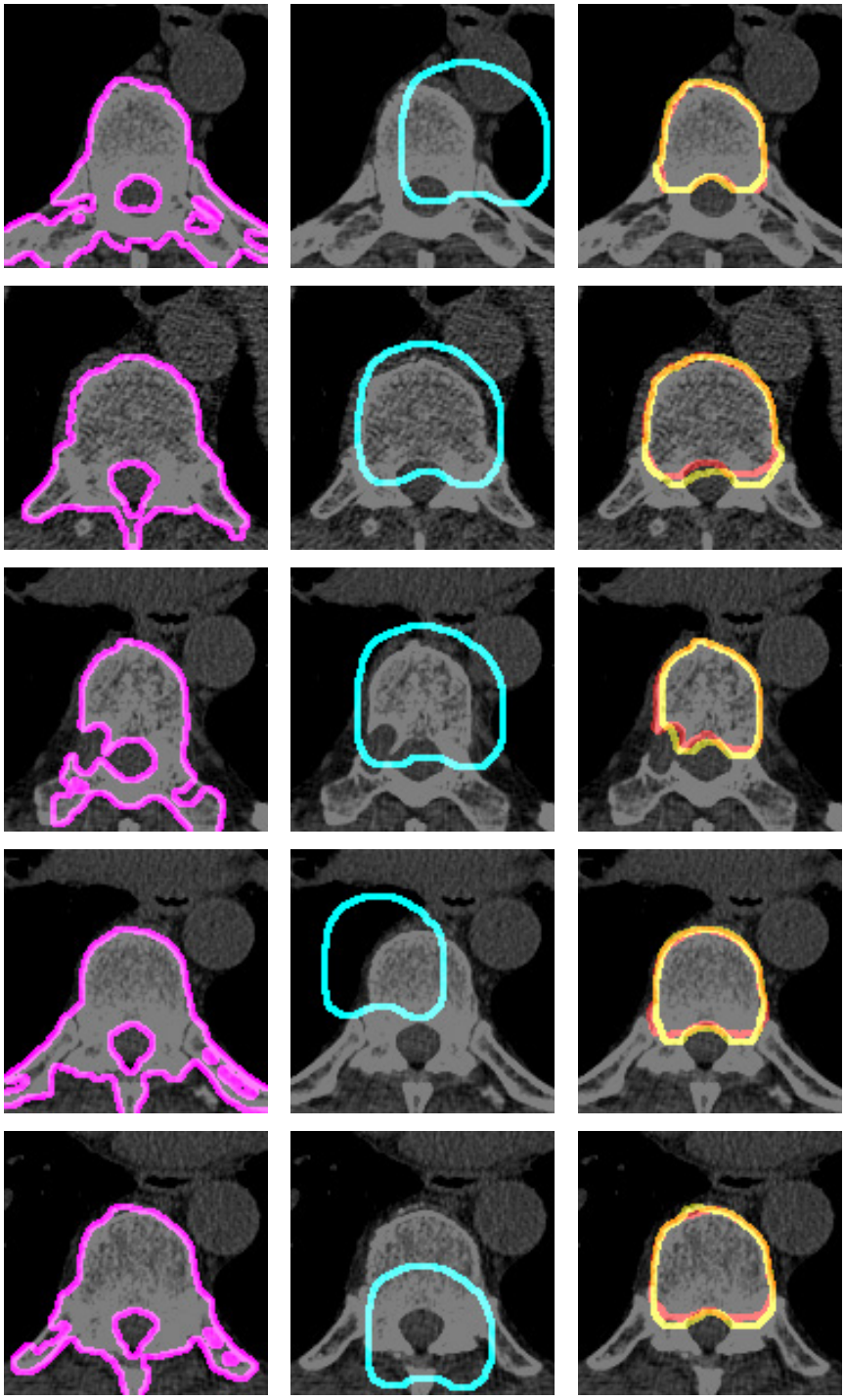

(a) (b) (c)

FIGURE 29 – Segmentation results of clinical CT images. (a) Only intensity based segmentation results. (b) Different initialization of the shape model. (c) The proposed segmentation results (the red color shows the contour of the ground truth shape region, the yellow color shows the contour of the automatically segmented region).

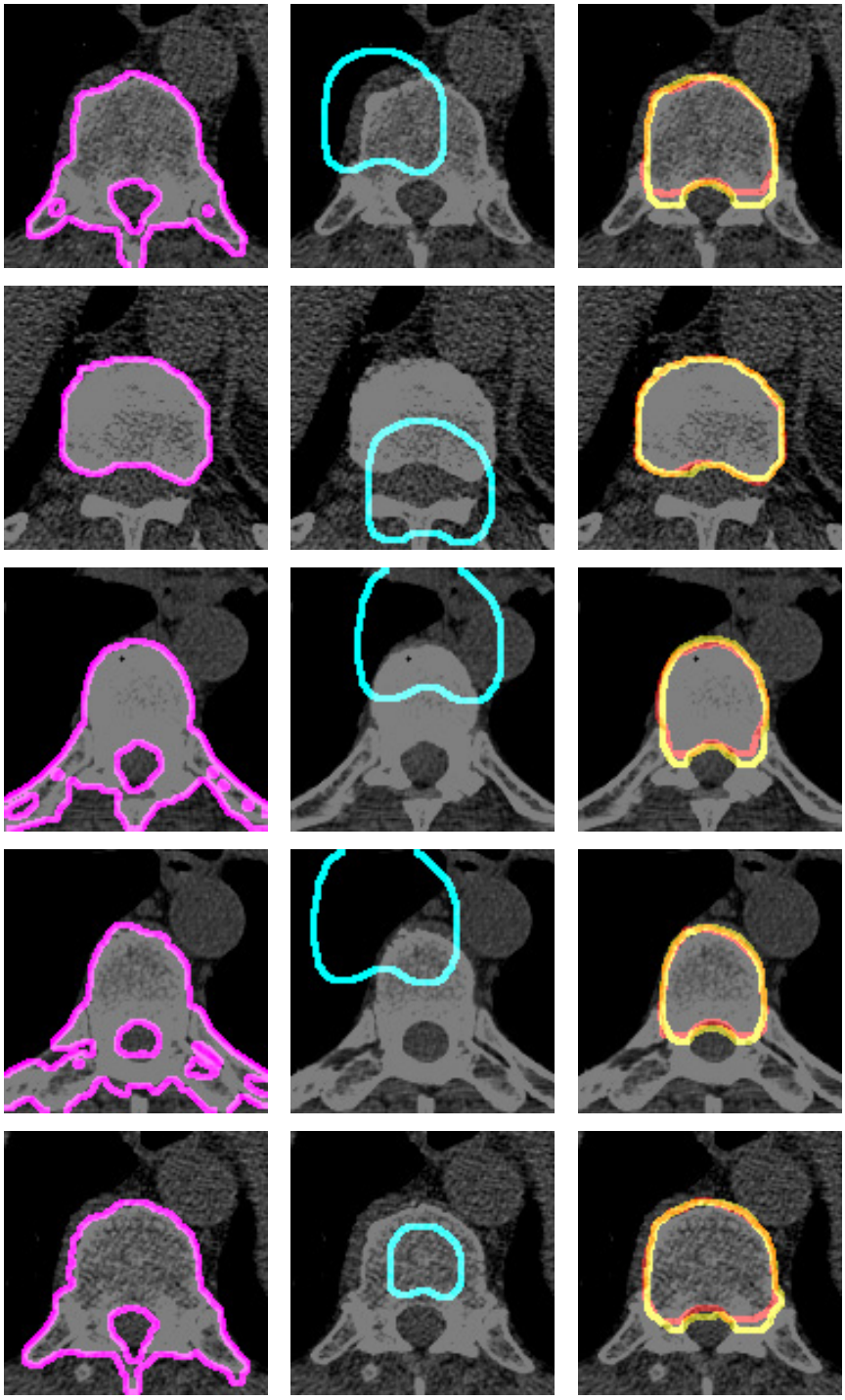

(a) (b) (c)

FIGURE 30 – Segmentation results of clinical CT images. (a) Only intensity based segmentation results. (b) Different initialization of the shape model. (c) The proposed segmentation results (the red color shows the contour of the ground truth shape region, the yellow color shows the contour of the automatically segmented region).

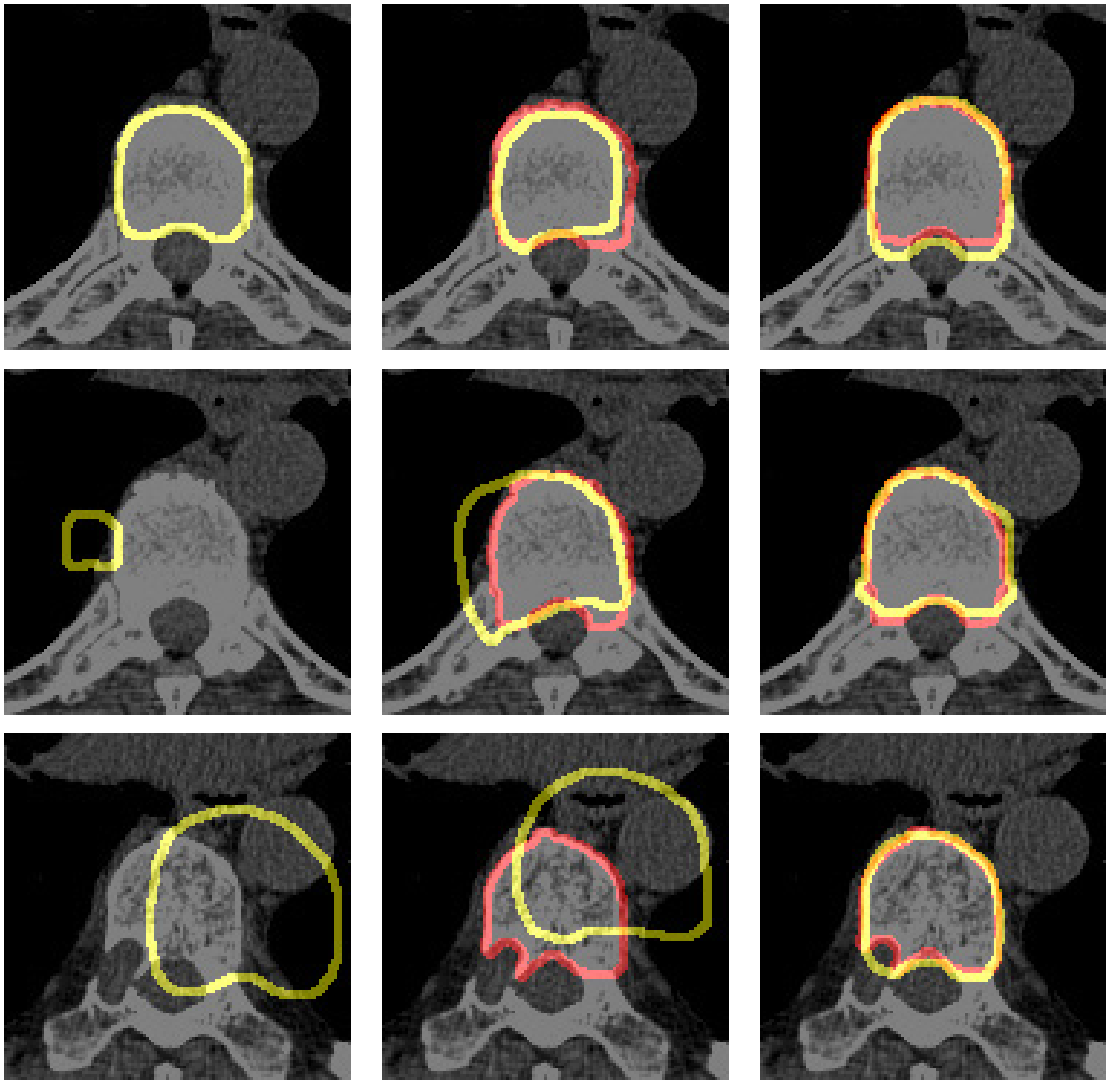

(a-Initialization) (b- [9]) (c-Proposed)

FIGURE 31 – Segmentation results on the clinical VB images with various shape initializations. In this figure, i) shows the shape initialization, ii) the results of AAM [9] when the shape model is initialized at the same location as shown in (i), and iii) shows the proposed segmentation results. (The red and yellow colors show the contour of the ground truth of objects and the contour of the segmented region, respectively.)

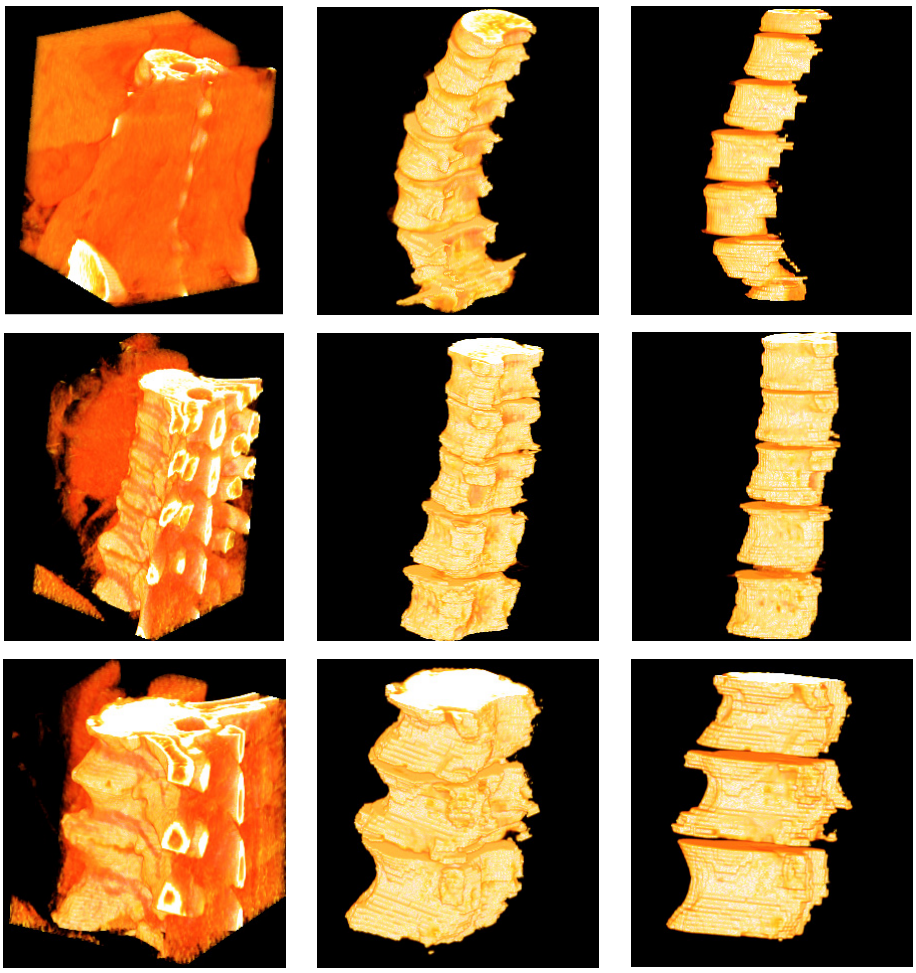

(a) (b) (c)

FIGURE 32 – 3D result of the segmentation results. (a) 3D CT data before the segmentation. (b)-(c) The segmentation results on different views. As seen in the figure, the proposed method is able to extract the spinal processes, ribs, and other surrounding soft tissues. It should be noted that adjacent VBs are assumed to be separated in advance.

proposed segmentation approach is very accurate and robust under different image conditions. Also, the proposed framework is able to improve the global shape registration results. Using the shape prior, the proposed method is able to extract the spinal processes.

CHAPTER III

STATISTICAL SHAPE BASED SEGMENTATION OF VERTEBRAL BODIES

This chapter describes the proposed method to solve existing drawbacks on spinal bone segmentation publications.

A. Spinal Bone Anatomy and Osteoporosis

1. Anatomy of the Spine Column

There are five sections of the spinal column including the cervical (7 VBs), thoracic (12 VBs), lumbar (5 VBs), sacral (5 VBs), and coccyx (3-5 fused VBs) as shown in Figure 33. The VB consists of cortical and trabecular regions. Cortical and trabecular bones form 70-80% and 20-30% of bone mass, respectively. Approximately 25% of the trabecular bone volume is bone tissue and 75% is bone marrow and fat. This proportion changes between different parts of the skeleton. Bone marrow has stroma, myeloid tissue, fat cells, blood vessels, sinusoids and some lymphatic tissue. The ratio between bone tissue and bone marrow also decreases with osteoporosis [69].

2. What is osteoporosis?

Osteoporosis is a bone disease characterized by a reduction in bone mass, resulting in an increased risk of fractures [69]. Figures 34 and 35 show some example views of healthy, osteopenia, and osteoporosis bones. With osteoporosis, a subject's bone tissue has less than the normal proportion amount of calcium. The

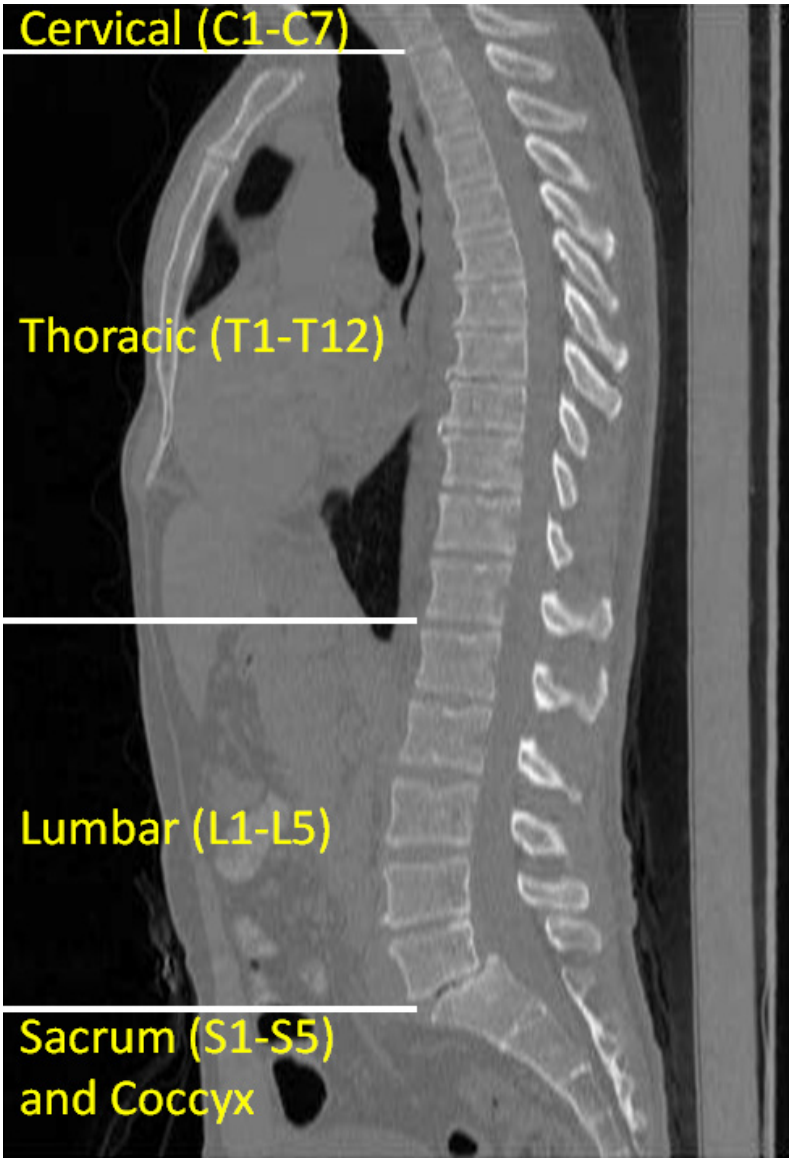

FIGURE 33 – The sagittal view of the spine column. There are five regions of the spine column: cervical, thoracic, lumbar, sacrum, and coccyx.

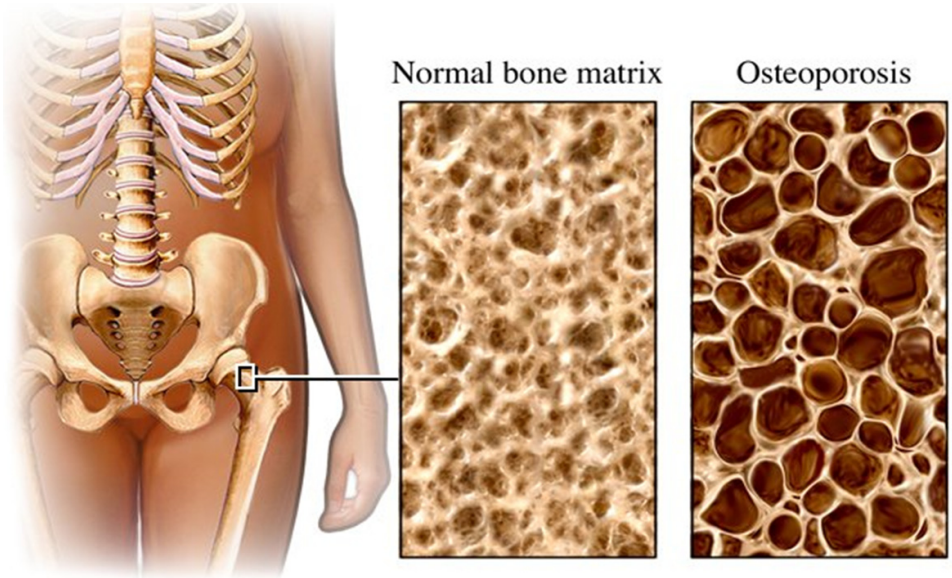

FIGURE 34 – Differences of the healthy and osteoporosis bone. (This image is adopted from [72].)

additional space is filled with fat. The ratio between the bone tissue and bone marrow is decreasing [69]. Low bone mass and osteoporosis occur more frequently in women. The bone begins loosing its weight and calcium soon after menopause. Without diagnosis and prevention, a woman can lose 20%-30% of her bone mass during the first 10 years of menopause [70].

Based on the Surgeon General report [71], there were approximately 10 million people over age 50 with osteoporosis and an additional 34 million with low bone mass or osteopenia in the United States in 2002. Unfortunately, the total number is expected to be increased to 61.4 million in 2020 as shown in Fig 36. These changes could cause the number of vertebrae, hip, and wrest fractures to increase rapidly by 2040 [71]. Example view of fractures is shown in Fig 37. It should be noted that 50% from all osteoporotic fractures are vertebral [37].

Some of the reasons of low bone mass and osteoporosis are poor nutrition, lack of exercise, decreased sex hormones, calcium and vitamin D deficiency, loss of ability to reproduce bone cell with age, other diseases and disorders.

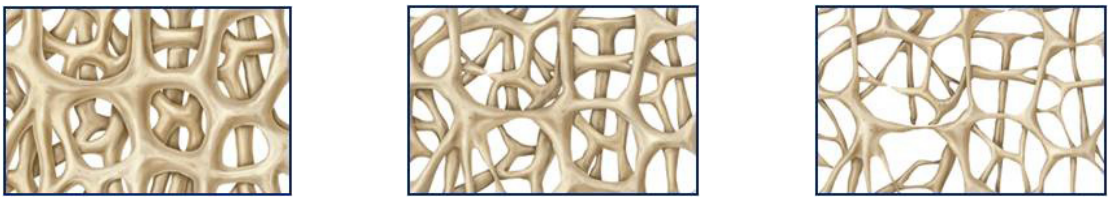

(a) (b) (c)

FIGURE 35 – Three different bone tissues. (a) Healthy, (b) osteopenia, and (c) osteoporosis bones. (These images are adopted from [73].)

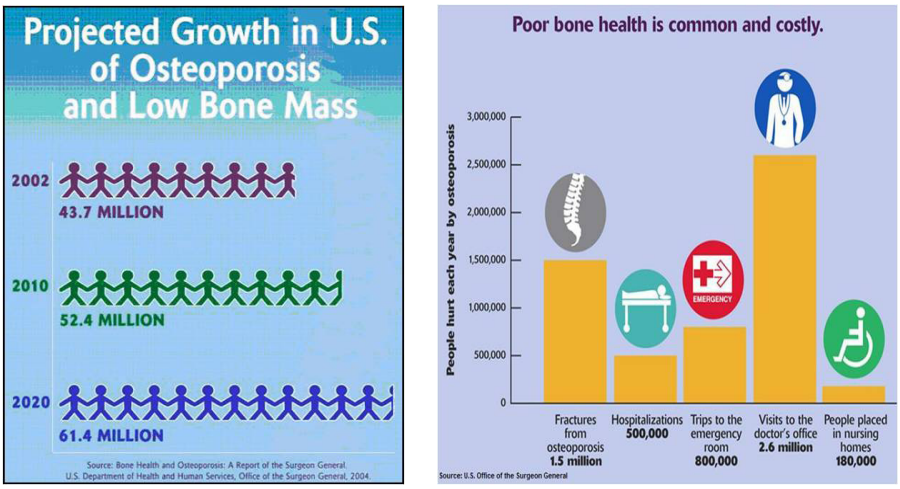

(a) (b)

FIGURE 36 – Based on the Surgeon general report (a) shows the current and estimated the number of people having low bone mass in 2002, 2010, and 2020, and (b) shows several consequences of having low bone mass. (These images are adopted from [74]).

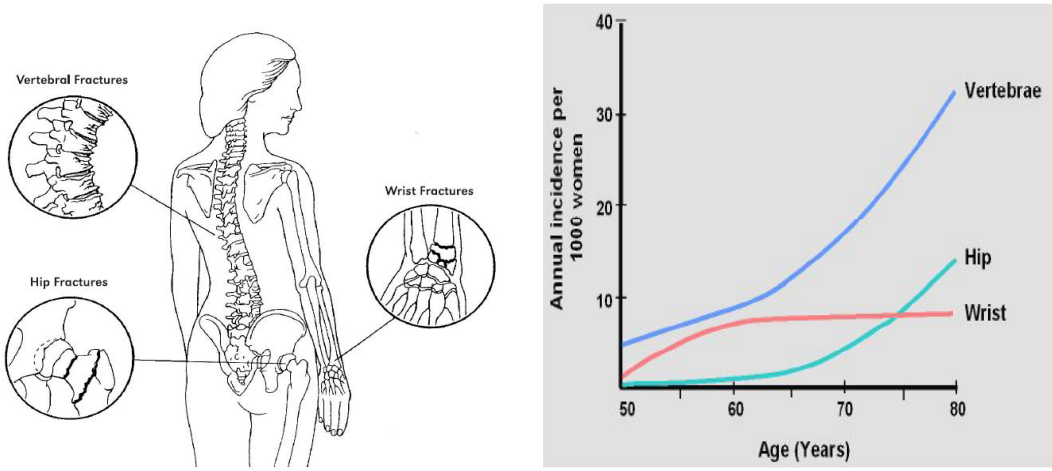

(a) (b)

FIGURE 37 – (a) Low bone mass (osteopenia) and osteoporosis cause severe fractures on vertebrae, hip, and wrist. (b) With increasing age, the incident of vertebral fractures are higher than the incidents of hip and wrist. (These images are adopted from [74] and [75], respectively).

3. How to Diagnose Osteoporosis

Doctors need the bone mineral density (BMD) measurements of vertebral bones in order to diagnose and treat osteoporosis. The BMD measurements remain the 'gold standard' test for an osteoporosis diagnosis. The BMD measurements are strong predictors of fracture risk. In the Surgeon General report, it is strongly stated that the relationship between the BMD score and future fracture is stronger than the relationship between cholesterol and heart attack [71]. The BMD measurements are also used to assess bone changes in treated and untreated individuals for monitoring drug therapies.

B. Introduction

Osteoporosis is a bone disease characterized by a reduction in bone mass, resulting in an increased risk of fractures. Doctors need the BMD measurements of vertebral bodies (VBs) in order to diagnose and treat osteoporosis. The verte-

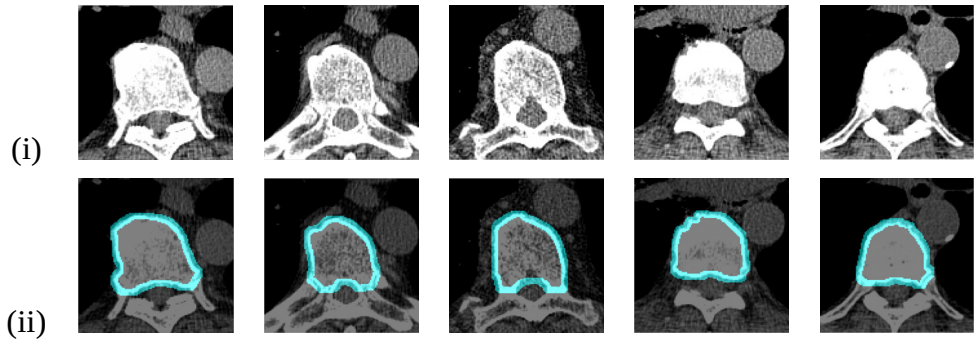

FIGURE 38 – More examples for the VB region definition. i) The original CT images show different vertebrae. ii) The blue contour shows vertebral body which is the region of interest. VBs are required to be separated from the ribs and spinal processes which have similar gray level information.

bra of the spine bone consists of the vertebral body, spinous process, transverse processes, articular processes, lamina, pedicles, and ribs. The VB region of interest examples are shown in Figure 38. Spinous process, transverse processes, articular processes, lamina, pedicles, and ribs should not be included in the BMD measurements since the BMD measurements are restricted to the VBs. As seen in the images, the VB segmentation is not an easy task since the ribs and processes have similar gray level information. The general objective is to segment the VBs correctly and increase the accuracy of the BMD measurements and fracture analysis. In this study volumetric computed tomography (CT) images of the VBs are used in the experiments.

Segmentation is an important method for feature extraction, image measurements, image registration, and image display. Segmentation has been used in many applications such as surgery simulations, measuring tumor volume, automated classification of blood cells, studying brain development. There have been many important segmentation works which should be reviewed. However, the revision of the different segmentation methods will not be reviewed since the aim of this work is to focus on the VB segmentation. In this section, the most important published works on spine bone segmentation are reviewed. The advantages and disadvantages of the existing methods are discussed.

There are limited publications on spine bone segmentation and analysis. The previously reported methods can be categorized as

- fully automatic,
- semi-automatic (with manual interactions),

Semi-automatic algorithms may have manual interactions. With manual interactions, user(s) have been able to detect, identify, and sometimes segment the adjacent VBs and spinal cord. There are few fully automatic methods in the scientific literature. These are theoretically correct and useful. However, they take high computational cost or execution time.

For instance, Kang et al. [76] proposed a 3D segmentation method for skeletal structures from CT data. Their method is a multi-step method that starts with a three dimensional region growing step using local adaptive thresholds, followed by a closing of boundary discontinuities and then an anatomically-oriented boundary adjustment. Applications of this method to various anatomical bony structures were presented and the segmentation accuracy was determined using the European Spine Phantom (ESP) [68].

Mastmeyer et al. [51] presented a hierarchical segmentation approach only for the lumbar spine in order to measure the bone mineral density. The detection vertebrae is carried out manually. The adjacent VBs are separated using a histogram information. Then, a two step segmentation using a deformable mesh followed by adaptive volume growing operations are employed in the segmentation. After the segmentation of the vertebra, the spinal processes are eliminated using morphological operations. The authors conducted a performance analysis using two phantoms: a digital phantom based on an expert manual segmentation and the ESP. The authors reported that complete analysis of three vertebrae took approximately 10 minutes in 2006 on a high standard computer system. This timing is far from the real time required for clinical applications but it is a huge improvement compared to the timing of $1 - 2h$ reported in [54].

Klinder et al. [36] proposed an automatic solution for detecting, identifying,

and segmenting vertebrae in CT images. They used a prior knowledge through the use of various kinds of models covering shape, gradient, and appearance information. Their method was designed to take an arbitrary CT image such as head-neck, thorax, lumbar, or whole spine as input. The major contribution of this work is the automated vertebrae identification. Their vertebrae identification rate was approximately 70% on 64 CT data sets. The shapes of neighboring vertebrae are generally very similar. Therefore an automatic identification is generally difficult to obtain. In the identification step, appearance models are rigidly registered to the detected candidates. This step is carried out for all testing vertebrae and the similarity measure is evaluated. The average similarity value is calculated to avoid mis-detection of vertebrae. Finally, triangulated shape models of the individual vertebra are adapted. Although, their method is comprehensive and yields an overall final mean error of 1.12 mm, the framework may not be used in clinical works as the authors stated. The authors reported that the execution time for 12 vertebrae identification was 2192 seconds (36.5 min) on average. Also, in this study the VB and processes were not separated. As mentioned above, the spinal processes should not be included in the BMD measurement.

Kim et al. [77] proposed an automatic vertebra segmentation in CT data. 3D fences that separate adjacent vertebrae are used. The method extracts the spinal cord and discs automatically. 3D fences separating adjacent vertebrae are generated at each intervertebral disc by a deformable model using 3D valley information. The final segmentation is obtained using a seed region growing method. In this work, the average execution time to segment a vertebra was not reported.

Yao et al. [52] proposed another segmentation method using the watershed algorithm. In this method they initially locate and extract the spine region using a simple threshold. Then the watershed algorithm is used to extract the spinal cord. Multiple spinal cord (canal) candidates may exist in one slice. They proposed a directed graph search to find the spinal cord. Finally, a four-part vertebra model is applied to segment the vertebral body. The model consists of the vertebral body,

spinous process, and left and right transverse process. Also, in this study there was no work to separate the VB and spinal processes. Other techniques have been developed to segment bone structures and can be found for instance in [78, 79] and the references therein.

Aslan et al. proposed various methods to segment VBs in [27, 34, 80, 81] which can be considered as progressive VB segmentation studies. In [27], the shape model was not used and it was assumed that the detection rate of VBs was very accurate for cropping the pedicles automatically. In [80], a probabilistic shape model was introduced in addition to the intensity and spatial interaction information to enhance the results. However, the shape model was assumed to be registered to the object of interest manually. In [34, 81], the probabilistic shape model was automatically embedded into the image domain and they appeared to be more realistic experiments. In [34], the shape model was registered into the image domain using the gradient descent approach which requires very high execution time, and hence is not suitable in clinical cases. In this dissertation, the automatic shape registration method described in [81] which is faster than the gradient descent methods, is used. However, the level sets method in [81] needs manual initialization and was validated on a limited number of data sets. Other techniques have been developed to segment bone structures and can be found for instance in [78, 79] and the references therein.

There are difficult segmentation challenges in spine CT images as shown in Figures 39-40. These include inner boundaries, osteophytes, bone degenerative disease, double boundary, and weak edges of spine bones. Also, exposure levels (X-ray tube amperage and peak kilovoltage), slice thickness, and volume of interest (VOI) affect the resolution of CT images. Higher exposure levels, bigger VOI, and smaller slice thickness produce a higher signal-to-noise ratio (SNR) as shown in Figure 41 (a). However, optimum parameters of image modalities may not be used in order to limit the radiation dose which is applied to a patient as shown in Figure 41 (b). As a result, segmentation methods should be robust to various

image conditions. To overcome these problems, the volume gray level information, spatial relationships of voxels, and shape prior information are used in this work.

In some CT images the separation of VBs is very difficult and algorithms may not be robust on images with high slice thickness and / or noise levels and / or bone degeneration diseases. The objective of this project is to obtain an algorithm which user(s) may select manual points in the VB separation stage only if the automated process fails. Otherwise, the process is entirely automated. In this study, the dependency on the automatic VB identification step in [36] which requires the registration of model shapes which were constructed for each spinal bone region (i.e. lumbar, thoracic, and etc.), and therefore the identification step costs huge execution time is not required.

In this dissertation, the objective is to eliminate the aforementioned problems as follows: i) The shape model is embedded into the image domain automatically (without any user interaction) and is faster than gradient descent methods, ii) the proposed method is validated using a higher number of data sets, iii) the proposed shape model is a universal shape information which works for any area of the spinal region such as thoracic, lumbar and etc. Hence, the proposed method does not need the VB identification process which requires very high execution time as in [36]. iv) the large execution time for the vertebra segmentation is reduced when compared with existing methods.

To overcome these problems, the volume gray level information, spatial relationships of voxels, and shape prior information are used in this dissertation. The objective is to eliminate the above problems as follows: i) The shape model is embedded into the image domain automatically (without any user interaction) and the registration is faster than gradient descent methods, ii) the proposed method is validated using a higher number of data sets respect to [34, 81], iii) the proposed shape model is a universal shape information which works for any area of the spinal region such as thoracic, lumbar and etc. Hence, the proposed method, in this dissertation, does not need the VB identification process which requires very

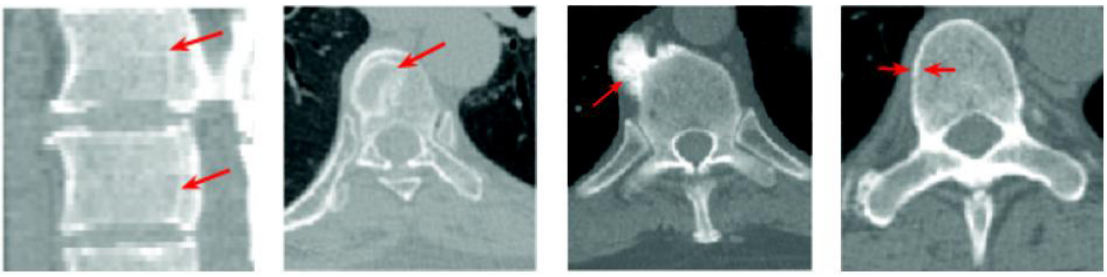

(a) (b) (c) (d)

FIGURE 39 – Typical challenges for vertebrae segmentation. (a) Inner boundaries. (b) Osteophytes. (c) Bone degenerative disease. (d) Double boundary.

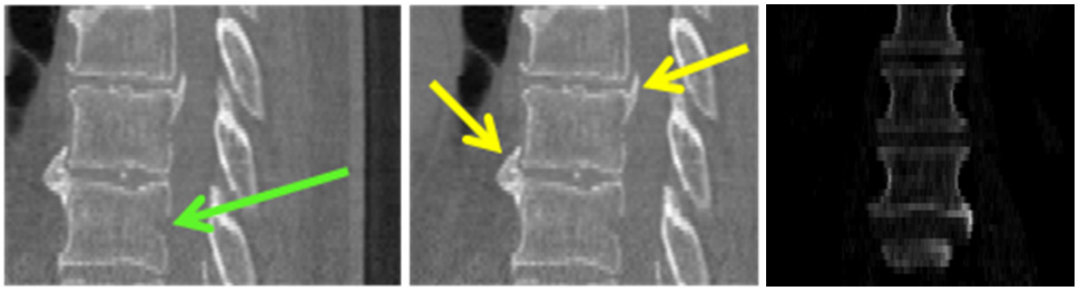

FIGURE 40 – More challenges on sagittal and coronal axes such as weak bone edges, osteophytes, and low resolution (from the left column to the right column, respectively).

high execution time. iv) Direct comparison with other methods would be difficult since previous works and this work have common and different objectives as a brief and relative comparison will be given on the experimental section. It should be noted that the computer systems reported on related publications are older than computer system specification in this work. However, the proposed framework completes the VB segmentation in very low execution time when compared with reports on the existing methods. vi) In some CT images the separation of VBs is very difficult and algorithms may not be robust on images with high slice thickness and / or noise levels and / or bone degeneration diseases. The objective of this work is to obtain an algorithm which user(s) may select manual points only in the VB separation stage.

(a)

(b)

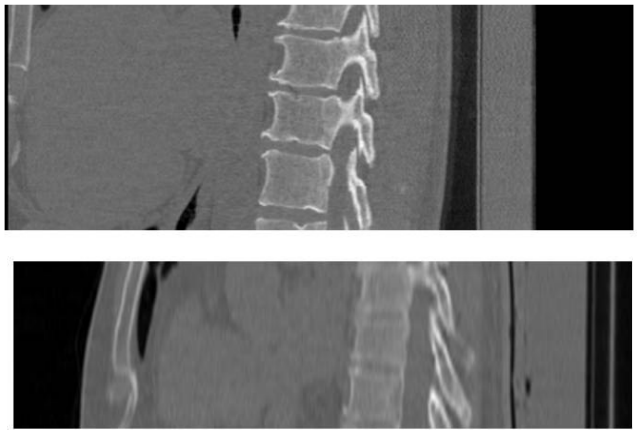

FIGURE 41 – Two different CT data sets. (a) The resolution is good, hence separation and segmentation of a VB is straightforward. (b) The resolution is low which makes the separation and segmentation of a VB difficult.

C. Motivation

The objective of this chapter is to propose a framework which has the following features:

- Original: To solve the VB segmentation problem with a new shape based segmentation method.
- Robust: The proposed method works under various segmentation challenges.
- Fast: The proposed algorithm can be used in clinical applications where quick results are necessary.

D. Contribution of this Study

The contributions can be listed as follows:

- The proposed framework and the new probabilistic shape model extract the spinal processes and ribs which should not be included in the bone mineral density measurements. In other works, such as [51], processes were eliminated with an additional high execution time.

- Most of other works are restricted to the specific regions of spine bone column as such lumbar, thoracic, and others. In this study, there is no region restriction, and the proposed framework is processed on different regions.

- If the results of the proposed method is compared with most important published bone segmentation methods, the large execution process time is reduced (such as in [36, 51, 54]).

- In CT spinal images, different partial regions are scanned. For instance, some CT data have only 4-5 thorocic VBs, some of them have 2-3 lumbar VBs, and etc. A framework which is dependent of the identification of VBs in a dataset can cause high execution time. This study is not dependent on any identification step thanks to the proposed shape model and its embedding step.

E. Overview of Intensity, Spatial Interaction, and Shape Models

In this dissertation, three pieces of information (intensity, spatial interaction, and shape) are modelled to obtain the optimum segmentation. It should be noted that the data is assumed to have two classes: background and object regions which are represented as "b" or "0" and "o" or "1", respectively. The intensity information is modelled using the Gaussian distribution. The parameters of distributions ($\Theta = \mu_o, \sigma_o, \pi_o, \mu_b, \sigma_b, \pi_b$ for the mean, standard deviation, and prior probability, respectively) are estimated using the expectation-maximization (EM) method in [21] and [20]. Spatial interaction that describes the relation between pixels / voxels is modeled using a Markov-Gibbs random field (MGRF). To do this, the image is realized as a stochactic process on a random field. The MGRF models capture the spatial textural information in an image by assuming that the pixel intensity depends on the intensities of the neighboring pixels. This work deals with the homogeneous isotropic Potts model proposed by Geman et al. [3] which is similar to Derin-Elliot model in [4]. The shape variability is described using new probabilis-

tic functions to be used as a prior information. The shape model is obtained using histogram of occurrences of training shape pixels or voxels. The main objective is to capture the shape variation of the object of interest. Using the intensity, spatial interaction, and shape modelling, each pixel in the image will have probabilities (for each information) to be an object and a background class.

In this section, the problem formulation is explained. Let $\mathbf{I}$ and $\mathbf{d}$ represent the input volume and the probabilistic shape model, respectively. To use a shape prior in the segmentation process, $\mathbf{I}$ and $\mathbf{d}$ are required to be registered. In the registration process, $\mathbf{I}$ and $\mathbf{d}$ will be the source and target information, respectively. In this method, the objective is to find the desired labeling, $\mathbf{f}$, with required transformation matrix, $\mathbf{T}$ to maximize $p(\mathbf{f} \mid \mathbf{T}, \mathbf{I}, \mathbf{d})$.

The desired labeling, required transformation, input image, and probabilistic shape model, can be given by a conditional distribution using Bayes' rule as

$$p(\mathbf{f} \mid \mathbf{T}, \mathbf{I}, \mathbf{d}) \propto p(\mathbf{I} \mid \mathbf{f}) p(\mathbf{f}) p(\mathbf{d} \mid \mathbf{f}, \mathbf{T}) \tag{41}$$

where $p(\mathbf{I} \mid \mathbf{f})$ is a conditional distribution of the input image given the desired labeling, $p(\mathbf{f})$ is an unconditional probability distribution of the desired labeling, and $p(\mathbf{d} \mid \mathbf{f}, \mathbf{T})$ is a conditional distribution of the shape model given the desired labeling and estimated transformation. The Bayesian MAP estimate of the map $\mathbf{f}$ can be written as

$$\mathbf{f}^* = \arg\max_{f} L(\mathbf{I}, \mathbf{d}, \mathbf{f}, \mathbf{T}). \tag{42}$$

The objective is to maximize the log-likelihood function

$$L(\mathbf{I}, \mathbf{d}, \mathbf{f}, \mathbf{T}) = \log p(\mathbf{I} \mid \mathbf{f}) + \log p(\mathbf{f}) + \log p(\mathbf{d} \mid \mathbf{f}, \mathbf{T}). \tag{43}$$

In this study, the Iterated conditional modes (ICM) method, which was originally proposed by Besag [53], is extended into a new form by integrating the shape model to maximize Eq. 43.

a. Intensity Model To obtain a good intensity model, the conditional probability distribution, $p(\mathbf{I} \mid \mathbf{f})$, of the original image is estimated. The intensity

information is modelled using the Gaussian distribution. The Gaussian function can be written as

$$p(\mathbf{I} \mid \mathbf{f} = i) = \frac{1}{\sqrt{2\pi\sigma_i^2}} \exp(-\frac{(\mathbf{I} - \mu_i)^2}{2\sigma_i^2}) \tag{44}$$

The parameters of distributions (μ_i, σ_i) are estimated using the expectation-maximization (EM) method in [21] and [20] where $i = "0"$ and $i = "1"$ represent 'background' and 'object' classes, respectively.

b. Spatial Interaction Model Spatial interaction helps correcting errors and recovering missing information in the image labeling problem [26]. Stochastic process on a random field is used to realize the image [82]. In this study, the unconditional probability distribution of the desired map (labeling), $p(\mathbf{f})$, is obtained. To estimate $p(\mathbf{f})$, the Gibbs distribution is used. The Gibbs distribution takes the following form

$$p(\mathbf{f}) = \frac{1}{Z} \exp(-\frac{U(\mathbf{f})}{T}) \tag{45}$$

where

$$Z = \sum_{f \in \mathcal{F}} \exp(-\frac{U(\mathbf{f})}{T}) \tag{46}$$

is a normalizing constant called the partition function, T is a control parameter called the temperature which is assumed to be 1 unless otherwise stated, and $U(\mathbf{f})$ is the Gibss energy function. The energy is a sum of clique functions $V_c(\mathbf{f})$ over all possible cliques $\mathcal{C}$ as

$$U(\mathbf{f}) = \sum_{c \in \mathcal{C}} V_c(\mathbf{f}). \tag{47}$$

A clique is a set of sites in which all pairs of sites are neighbors. The clique potentials can be defined by

$$V_c(f) = \begin{cases} \gamma_c & \text{if all sites on } c \text{ have the same label} \\ -\gamma_c & \text{otherwise,} \end{cases} \tag{48}$$

where γ_c is the potential for type-c cliques. In this proposed method, the Potts model [3] which is similar to Derin-Elliot model [4] is used. This model uses the potentials of the Potts model describing the spatial pairwise interaction between

two neighboring pixels. In this method, γ_c is estimated using the method proposed by Ali et al. in [83]. For detailed information, see Appendix I.

c. Shape Model Human anatomical structures such as spine bones, kidneys, livers, hearts, and eyes may have similar shapes. These shapes usually do not differ greatly from one individual to another. There are many works which analyze the shape variability. Cootes et al. [8] proposed effective approach using principle component analysis (PCA). Abdelmumin [5] proposed another shape based segmentation method using the Level sets algorithm. Tsai et al. [14] proposed a shape model which is obtained using a signed distance function of the training data. Eigenmodes of implicit shape representations are used to model the shape variability. Their method does not require point correspondences. Their shape model is obtained using a coefficient of each training shape. Cremers [15] et al. proposed a simultaneous kernel shape based segmentation algorithm with a dissimilarity measure and statistical shape priors. This method is validated using various image sets in which objects are tracked successfully. Most published works are theoretically valuable. However, parameter optimization of the shape priors may take high execution time if the training set is large. Also, the optimization methods used in shape registration, such as the gradient descent, takes high execution time. In the proposed work, the vertebral body shape variability is analyzed using a probabilistic model. More information about the construction of the shape model and how it is used are discussed in Section III.F.

F. Proposed Framework

The proposed framework steps are described in Algorithm III.F as follows:

The overall segmentation framework is shown in Figure 42. In the next sections, data information and each steps are described in detail.

Algorithm 1 Proposed framework

A (Training)): 80 training VB shapes are used to obtain the new probabilistic shape model. In this step, manually segmented VB shape which are obtained from 20 different patients and different regions (such as cervical, thoracic, and lumbar spine bone sections) are used. Algorithm III.F.2.a (below) shows the steps of the training stage.

B) Spinal cord extraction (Pre-processing): In this process, the Matched filter is used to detect the spinal cord. This step roughly extracts the ribs and spinal processes. Also, the data size is reduced to 120x120xZ from 512x512xZ where Z is the number of slices. This step reduces the execution time of the segmentation process. The output of this phase is used in the following steps.

C) Separation of VBs (Pre-processing): In this step, two choices are given for the user(s)-i)manual selection of disk to obtain each VB in a datasets, ii) fully automatic VB separation using the histogram based information. It should be noted all steps of the framework are fully automated except this step.

D) Segmentation: In this work, three models are used to segment VBs as briefly described in Section III.E: The intensity, spatial interaction, and shape models.The following '**While**' loop is processed for the segmentation.

While $j < N_{slices}$ **do** (N_{slices}: the number of slices.)

1) The initial segmentation using the ICM method which integrates the intensity and spatial interaction information. Using the EM algorithm, $p(\mathbf{I}|\mathbf{f} = 0)$ and $p(\mathbf{I}|\mathbf{f} = 1)$ are estimated; and $p(\mathbf{f} = 0)$ and $p(\mathbf{f} = 1)$ are estimated using the MGRF modeling. Then ICM method is used to select the optimum labeling which maximizes $\log p(\mathbf{I}|\mathbf{f}) + \log p(\mathbf{f})$.

2) The shape model is registered to the initially segmented region.

3) Final segmentation is carried out using the ICM which maximizes $\log p(\mathbf{I}|\mathbf{f}) + \log p(\mathbf{f}) + \log p(\mathbf{d} \mid \mathbf{f}, \mathbf{T})$. Algorithm III.F.5.c describes the optimization of three models.

End While

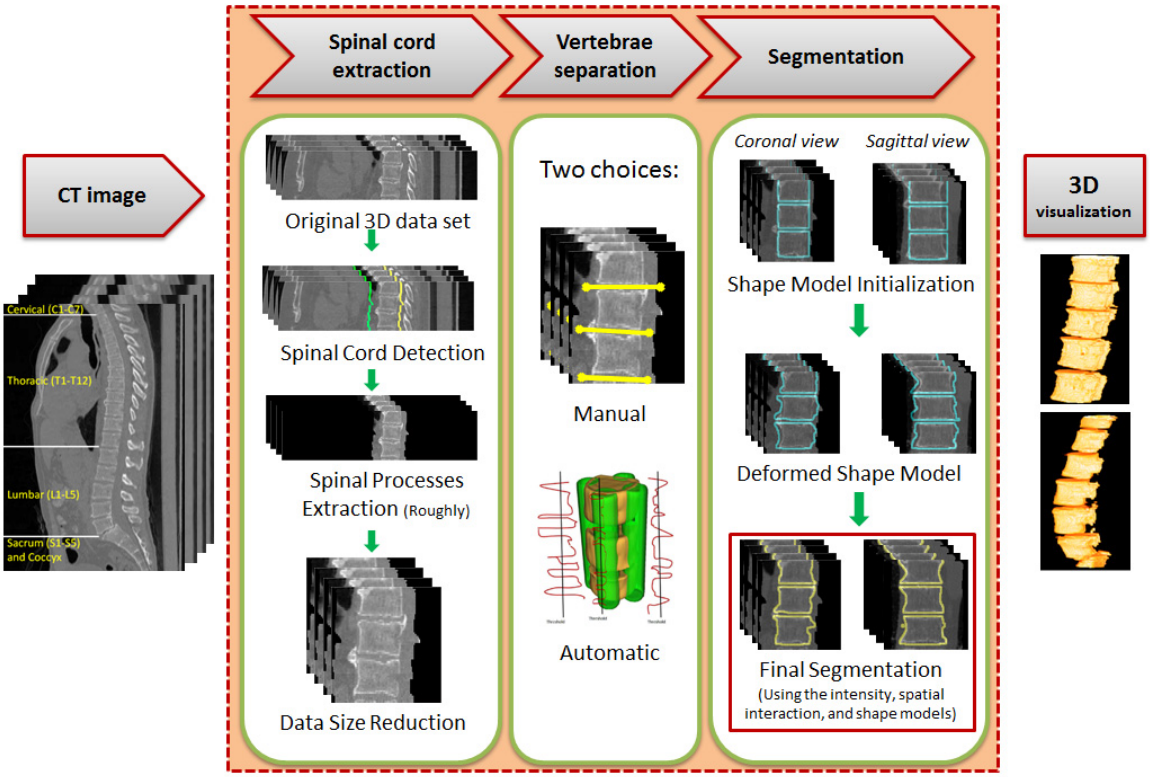

FIGURE 42 – The general segmentation framework. (Prior to this framework, it is required to obtain the shape model). In the first phase, the spinal cord is extracted, processes, and ribs roughly using the Matched filter. Also, the data size is reduced to minimize the execution time. In the second phase, the VBs are separated with two choices: i) manual, ii) automatic. In the third phase, a new shape based ICM method is proposed to segment the VBs.

1. CT Data Information

The training and testing images were acquired from GE LightSpeed VCT, Toshiba Aquilion, and Imatron C-150 CT scanners with an in-plane resolution range of $0.63 - 0.98$ mm and a slice thickness of $0.63 - 3.00$ mm. For the training stage, 80 VB cross-sections (34 thoracic, 34 lumbar, 12 cervical) are used. These VBs are selected form 10 healthy and 10 with low bone mass patients. The more information about the testing CT data sets will be given in the experimental section.

2. Shape Model Construction (Training)

a. The Registration of Training Shapes In this step, the shape is described using the same representation as described in Chapter II. The training set consists of VB shapes, $\{C_1, \ldots, C_N\}$, as shown in Figure 43; with the signed distance functions $\{\phi_1, \ldots, \phi_N\}$. Any pixel in this shape representation is shown as $\mathbf{x}$. The registration of all training shapes is done using the similar approach described in [15] and used in [81] as follows:

i) First, the average of the position factor (μ) and scale factor (σ) are obtained using the following equations

$$\mu = \begin{bmatrix} \mu_x & \mu_y \end{bmatrix}^T = \begin{bmatrix} \frac{\sum_{i=1}^{N}\sum_{\Omega} xH(-\phi_i(\mathbf{x}))}{\sum_{i=1}^{N}\sum_{\Omega} H(-\phi_i(\mathbf{x}))} & \frac{\sum_{i=1}^{N}\sum_{\Omega} yH(-\phi_i(\mathbf{x}))}{\sum_{i=1}^{N}\sum_{\Omega} H(-\phi_i(\mathbf{x}))} \end{bmatrix}^T, \tag{49}$$

$$\sigma = \begin{bmatrix} \sigma_x^2 & \sigma_y^2 \end{bmatrix}^T = \begin{bmatrix} \frac{\sum_{i=1}^{N}\sum_{\Omega}(x-\mu_x)^2 H(-\phi_i(\mathbf{x}))}{\sum_{i=1}^{N}\sum_{\Omega} H(-\phi_i(\mathbf{x}))} & \frac{\sum_{i=1}^{N}\sum_{\Omega}(y-\mu_y)^2 H(-\phi_i(\mathbf{x}))}{\sum_{i=1}^{N}\sum_{\Omega} H(-\phi_i(\mathbf{x}))} \end{bmatrix}^T, \tag{50}$$

where $H(.)$ is the Heaviside step function.

ii) A global transformation is used to register training shapes with scale and translation parameters. The transformation has scaling, $\mathbf{S}$, and translation components $\mathbf{Tr}$. Obtain the transformation parameters ($t_x,\ t_y,\ s_x,\ s_y$) for each

training shape, ϕ, as

$$\mathbf{Tr} = \begin{bmatrix} t_x & t_y \end{bmatrix}^T = \begin{bmatrix} \mu_x - \frac{\sum_\Omega xH(-\phi(\mathbf{x}))}{\sum_\Omega H(-\phi(\mathbf{x}))} & \mu_y - \frac{\sum_\Omega yH(-\phi(\mathbf{x}))}{\sum_\Omega H(-\phi(\mathbf{x}))} \end{bmatrix}^T, \tag{51}$$

$$\mathbf{S} = \begin{bmatrix} s_x & 0 \\ 0 & s_y \end{bmatrix} = \begin{bmatrix} \frac{\sigma_x}{\sqrt{\frac{\sum_\Omega (x-\mu_x)^2 H(-\phi(\mathbf{x}))}{\sum_\Omega H(-\phi(\mathbf{x}))}}} & 0 \\ 0 & \frac{\sigma_y}{\sqrt{\frac{\sum_\Omega (y-\mu_y)^2 H(-\phi(\mathbf{x}))}{\sum_\Omega H(-\phi(\mathbf{x}))}}} \end{bmatrix}^T. \tag{52}$$

iii) The transformation will be in the form $\mathbf{T}(\mathbf{x}) = \mathbf{X} = \mathbf{S}\mathbf{x} + \mathbf{Tr}$, where $\mathbf{X}$ is the transformed point of $\mathbf{x}$.

Note: In 2D case, the rotation parameter for the VB shape registration is not necessary since VB shape does not show important variation in different rotation.

Algorithm 2 Training stage (Obtaining Probabilistic Shape Model)

1. Segment training images manually.
2. Align segmented images.
3. Generate shape variation. Intersection of training shape is accepted as an object volume. The rest of the volume is accepted as variability volume except the background region.
4. Obtain the probabilities of the object and background in the variability volume of the shape model. This step will be explained more in Section III.F.2.b.

b. Shape Modeling A new probabilistic shape model is formed using the training shapes as shown in Figure 43(a). All registered training shapes are combined as shown in Figure 43(b). The shape prior represented as $\mathcal{R} = \mathcal{O} \bigcup \mathcal{B} \bigcup \mathcal{V}$ is generated. The proposed shape model functions are defined as follows:

$$\mathcal{O} = \bigcap_{i=1}^{N} H(-\phi_i), \tag{53}$$

$$\mathcal{B} = \bigcap_{i=1}^{N} H(\phi_i), \tag{54}$$

$$\mathcal{V} = \bigcup_{i=1}^{N} H(-\phi_i) - \bigcap_{i=1}^{N} H(-\phi_i), \tag{55}$$

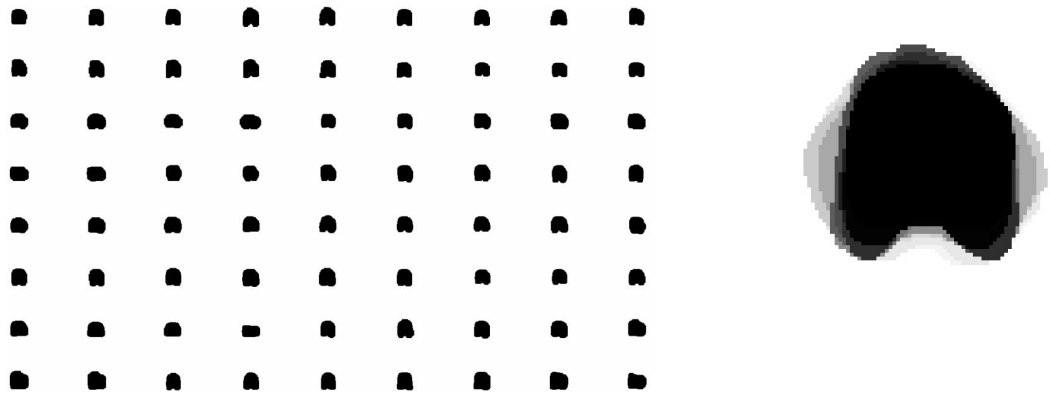

(a) (b)

FIGURE 43 – (a)The training VB images. In this experiment, 80 VB shapes which are obtained from 20 different patients and different regions (such as cervical, thoracic, and lumbar spine bone sections) are proposed. (b) The average shape of all training VB images. The darker color represents the higher object probability.

where ϕ_i^t represents any training shape. Figure 44 shows the detailed description of the shape models. The green color shows the background region ($\mathcal{B}$) which does not have any intersection with any training shape. The blue color shows the object region ($\mathcal{O}$) which is the intersection of all training shapes. In (a), the gray color represents the variability region ($\mathcal{V}$) that can be described as the union of all projected training shapes subtracted by the intersection of those shapes. In this variability region, the object and background probabilistic shapes are modeled. The red color, in (b), shows the outer contour of the variability region, and it is represented as (**J**). In the registration step, the shape model is embedded to the initially segmented region. **J** is used to estimate the registration parameters. The object ($p(\mathbf{d} \mid \mathbf{f} = 1)$) and background ($p(\mathbf{d} \mid \mathbf{f} = 0)$) probabilistic models are defined in the variability region. The probabilistic shape models are defined as follows:

- If $\mathbf{x} \in \mathcal{O}$, then $p(d_{\mathbf{x}} \mid f_{\mathbf{x}} = 1) = 1$ and $p(d_{\mathbf{x}} \mid f_{\mathbf{x}} = 0) = 0$

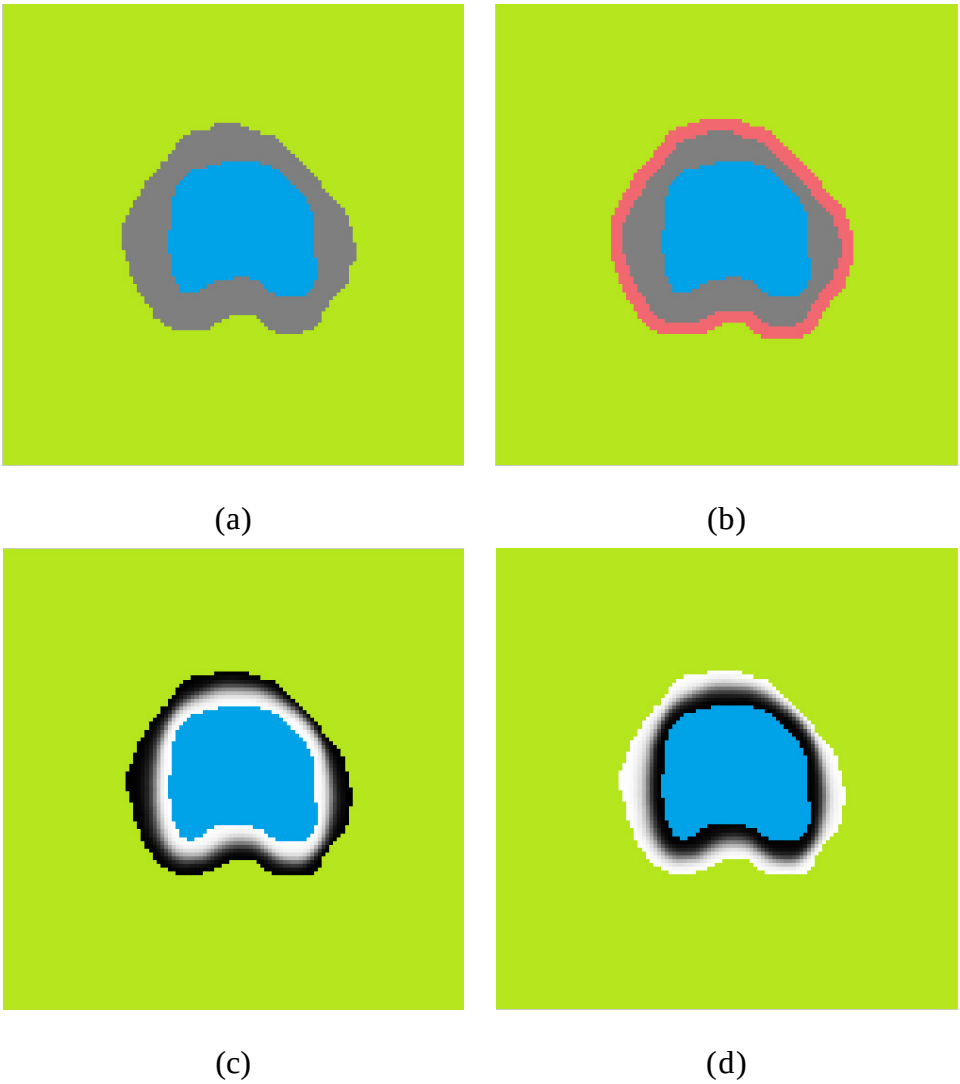

FIGURE 44 – The shape model. The green color shows the background region which does not have any intersection with any training shape. The blue color shows the object region which is the intersection of all training shapes. (a) The gray color represents the variability region that can be described as the union of all projected training shapes subtracted by the intersection of those shapes. In this variability region, the object and background probabilistic shapes are defined. (b) The red color shows the outer contour of the variability region. (c) The object ($p(\mathbf{d} \mid \mathbf{f} = 1)$) and (d) background ($p(\mathbf{d} \mid \mathbf{f} = 0)$) shapes are modelled in the variability region in which the pixel values are defined in $(0 : 1)$.

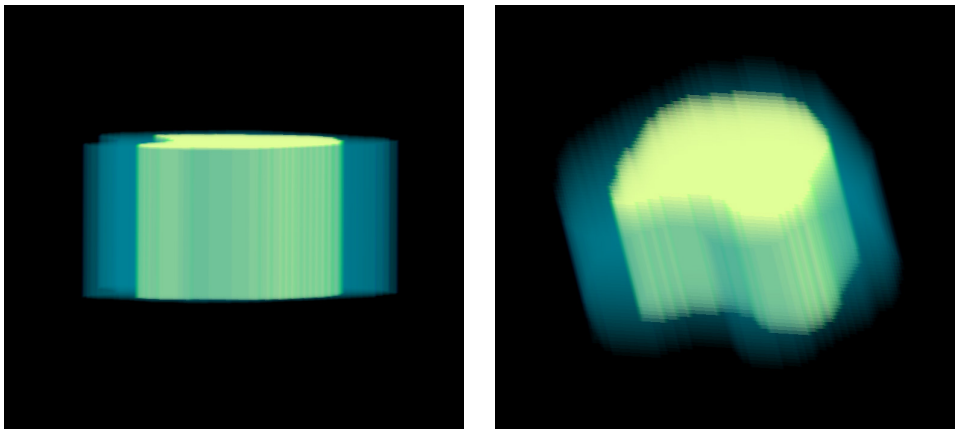

FIGURE 45 – The shape model is shown in 3D (when propagating 2D shape model into 3D). The outer volume represents the variability region, the inner volume represents the object region.

- if $\mathbf{x} \in \mathcal{B}$, then $p(d_{\mathbf{x}} \mid f_{\mathbf{x}} = 1) = 0$ and $p(d_{\mathbf{x}} \mid f_{\mathbf{x}} = 0) = 1$

- if $\mathbf{x} \in \mathcal{V}$, then

$$p(d_{\mathbf{x}} \mid f_{\mathbf{x}} = 1) = \frac{\sum_{i=1}^{N} H(-\phi_i(\mathbf{x}))}{N}, \tag{56}$$

$$p(d_{\mathbf{x}} \mid f_{\mathbf{x}} = 0) = \frac{\sum_{i=1}^{N} H(\phi_i(\mathbf{x}))}{N}. \tag{57}$$

3D representation of the shape model is shown in Figure 45. It should be noted that Eqs. 56 and 57 represents the probability value at each pixel, $\mathbf{x}$.

3. Spine Cord Extraction

As a pre-processing step, the spinal cord is extracted using the Matched filter. This process helps to remove the spinal processes roughly; hence the shape

model will be registered to the image domain easily. In the first step, the Matched filter (MF) [64, 84, 85] is employed to detect the VB automatically. This procedure eliminates the user interaction and improves the segmentation accuracy. Let $f(x, y)$ and $g(x, y)$ be template and test images, respectively. To compare the two images for various possible shifts τ_x and τ_y, one can compute the cross-correlation $c(\tau_x, \tau_y)$ as

$$c(\tau_x, \tau_y) = \int\int g(x, y) f(x - \tau_x, y - \tau_y) dx dy, \tag{58}$$

where the limits of integration are dependent on $g(x, y)$. The Eq. 58 can also be written as

$$\begin{aligned} c(\tau_x, \tau_y) &= \int\int G(f_x, f_y) F^*(f_x, f_y) \exp(j2\pi(f_x\tau_x + f_y\tau_y)) df_x df_y \\ &= FT^{-1}(G(f_x, f_y) F^*(f_x, f_y)), \end{aligned} \tag{59}$$

where $G(f_x, f_y)$ and $F(f_x, f_y)$ are the 2-D FTs of $g(x, y)$ and $f(x, y)$, respectively with f_x and f_y denoting the spatial frequencies. The test image $g(x, y)$ is filtered by $H(f_x, f_y) = F^*(f_x, f_y)$ to produce the output $c(\tau_x, \tau_y)$. Hence, $H(f_x, f_y)$ is the correlation filter which is the complex conjugate of the 2-D FT of the reference image $f(x, y)$. Figure 46(a) shows the reference image used in the Matched filter. Some examples of the VB detection are shown in Figures 46(b-d). The Matched filter is tested using 4000 clinical CT images. The detection accuracy for the VB region is 97.2%. The detection accuracy is increased to around 100% by smoothing all detected points of a dataset in the z-axis.

To extract the spinal processes and ribs roughly, some simple steps are followed as shown in Figure 47. These steps are required to: i) extract the spinal processes and ribs roughly, ii) crop the ROI minimize the execution time. Figures 48-50 show different examples of this stage in the sagittal view.

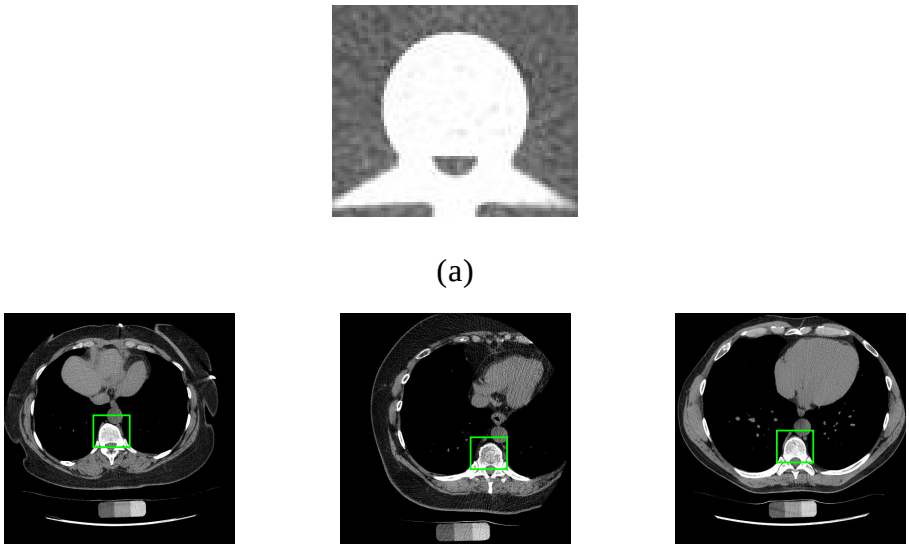

(a) (b) (c) (d)

FIGURE 46 – (a) The template used for the Matched filter, (b-d) a few images of automatic VB detection. The green line shows the detection of VB region.

4. Vertebrae Separation

This process is required in the proposed framework hence the shape model is registered to each VB in an easy way. In this process, two methods are suggested to separate each vertebrae. The first suggestion is the manual separation, and the second one is the previously proposed automatic framework [86] as shown in Figure 51. The advantage of automatic separation is to eliminate user interaction(s). However, there are two disadvantages: i) increased error, ii) current methods in the literature have higher execution time respect to the manual methods.

To give the user his own choice, two methods are described.

a. Manual After the spinal cord, processes, and ribs are extracted roughly, we need to separate adjacent VBs in order to embed the shape model to the image domain. In the manual separation, simple manual annotations are needed to specify the cut-points of VBs. For instance, if there are three VBs in the dataset, six points are annotated on the image. In the experiments, the average execution time to separate 12 adjacent VBs is 18 seconds. This timing may still not be optimum one, however, with manual annotations there should not be any possible

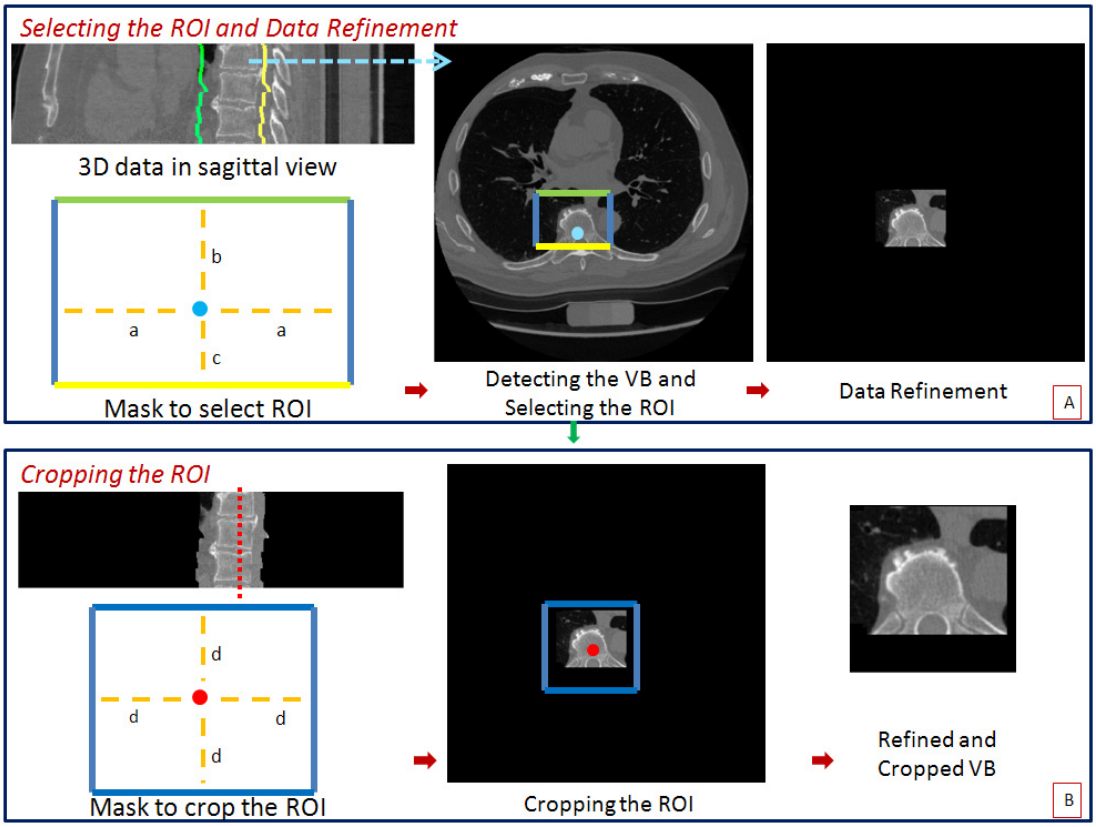

FIGURE 47 – In the first step, the MF is run on each slice of the 3D data. The output of this process is the detected points of each CT slices as shown with the blue dot. After the center points are detected, a mask is used to refine the data to specify the region of interest (ROI). In the mask, it is accepted that $a = 50$, $b = 60$, and $c = 20$. Any user can change these values. But the user should be careful to extract the spinal processes and ribs roughly. Then, another mask can be used to crop the ROI using the average center points (the red color) of all slices of 3D data. $d = 60$ is accepted to capture the VB region.

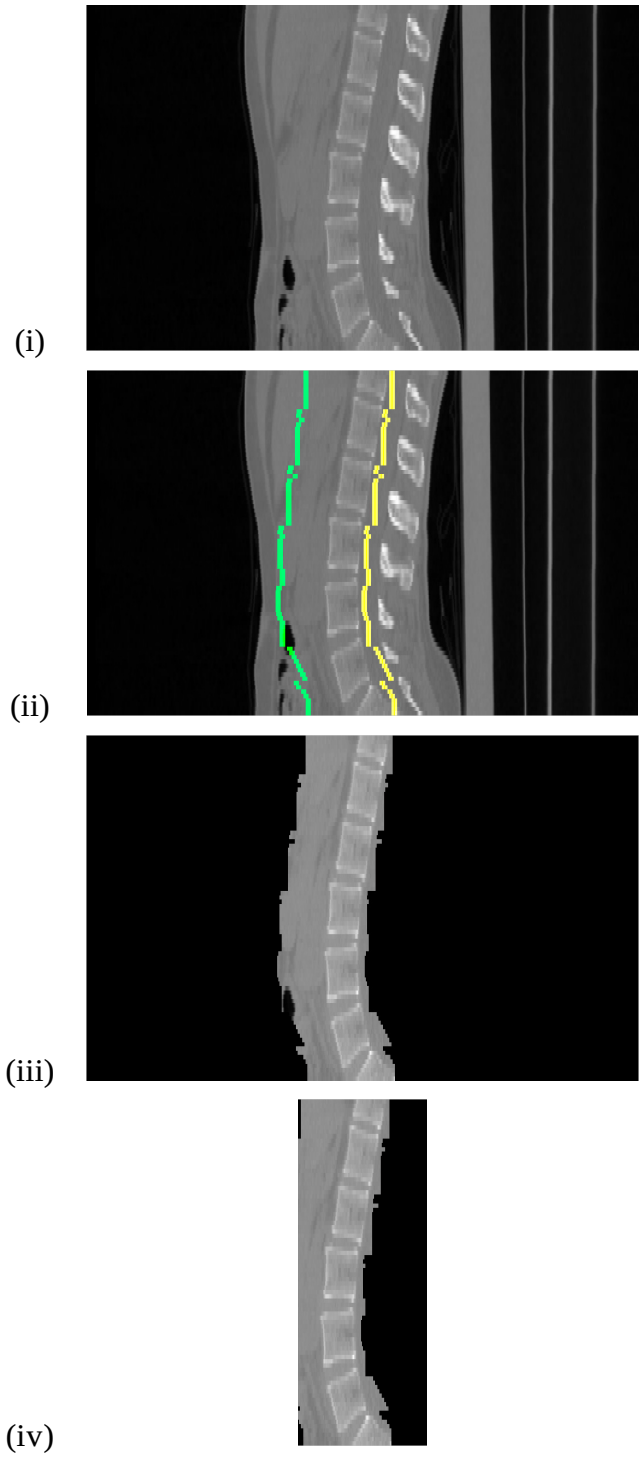

FIGURE 48 – The extraction of the spinal cord on a data set (Example-1). (i) Sagittal view of each data. (ii) The detected VB region. (iii) The refined data to extract the spinal processes and ribs. (iv) The cropped data to reduce the size of the image.

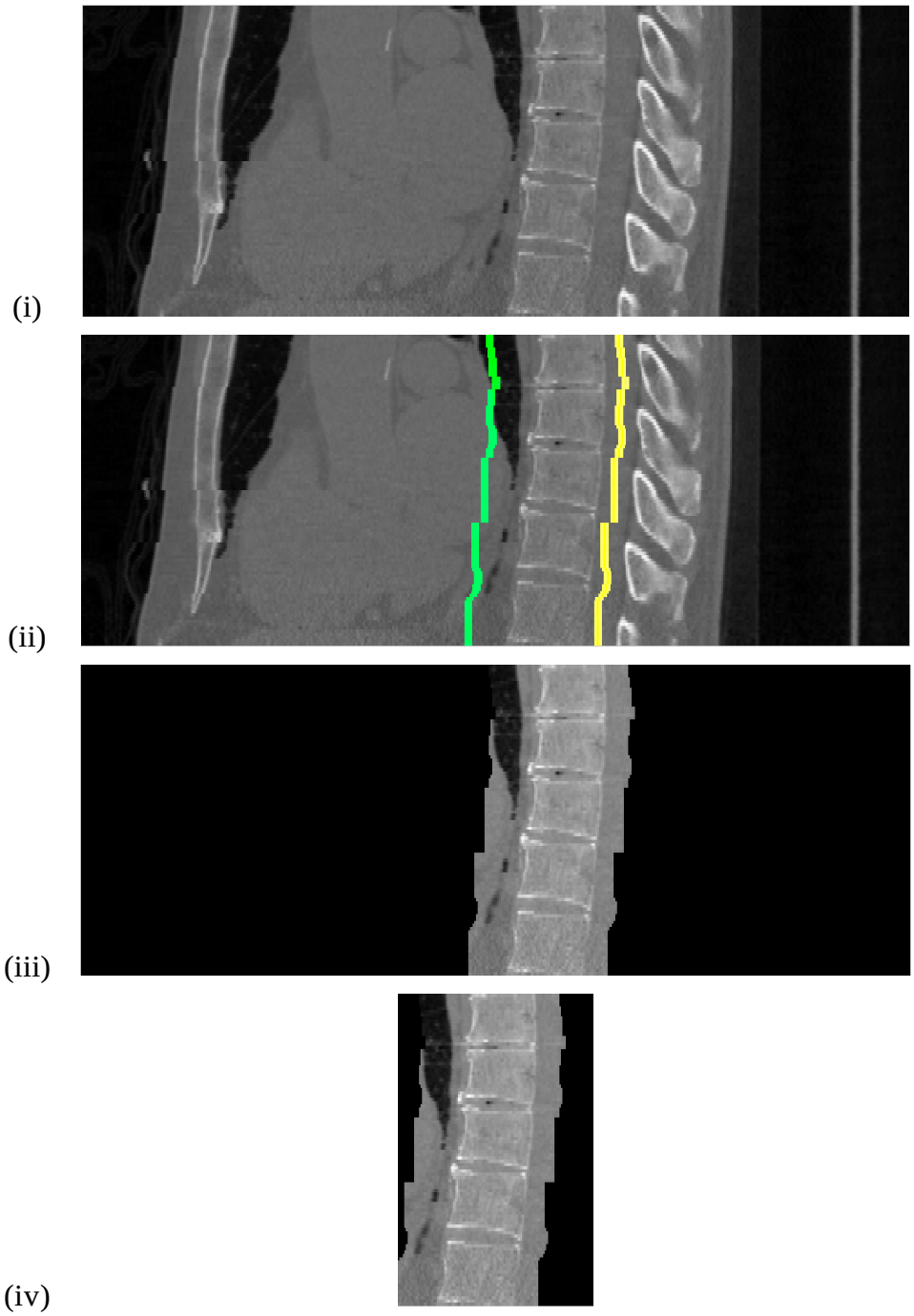

FIGURE 49 – The extraction of the spinal cord on a data set (Example-3). (i) Sagittal view of each data. (ii) The detected VB region. (iii) The refined data to extract the spinal processes and ribs. (iv) The cropped data to reduce the size of the image.

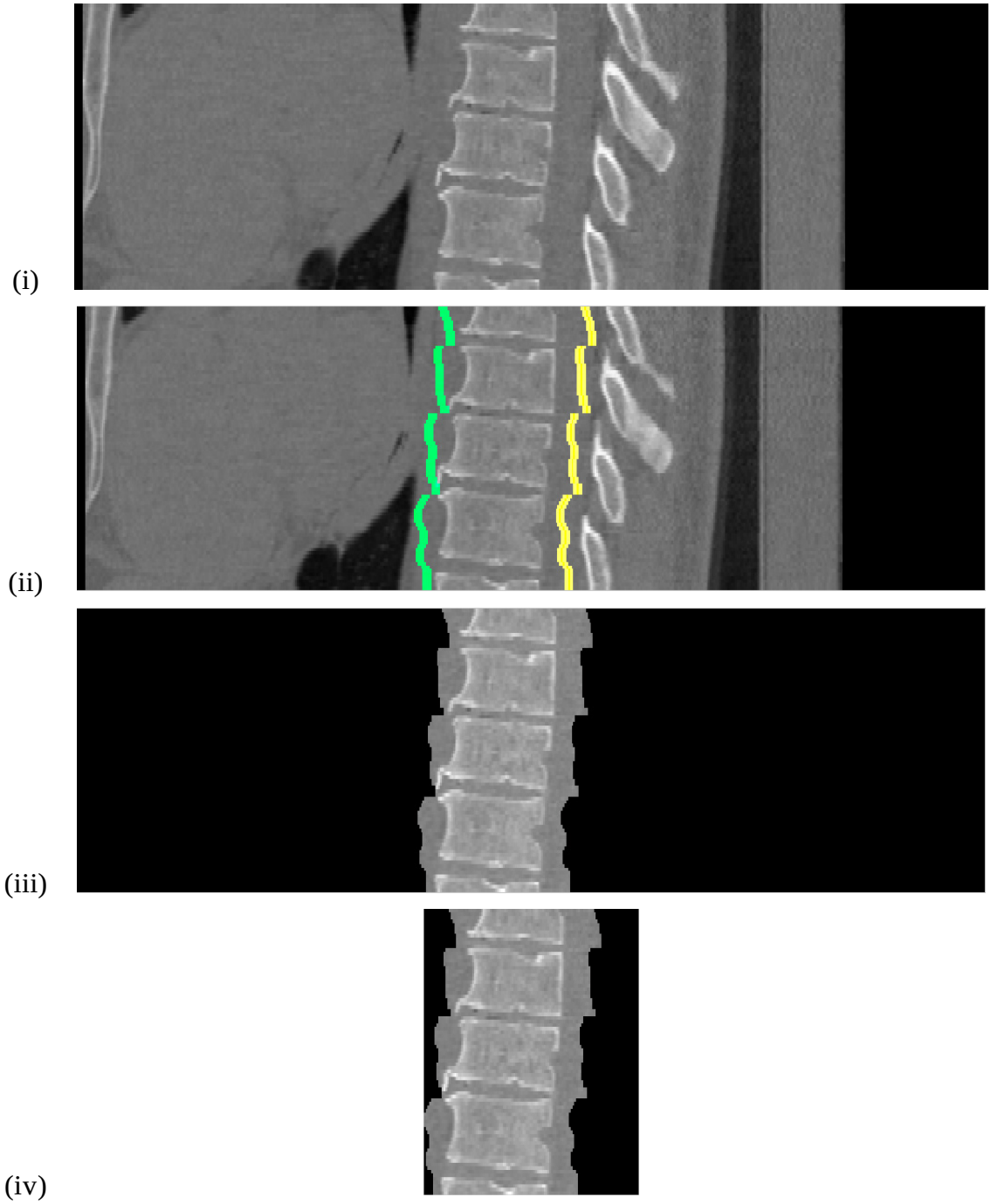

FIGURE 50 – The extraction of the spinal cord on a data set (Example-5). (i) Sagittal view of each data. (ii) The detected VB region. (iii) The refined data to extract the spinal processes and ribs. (iv) The cropped data to reduce the size of the image.

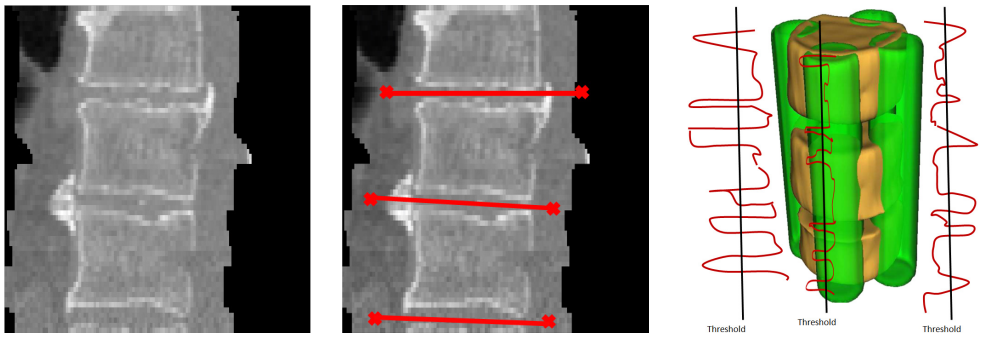

(a) (b) (c)

FIGURE 51 – The separation of each VB in a data set. Two choices are given to the user: The Manual and automatic options. Each option has its own advantages and disadvantages which are described the section. (a) An image which has 3 adjacent VBs. (b) The manual separation process with 6 points selected by a user. (c) The automatic separation method which was proposed by Aslan et al. in [86].

data loss. In the next section, the automated separation process, which Aslan et al. previously published in [86], is described. It should be noted that segmentation accuracy is measured when the VBs are separated manually.

b. Automatic In this section, a 3D framework to separate vertebral bones in CT images without any user intervention [86] is used. To separate the VBs, the previously developed approach based on four points automatically placed on cortical shell is used. An example of separation and segmentation of a VB is shown in Figure 51(c). After the spinal cord is extracted; the approximate centerline of VB column is obtained. These seeds are placed using the relatively higher gray level intensity values of the cortex region.

Next, the histogram for a neighborhood around each seed is obtained. The histogram represents the number of voxels whose intensity values are above 200 Hounsfield Unit (HU). This value is obtained empirically. Vertical boundaries of a VB show higher gray level intensity than inner region of the VB and disks. Figure 51(c) shows histograms (the red line), and thresholds (the black line). To search vertical limits of the VB, the following adaptive threshold equation is used as follows:

$$TH = \mu(A) + \kappa * [\max(A) - \mu(A)], \tag{60}$$

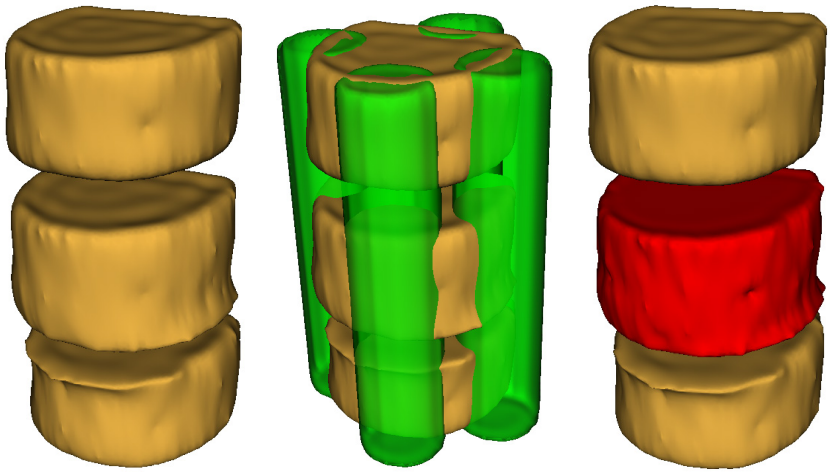

(a) (b) (c)

FIGURE 52 – The separation of the VB region. (a) 3D view of three adjacent VB, (b) automated placement of four seeds on cortical bone and disc, (c) separation of VB shown with red color.

where $\kappa = 0.3$ which is derived from experiments by trial-and-error, where A represents each histogram vector with the red line as shown in Fig 51(c), $\max(A)$ and $\mu(A)$ are the maximum and average values in the histogram vector.

In the separation step, 30 patients which totals to 117 VBs are used. The results can be classified as in [77]. There are five respective categories as described below.

- Excellent: The VB is successfully separated without any misclassification. Vertical limits are correctly obtained.
- Good: The VB is separated with small parts of adjacent disk or VB. Around 90% or vertical limits are correctly obtained.
- Bad: The VB is separated, however noticeable parts of it are missed. Around $70 - 90\%$ of vertical limits are correctly obtained.
- Poor: Large portions of anatomical structure of VB are missed. Around $50 - 70\%$ of vertical limits are correctly obtained.
- Fail: The VB is not separated due to challenges.

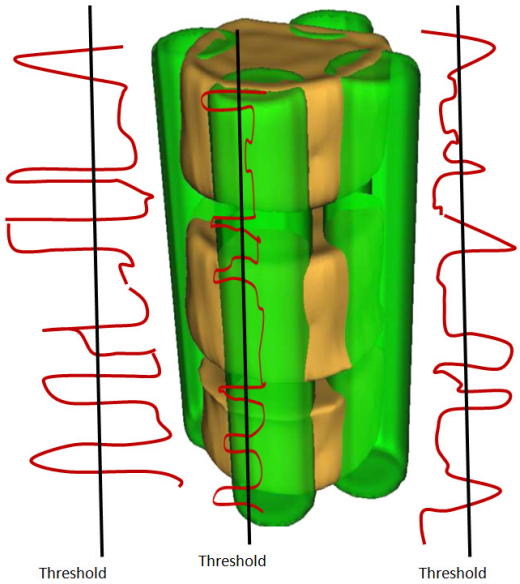

FIGURE 53 – The VB separation: The green volume shows the four four seeds. The red lines correspond to the number of voxels whose gray level are bigger than 200 HU. The black lines correspond to the threshold written in Eq. 60.

The proposed method produced about 85% successful separation results, if excellent and good grades are considered. Hence, 15% separation results were considered as fair, bad, or fail.

5. Segmentation

Intensity and interaction models may not be enough to obtain optimum segmentation. To segment the VB, a new shape based iterated conditional modes method which integrates the models of the intensity, spatial interaction, and shape prior information is proposed. The proposed method presents several advantages which can be written as: i) the probabilistic shape model is automatically registered to the testing image, hence manual interaction is eliminated, ii) the registration benefits from the segmented region to be used in the shape representation, and iii) the probabilistic shape model refines the initial segmentation result using the registered variability volume.

The segmentation part has following steps: 1) initial segmentation using only intensity and spatial interaction information (this step is needed to obtain the

feature correspondence between the image domain and shape model), 2) shape model registration, and 3) the final segmentation using three models.

a. Initial Segmentation To estimate the initial labeling $\mathbf{f}^*$, the ICM method which integrates the intensity and spatial interaction information is used. The same method described in Section III.F.5.c (without shape prior) is used. It should be noted that the shape model has not been used in this process. The initial segmented region is used to obtain the SDF representation which is required in the registration process. An example of the initial labeling is shown in Fig 54. The method has acceptable results, because a relatively large amount of pedicles and ribs are separated from the vertebral body. It should be noted that there may still some portion of pedicles and ribs which could not be separated. Between Figure 54(c) and (d), there is a shape registration process which is shown in Figures 55-56.

b. Embedding the Shape Model To use the shape prior in the segmentation process, $\mathbf{f}^*$ and the shape prior are required to be registered. The shape model has a variability region as shown in Figure 44(a). The outer contour is represented as $\mathbf{J}$. In the registration process, $\mathbf{J}$ and $\mathbf{f}^*$ will be the source and target information, respectively. The registration step is done in 2D slice by slice since the shape model can deform locally independently from other slices. This approach gives deformation flexibility between each slices which stocks in z-axis. The transformation has four parameters such as s_x, s_y (for scale, $\mathbf{S}$), and t_x, t_y (for translation, $\mathbf{Tr}$). It should be noted that the rotation is not necessary in the method since the registration is done slice by slice; and the VB does not show important rotational variation in the axial axes. Let us define the transformation result by β that is obtained by applying a transformation $\mathbf{T}$ to a given contour / surface α. In this case, β and α correspond to $\mathbf{f}^*$ and $\mathbf{J}$, respectively. The transformation can be written for any point $\mathbf{X}$ in the space as $\mathbf{T}(\mathbf{x}) = \mathbf{X} = \mathbf{S}\mathbf{x} + \mathbf{Tr}$. Now consider $\mathbf{x} \in \phi_{\mathbf{J}}$ and $\mathbf{X} \in \phi_{\mathbf{f}^*}$. To register the shape model to the image domain, the similar approach is followed as described in Section III.F.2.a.

The registration of the shape model and testing image is done as follows:

i) First, the average of the position factor ($\mu^{\mathbf{f}^*}$) and scale factor ($\sigma^{\mathbf{f}^*}$) are obtained using the following equations

$$\mu^{\mathbf{f}^*} = \begin{bmatrix} \mu_x^{\mathbf{f}^*} & \mu_y^{\mathbf{f}^*} \end{bmatrix} = \begin{bmatrix} \frac{\sum_\Omega xH(-\phi_{\mathbf{f}^*}(\mathbf{x}))}{\sum_\Omega H(-\phi_{\mathbf{f}^*}(\mathbf{x}))} & \frac{\sum_\Omega yH(-\phi_{\mathbf{f}^*}(\mathbf{x}))}{\sum_\Omega H(-\phi_{\mathbf{f}^*}(\mathbf{x}))} \end{bmatrix}^T, \tag{61}$$

$$\sigma^{\mathbf{f}^*} = \begin{bmatrix} (\sigma_x^{\mathbf{f}^*})^2 & (\sigma_y^{\mathbf{f}^*})^2 \end{bmatrix} = \begin{bmatrix} \frac{\sum_\Omega (x-\mu_x^{\mathbf{f}^*})^2 H(-\phi_{\mathbf{f}^*}(\mathbf{x}))}{\sum_\Omega H(-\phi_{\mathbf{f}^*}(\mathbf{x}))} & \frac{\sum_\Omega (y-\mu_y^{\mathbf{f}^*})^2 H(-\phi_{\mathbf{f}^*}(\mathbf{x}))}{\sum_\Omega H(-\phi_{\mathbf{f}^*}(\mathbf{x}))} \end{bmatrix}^T. \tag{62}$$

ii) Obtain the transformation parameters ($t_x,\ t_y,\ s_x,\ s_y$) for the shape model, $\phi_{\mathbf{J}}$, as

$$\mathbf{Tr} = \begin{bmatrix} t_x & t_y \end{bmatrix}^T = \begin{bmatrix} \mu_x^{\mathbf{f}^*} - \frac{\sum_\Omega xH(-\phi_{\mathbf{J}}(\mathbf{x}))}{\sum_\Omega H(-\phi_{\mathbf{J}}(\mathbf{x}))} & \mu_y^{\mathbf{f}^*} - \frac{\sum_\Omega yH(-\phi_{\mathbf{J}}(\mathbf{x}))}{\sum_\Omega H(-\phi_{\mathbf{J}}(\mathbf{x}))} \end{bmatrix}^T, \tag{63}$$

$$\mathbf{S} = \begin{bmatrix} s_x & 0 \\ 0 & s_y \end{bmatrix} = \begin{bmatrix} \frac{\sigma_x^{\mathbf{f}^*}}{\sqrt{\frac{\sum_\Omega (x-\mu_x^{\mathbf{f}^*})^2 H(-\phi_{\mathbf{J}}(\mathbf{x}))}{\sum_\Omega H(-\phi_{\mathbf{J}}(\mathbf{x}))}}} & 0 \\ 0 & s_y = \frac{\sigma_y^{\mathbf{f}^*}}{\sqrt{\frac{\sum_\Omega (y-\mu_y^{\mathbf{f}^*})^2 H(-\phi_{\mathbf{J}}(\mathbf{x}))}{\sum_\Omega H(-\phi_{\mathbf{J}}(\mathbf{x}))}}} \end{bmatrix}^T. \tag{64}$$

iii) Transform each point $\mathbf{x} \in \Omega$ to the new point $\mathbf{X}$. Hence, the shape model is registered to the image domain.

iv)The new probabilistic function at each pixel is $p(d_{\mathbf{X}} \mid f_{\mathbf{X}}) = p(d_{\mathbf{x}} \mid f_{\mathbf{x}}, \mathbf{T})$. Hence, the new transformed pixels will have the same probabilistic value with corresponding pixels. An example of the registration and final segmentation results are shown in Figures 55-56.

c. Final Energy Minimization Using Three Models: Intensity, Spatial Interaction, and Shape As described in Section III.E, three probabilistic models are used. Before this step, the followings are obtained already i) the initial labeling $\mathbf{f}^*$ that maximizes $p(\mathbf{I} \mid \mathbf{f}^*)$, ii) the MGRF model for $p(\mathbf{f}^*)$, and iii) the transformed shape prior to maximize $p(\mathbf{d} \mid \mathbf{f}^*, \mathbf{T})$. It should be noted that the transformation step is not an iterative process, and there is a unique solution for a given initial segmentation and shape model. Now, the objective is to optimize the following equation to maximize the likelihood energy functional.

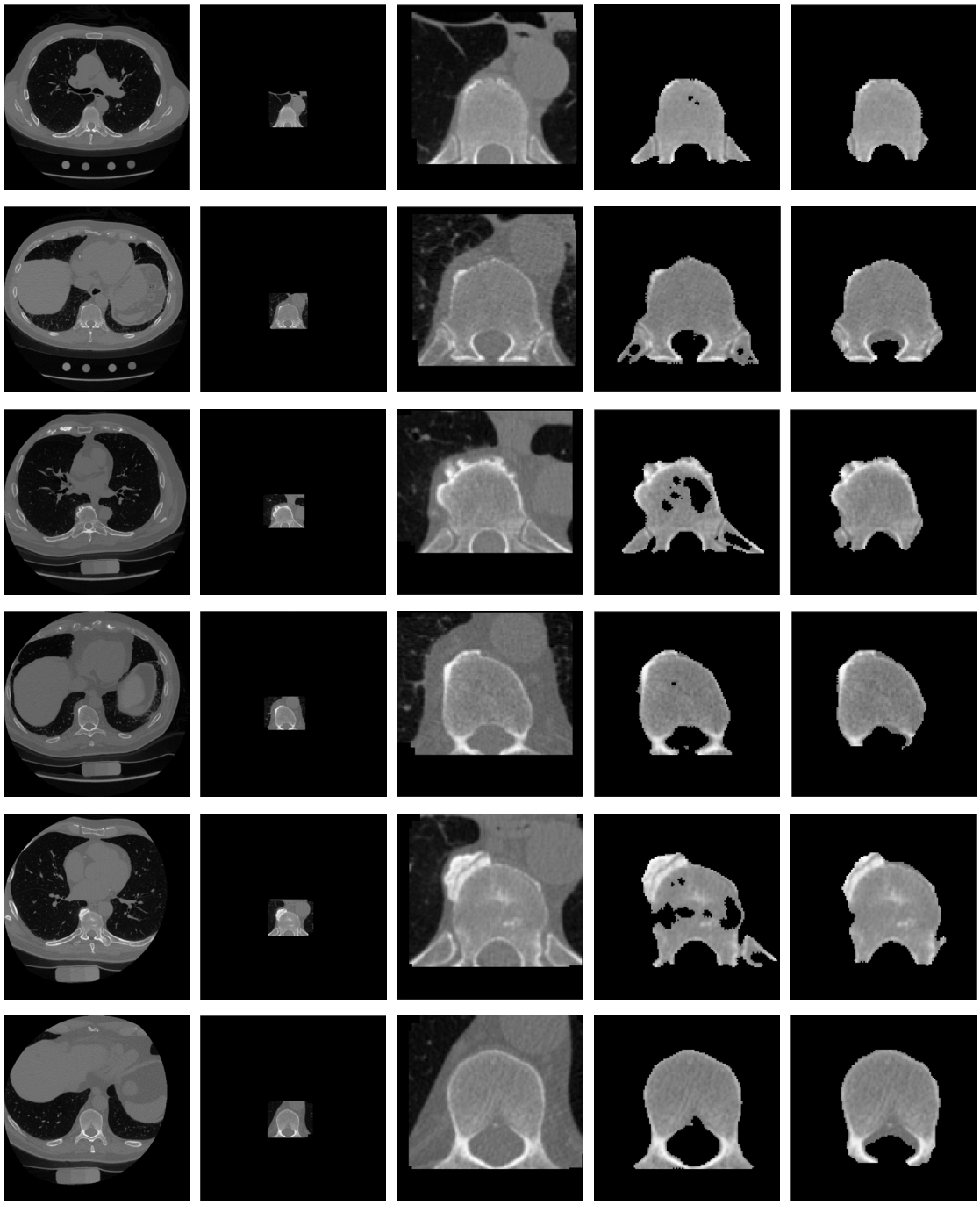

(a) (b) (c) (d) (e)

FIGURE 54 – An example of the initial labeling. (a) Original CT images, (b) detection of the VB region and refinement, (c) the cropped VB region, (d) the initial labeling, $\mathbf{f}^*$ using only the intensity and spatial interaction models, and (e) the final segmentation using three models.

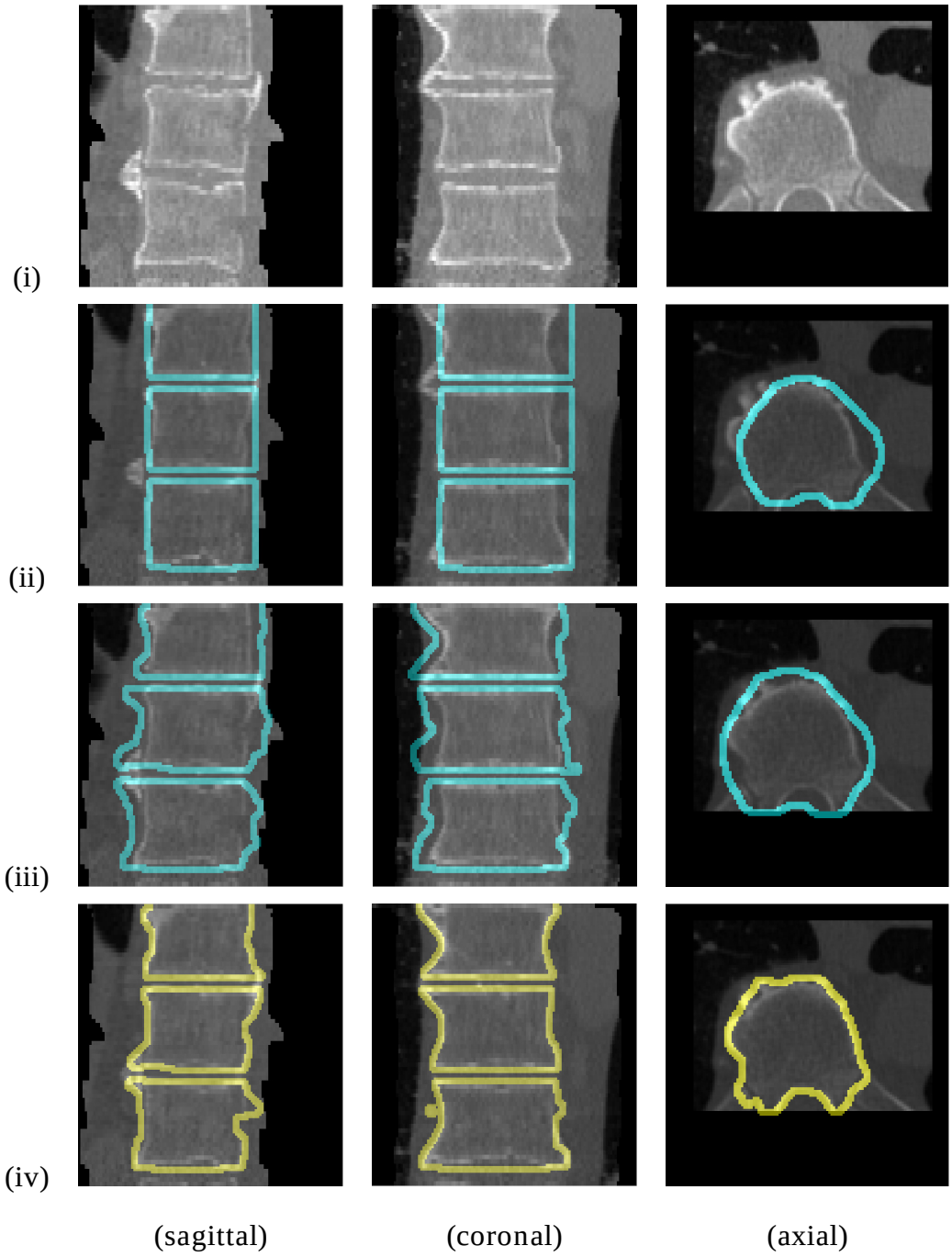

FIGURE 55 – Embedding the shape model to the image domain and the final segmentation. (i) A CT data after the extraction of spinal cord. (ii) Shape model initialization (the blue color show the outer surface of the variability region **J**). The contour **J** is placed equally in every slice using the obtained ROI. (iii) Embedding the shape model to the image domain. (iv) Final segmentation using three models: The intensity, spatial interaction, and shape information. Images and results are shown in the (a) sagittal, (b) coronal, and (c) axial views.

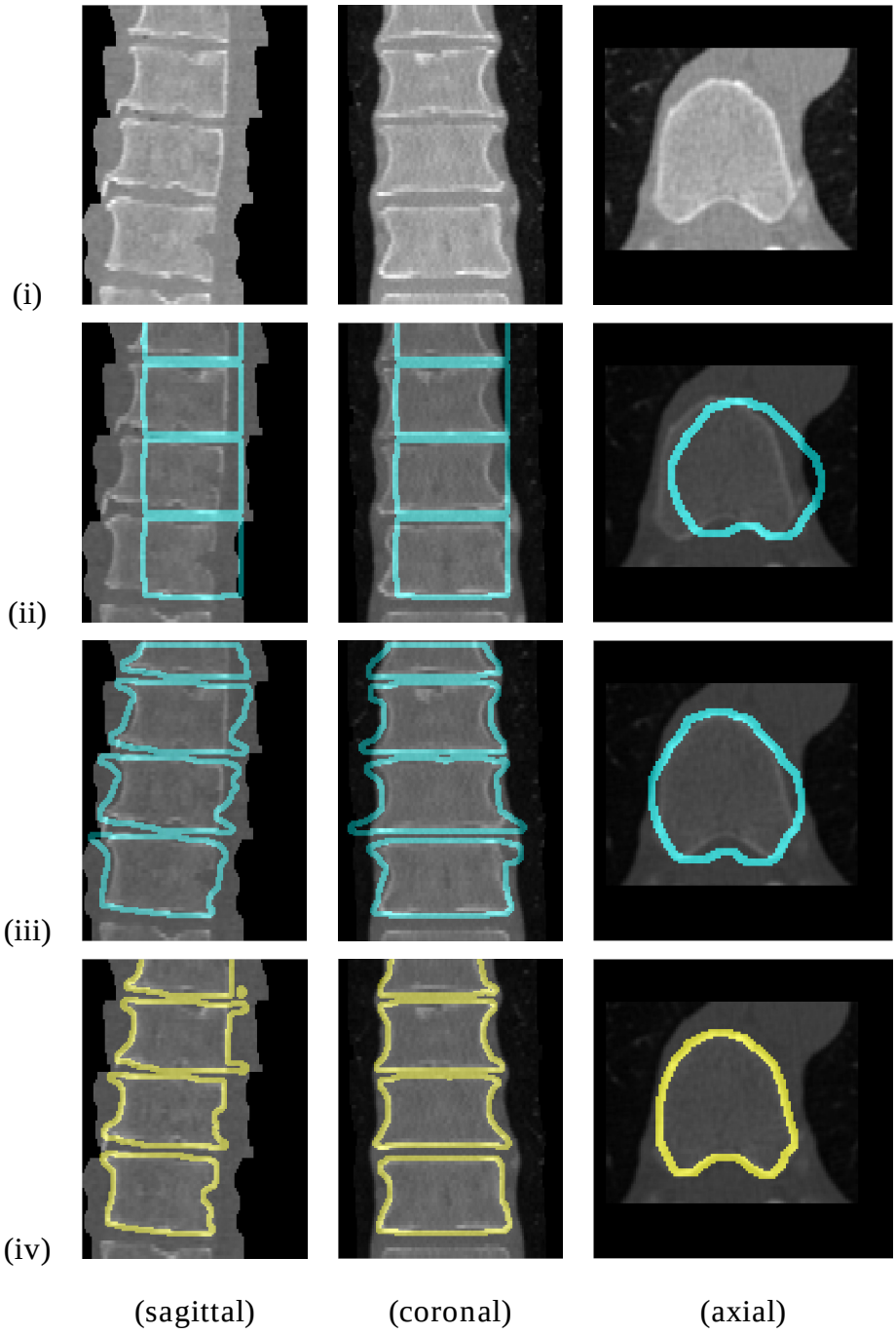

FIGURE 56 – Embedding the shape model to the image domain and the final segmentation. (i) A CT data after the extraction of spinal cord. (ii) Shape model initialization (the blue color show the outer surface of the variability region **J**). The contour **J** is placed equally in every slice using the obtained ROI. (iii) Embedding the shape model to the image domain. (iv) Final segmentation using three models: The intensity, spatial interaction, and shape information. Images and results are shown in the (a) sagittal, (b) coronal, and (c) axial views.

Algorithm 3 Optimization of Three Models

1. While $i < N_{iter}$ do
   2. For all $\mathbf{X} \in \Omega$ do
      3. Update $f^*_{\mathbf{X}}$ by the value of $f_{\mathbf{X}}$ which maximizes

$$\underline{\log p(I_{\mathbf{X}} \mid f_{\mathbf{X}}) + \log p(f_{\mathbf{X}}) + \log p(d_{\mathbf{X}} \mid f_{\mathbf{X}})}$$

   4. End for
   5. Increase i
6. End while

Note: It should be noted that $\mathbf{X} = \mathbf{Sx} + \mathbf{Tr}$ is any transformed pixel,and Ω is the pixel domain in the image.

$$L(\mathbf{I}, \mathbf{d}, \mathbf{f}, \mathbf{T}) = \log p(\mathbf{I} \mid \mathbf{f}) + \log p(\mathbf{f}) + \log p(\mathbf{d} \mid \mathbf{f}, \mathbf{T}). \tag{65}$$

Algorithm III.F.5.c shows the proposed segmentation process using a new ICM method.

G. Experiments and Results

1. CT Data Information

For the testing stage, 18 patient data sets, of which 10 are from female ('F') and 8 are from male ('M'), and a phantom are examined in this study. There are $16-96$ axial slices with 512x512 voxels. The proposed algorithm is tested on 932 CT slices / 66 VBs which are obtained from different spine bone regions (i.e. lumbar, thoracic, and etc.). In the datasets, the number of visible VBs changes from $2-8$. The data sets are also categorized as 'healthy' (H) and 'with low bone mass' (L) with respect to their calcium absorbtion. The experiments are run on 7 'H' and 11

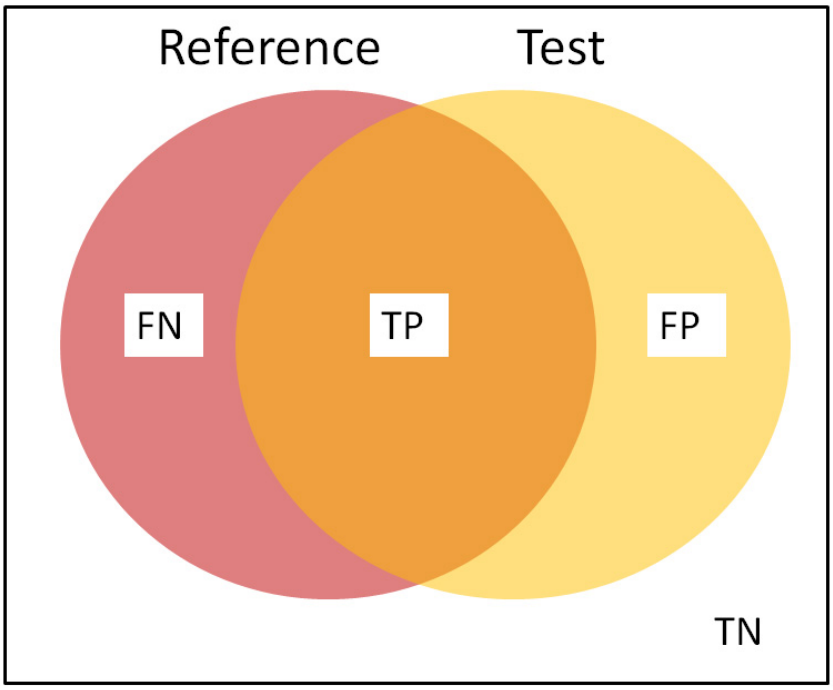

FIGURE 57 – In the segmentation quality measurements, there are 4 regions to be considered as: True positive (TP), false positive (FP), true negative (TN), and false negative (FN). The reference and test regions represent the ground truth and automatic segmented regions.

'L' data sets. The ages of the test subjects varies between $38 - 76$ years with an average age of 61.3 years with 12.2 years standard deviation.

2. Segmentation Measurements

Figure 57 shows the region of true positive (TP), true negative (TN), false positive (FP), and false negative (FN). In this figure, the reference region represents the ground truth which is verified by a radiologist. The test region represents the automated segmented region. For the ESP, the segmentation quality is measured using the Jaccard distance whereas for the clinical data sets, the segmentation quality is measured using four difference formulations. The measurements can be defined as follows:

$$\text{ACCURACY (\%)} = 100 * \frac{TP + TN}{TP + FP + FN + TN} \tag{66}$$

$$\text{PRECISION (\%)} = 100 * \frac{TP}{TP + FP} \tag{67}$$

$$\text{JARRARD COEFFICIENT (\%)} = 100 * \frac{TP}{TP + FN + FP} \tag{68}$$

$$\text{DICE'S COEFFICIENT (\%)} = 100 * \frac{2TP}{2TP + FP + FN} \tag{69}$$

3. Validation Using the Phantom

In the experiments, the ESP, which is an accepted standard for quality control [68] in bone densitometry, is used to validate the segmentation algorithms. Because clinical CT images have gray level inhomogeneity, noise, and weak edges in some slices, the ESP was scanned with the same problems to validate the robustness of any method. CT images may have various noise and image uncertainties. Image noise is related to the numbers of x-ray photons absorbed by each small area of the image [87]. The higher exposure levels result in a better image, and less image noise, but more radiation is absorbed by a patient. Hence, segmentation methods should be robust to various image conditions. It is assumed that CT images may have random noise. To assess the proposed method under various challenges, Gaussian noise with a zero mean and different variance σ_n^2 values (from 0 to 0.5) is added to the CT images. The segmentation accuracy is measured for each method using the ground truths. The proposed method is compared with other three alternatives which can be represented as follows: $A1$: Active appearance method described in [9], $A2$: Level sets method described in [25], and $A3$: Shape based level sets method described in [81].

[1] All algorithms are run on a PC with a 3Ghz AMD Athlon 64 X2 Dual processor with 3GB RAM.

The segmentation results and the average accuracy on the ESP (when the initialization is optimal) are shown in Figure 58 and Figure 60, respectively. In this test, the initial point is chosen at the center of the object of interest. The elapsed time[1] to segment 12 ESP images is 136.2 seconds for $A1$, 194 seconds for $A2$ (with 30-pixel radius seed size) , 248 seconds for $A3$ (with 30-pixel radius seed size) and 12.8 seconds for the proposed method (without the detection and VB separation parts). It should be noted that the all results are obtained until each method reaches its possible convergence stage. The results show that the proposed method is robust under various noise levels as well as faster than other famous alternatives. The initialization effect is also validated in this experiments. It should be noted that $A1-A3$ need perfect manual initializations. However, the method is almost independent of the initialization (which is usually required in the registration step). The segmentation results and the accuracy on the ESP (when the initialization is not optimal) are shown in Figure59 and Figure61, respectively. In this figures, the initial point is chosen not close to the center point of the object of interest. It's clear that the proposed method performance is almost constant with different initial points. On the contrary, the alternative methods are severely suffering from performance degradation.

The effect of each model is validated as shown in Figure62. In the figure, the results which are based on ii) only the intensity model, iii) intensity and spatial interaction, iv) intensity, spatial interaction, and shape models are shown. The intensity based approach is not robust under various noise levels. After the spatial interaction model is used, the segmentation is getting better and most of the noise is eliminated. However, there are still missing information and some noise using the two models. With the proposed approach much better results are obtained compared with other models. The segmentation accuracy with respect to the various noise levels is shown in Figure 63.

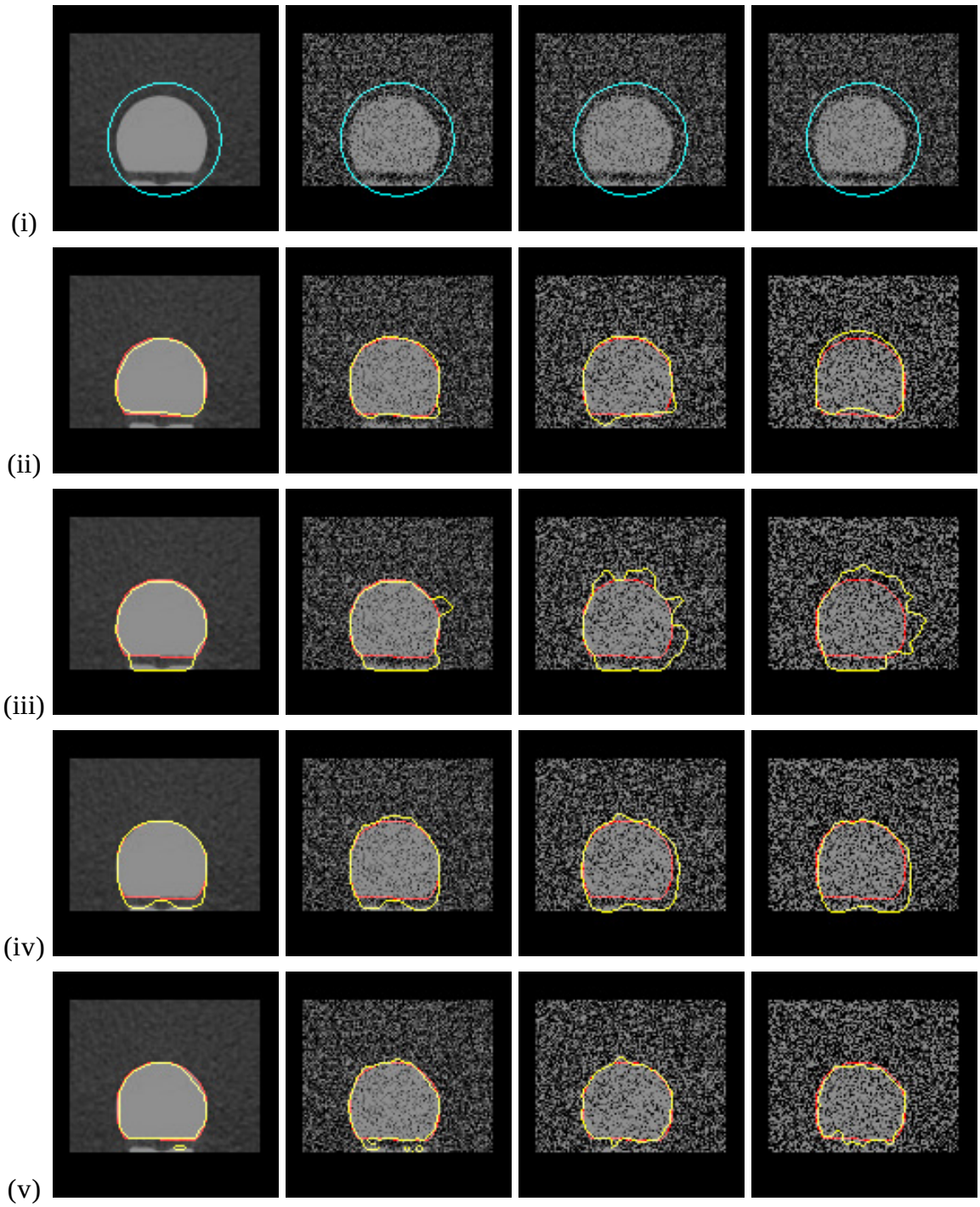

FIGURE 58 – Good Initialization: Segmentation comparison under (a) no noise, noise variances (b) σ_n^2=0.1, (c) σ_n^2=0.25, and (d) σ_n^2=0.5. (i) Initialization. The results of (ii) $A1$, (iii) $A2$, (iv) $A3$ and (v) the proposed method. (The red and yellow colors show the contour of the ground truths and segmented regions, respectively.)

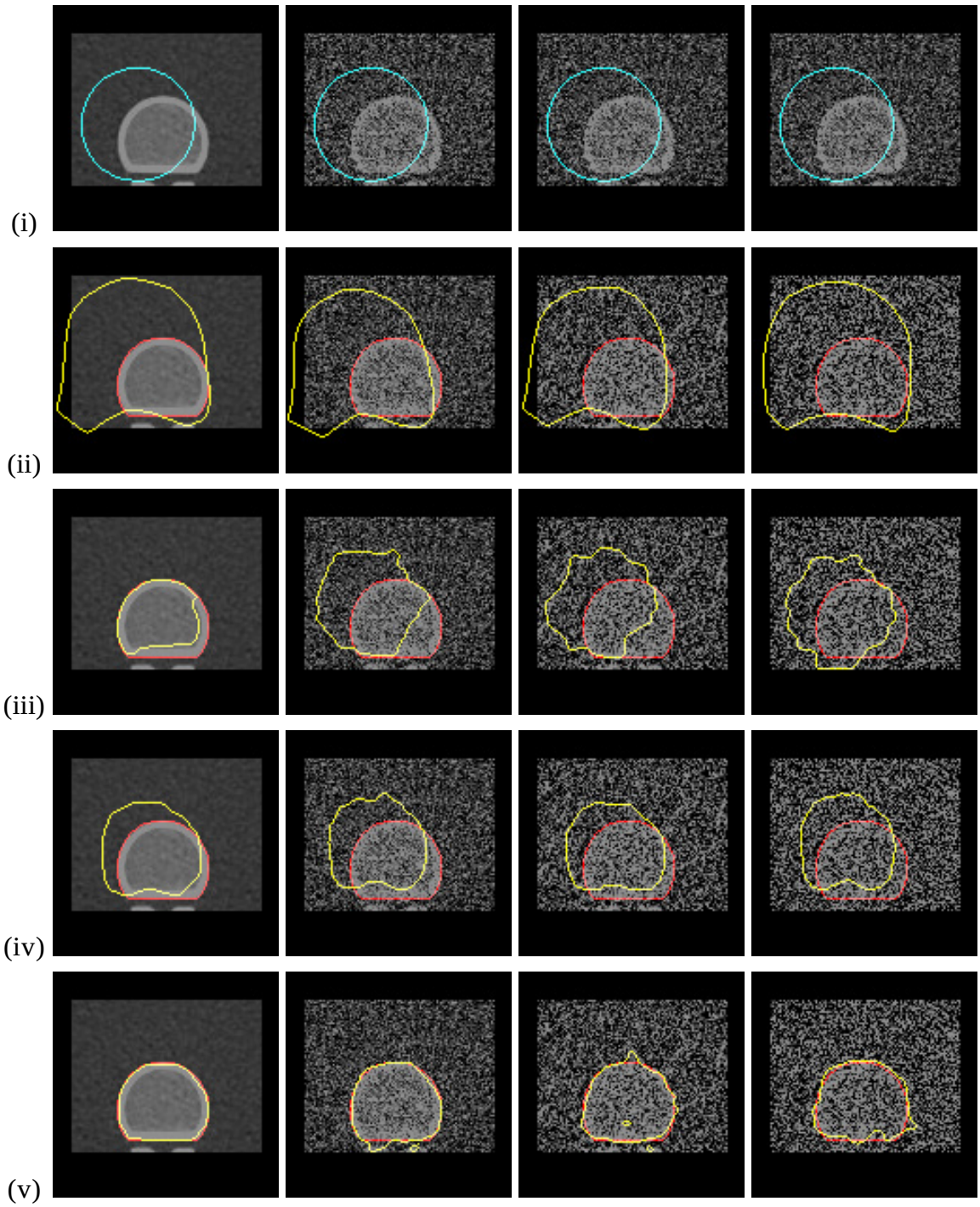

FIGURE 59 – Worse Initialization: Segmentation comparison under (a) no noise, noise variances (b) σ_n^2=0.1, (c) σ_n^2=0.25, and (d) σ_n^2=0.5. (i) Initialization. The results of (ii) $A1$, (iii) $A2$, (iv) $A3$ and (v) the proposed method. (The red and yellow colors show the contour of the ground truths and segmented regions, respectively.)

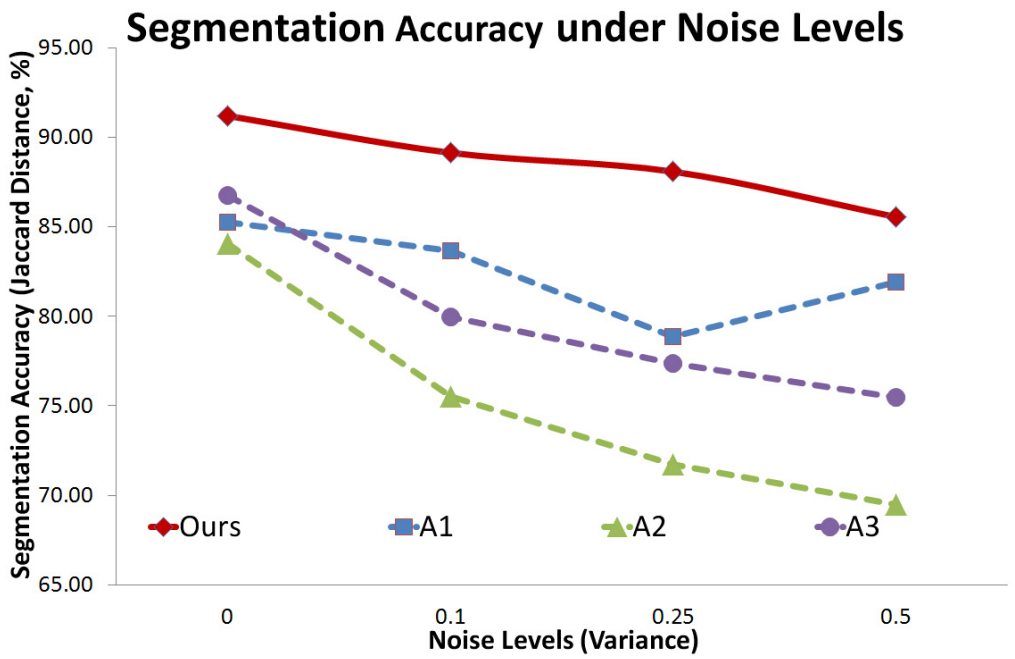

FIGURE 60 – Average segmentation accuracy of the VB segmentation on 12 CT images (ESP) with respect to the various noise levels.

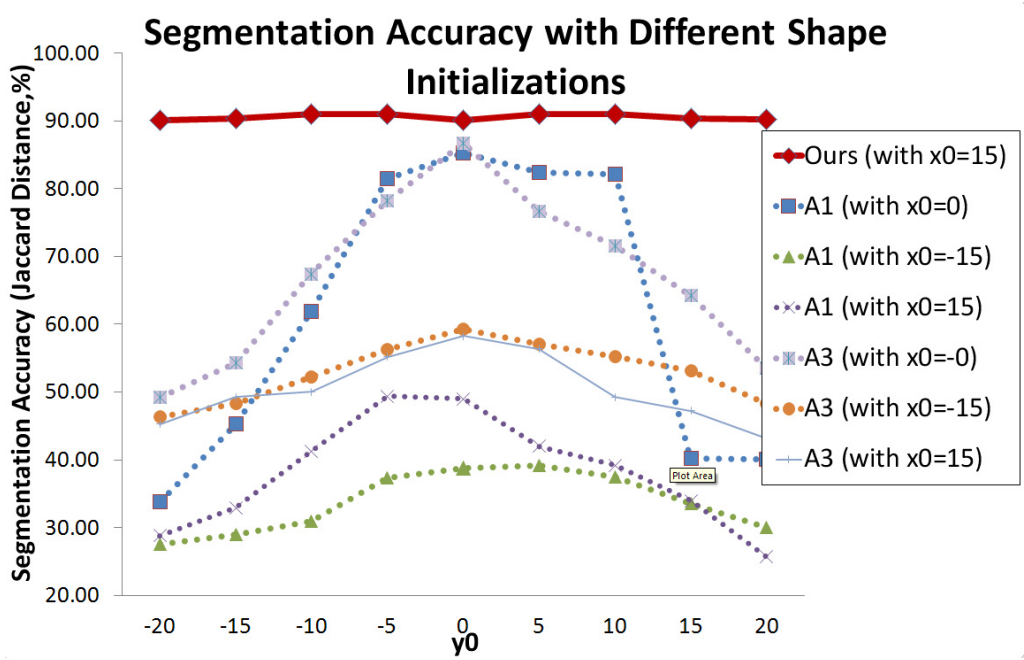

FIGURE 61 – The effect of the initialization on the segmentation accuracy of 12 CT images (ESP) using $A1$, $A3$, and the proposed. x_0 and y_0 represent the initial point in the X-direction and Y-direction respectively w.r.t the center of the object.

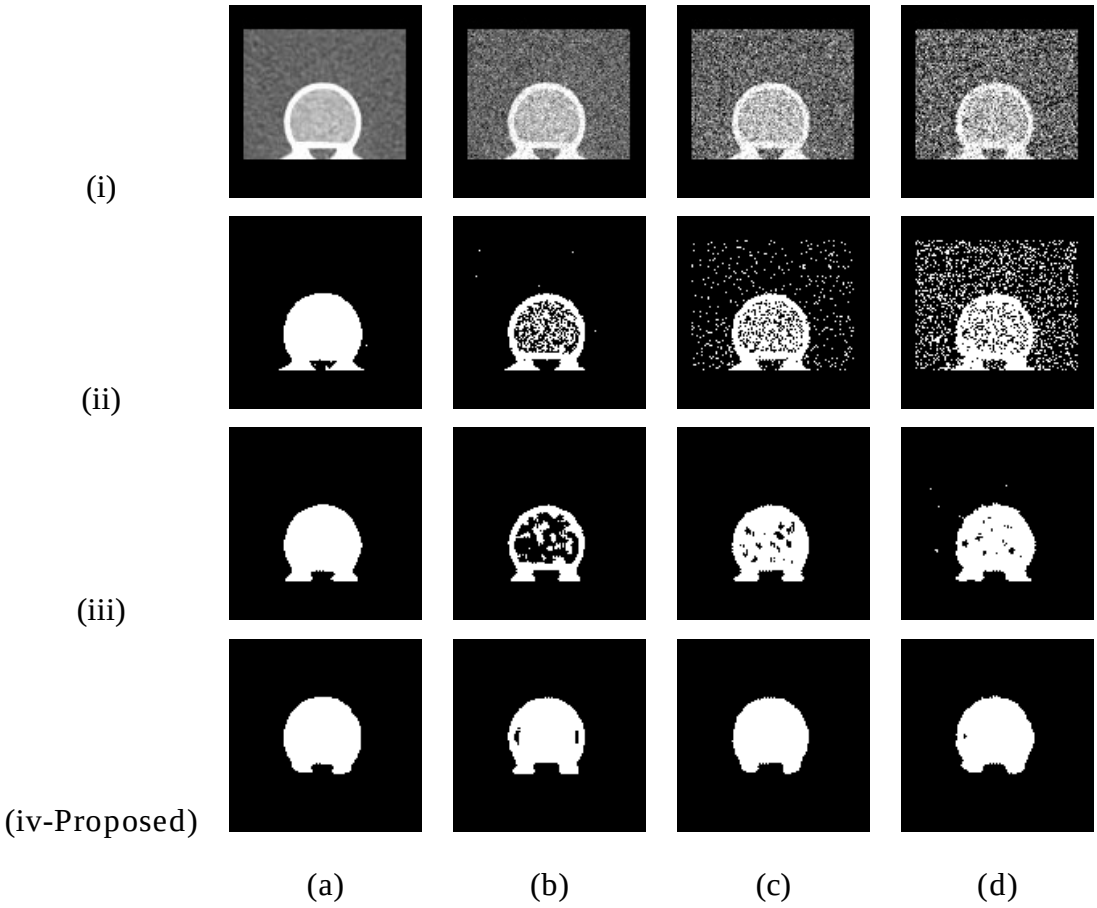

FIGURE 62 – Segmentation results of an ESP CT slice with (a) no noise, noise variances (b) σ_n^2=0.1, (c) σ_n^2=0.25, and (d) σ_n^2=0.5. (i) The original gray level image with various noise levels. The results of (ii) only the intensity based segmentation, (iii) the initial segmentation $\mathbf{f}^*$ based on the intensity and spatial interaction models, (iv) proposed method integrating three models (intensity, interaction, and shape).

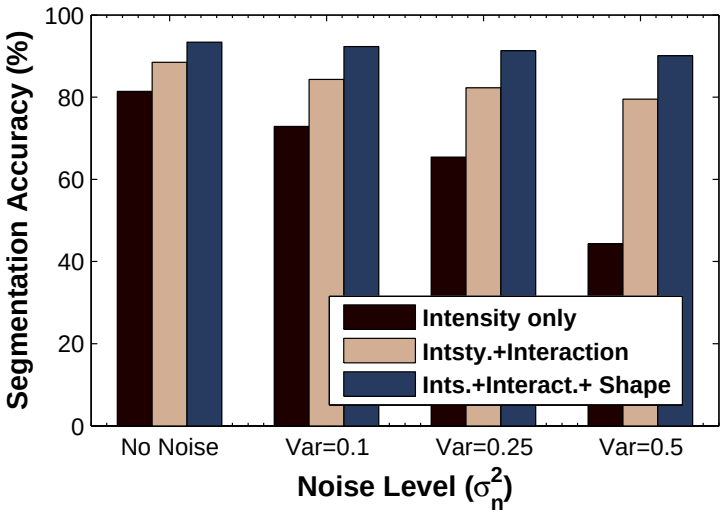

FIGURE 63 – Average segmentation accuracy of the VB segmentation method on 12 ESP CT images . The size of each image is 512x512. (After each VB is detected, the size is reduced to 120x120).

4. Results on Clinical CT Images

In this study, different type of data sets are used. Classification of data sets are categorized into three groups as shown in Table 2. Classification is based on 6 features. Slice thickness, resolution, spine column region (shape), fractures, diseases, and spine bone edges are main factors of the classification. Class A is the best data sets which can be segmented and analyzed easily. Data sets which are classified in class C have serious problems such as diseases, fractures, weak spine edges, and low resolution. Data sets in class B have some problems but they are better than data sets in class C. Categorization could help to analyze the results separately.

As mentioned above, the proposed algorithm is tested on 932 CT slices / 66 VBs which are obtained from 18 (7 H and 11 L) different patients and different spine bone regions (i.e. lumbar, thoracic, and etc.). The segmentation accuracy is given with respect to the health condition of bone ('H', 'L', and 'H+L'), and the classification criteria (Class A, B, and C). Table 3 shows the quality measurement results of the proposed segmentation method. The four different measurements are given to be judged fairly.

As can be interpreted from the results in the table, the Jaccard coefficient gives the lowest quality score respect to the others. Also, the accuracy gives the highest quality score respect to the other measurements. By using this information, the proposed segmentation reaches the scores of 'Jaccard coefficient' 87.6%, 83.0%, and 85.0% for 'H', 'L', and 'H+L', respectively. The same measurements gives 87.7%, 86.9%, and 80.3% for classes A, B, and C, respectively. The proposed method reaches the scores of 'accuracy' measurement 98.2%, 97.9%, and 97.6% for 'H', 'L', and 'H+L', respectively. The same measurements gives 99.0%, 98.7%, and 98.0% for classes A, B, and C, respectively.

Figure 64 shows the shape model registration and final segmentation result on end-plate slices of VBs. The proposed method is able to segment end-plate slices

TABLE 2
CLASSIFICATION OF CLINICAL DATA SETS USED IN THE EXPERIMENTS: THERE ARE TOTALLY 18 DATA SETS IN THE DATA BASE. CLASS A, B, AND C HAVE 7, 5, AND 6 DATA SETS, RESPECTIVELY.

	Class A	**Class B**	**Class C**
Slice thickness	Usually <2.5mm	Usually ≥2.5mm, but may be <2.5mm	Usually≥3.00mm, but can be smaller if disease exists
Resolution	High	Usually low	Lower
Shape	Straight	Straight / Curvy	Usually curvy but it can be straight
Bone degeneration or osteophyte	No	May have disease	May have disease
Fracture	No	No serious fracture	May have serious fractures
Edge	Strong	Strong / Weak	Usually weak
Note:	Optimum data	This class has some problems	This class has very serious problems

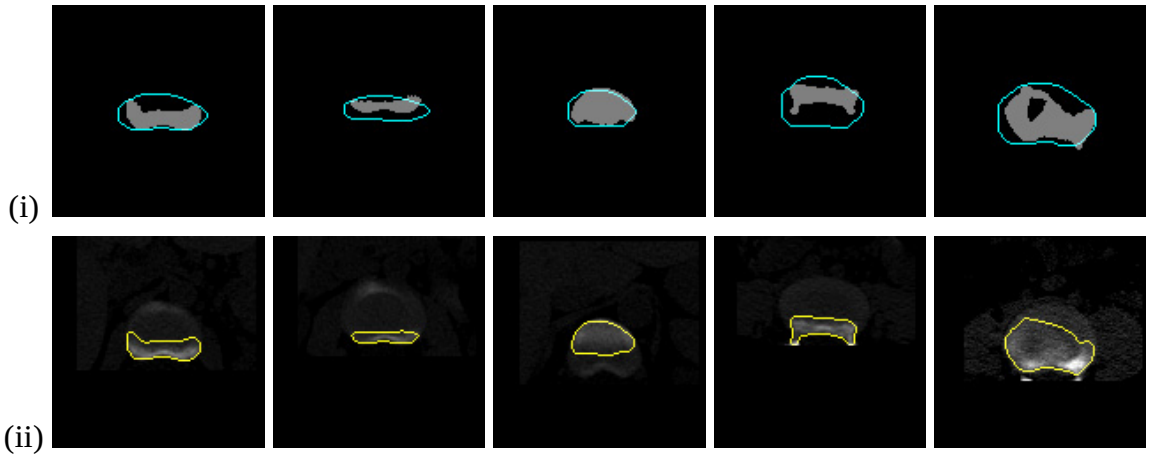

FIGURE 64 – The shape registration process and segmentation results of end-plate slices of VBs. (i) The shape model is registered to the initial segmented region. The blue color shows the contour of the registered variability region, **J**. (ii) Final segmentation results. The yellow color shows the contour of the segmented region.

thanks to the shape embedding process although the shape model is obtained using the full view of VB slices. The unnecessary regions such as ribs and processes are extracted as much as possible using the shape model. Figure 65 shows some of the segmentation examples in axial view.

It should be noted that VBs were manually separated in this test. The framework take 167.2 seconds (less than three minutes) to segment 12 VBs. It should be noted that the number of slices affects the execution time. For the 2D/3D frame-

TABLE 3
SEGMENTATION RESULTS OF EACH DATA CLASS BASED ON DIFFERENT MEASURES. (THE MEASUREMENTS ARE BASED ON DATA SETS WITH $120\mathbf{x}120\mathbf{x}Z$ SIZE WHERE Z REPRESENTS NUMBER OF SLICES.)

	'H'	'L'	'H+L'	Class A	Class B	Class C
Accuracy,%	98.2	97.9	97.6	99.0	98.7	98.0
Precision,%	91.1	86.6	88.6	90.9	89.9	84.4
Jaccard coefficient,%	87.6	83.0	85.0	87.7	86.9	80.3
Dice's coefficient,%	93.1	90.4	91.5	93.8	92.9	89.0

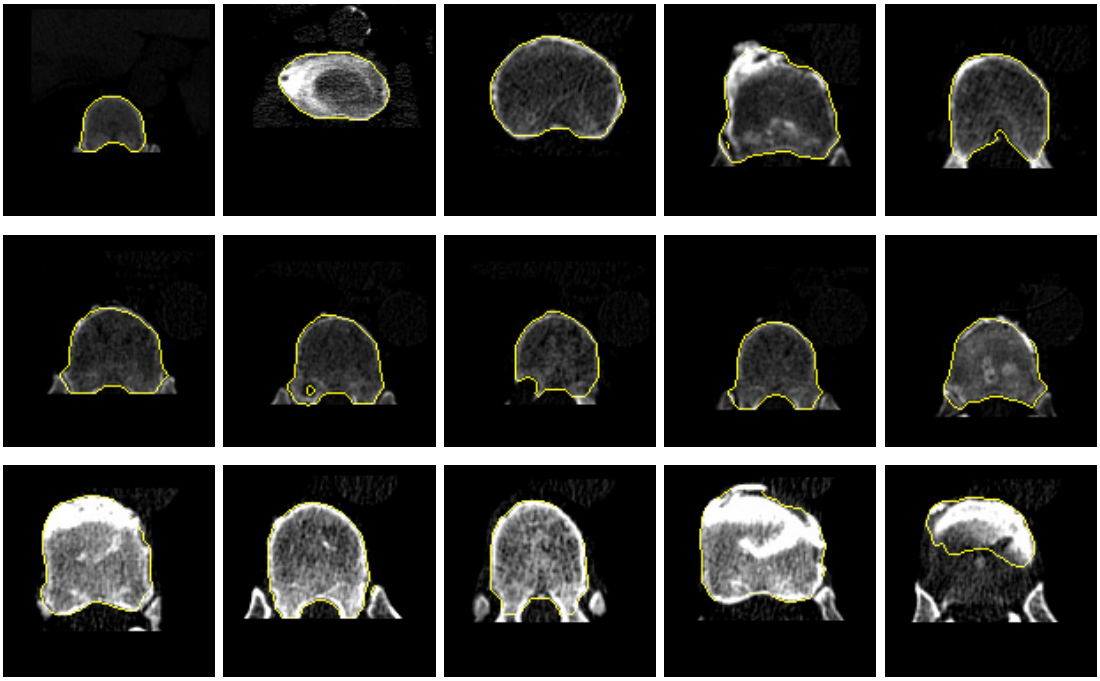

FIGURE 65 – Some of segmentation results are shown in the axial view. The yellow color shows the contour of the segmented region.

TABLE 4
RELATIVE COMPARISON

	$F1$	$F2$	$F3$	$F4$	$F5$	$F6$
[36]	No	> 36.5	No	Yes	All	No
[51]	Yes	> 36	Yes	No	Specific	Yes
Proposed	Optional	< 3	Yes	No	All	No

work, the execution time is related to the number of slices in the image. Some experimental images of 3D results are shown on coronal and sagittal views in Figure 69.

The proposed framework is compared with two of very important spinal bone related publications using features of each method. The features can be described as follows: $F1$: User interactions, $F2$: Execution time (minutes) to run all steps respect to segment 12VBs, $F3$: Extraction of spinal processes, $F4$: Vertebra identification, $F5$: Suitability to all or specific location of spinal column (such as thorocic, lumbar, and etc.), $F6$: The BMD measurements. Since the direct compar-

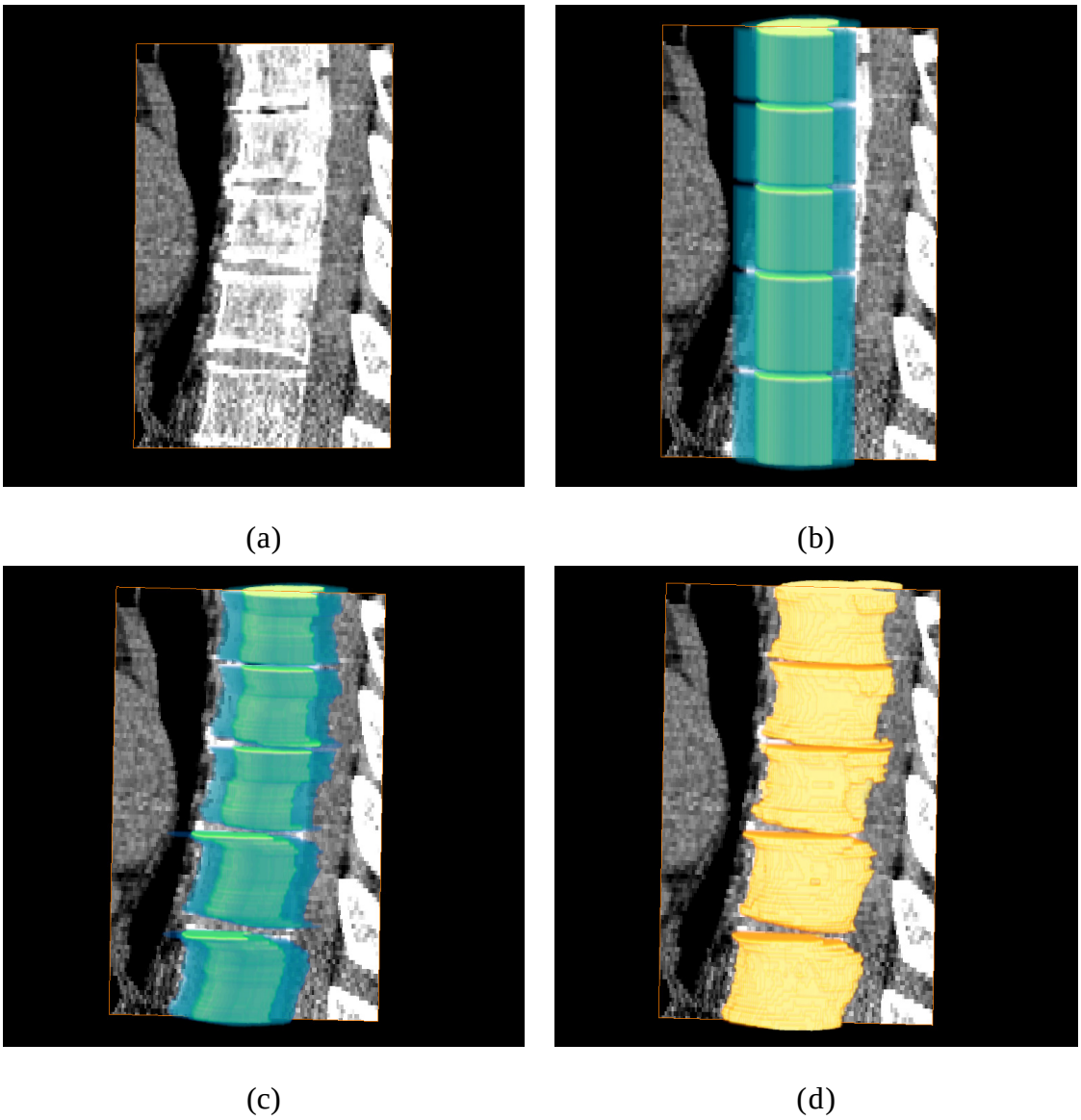

FIGURE 66 – The shape embedding and final segmentation results are shown in 3D views. (a) A CT data is shown in the sagittal axis (without the refinement). (b) The initial location of the shape models. 2D shape models are propagated in z-axis to form 3D models. The blue color (outer volume) shows the variability region, whereas the yellow color (inner volume) represents the object region. (c) The shape model after registration. (d) The final segmentation results using the three models.

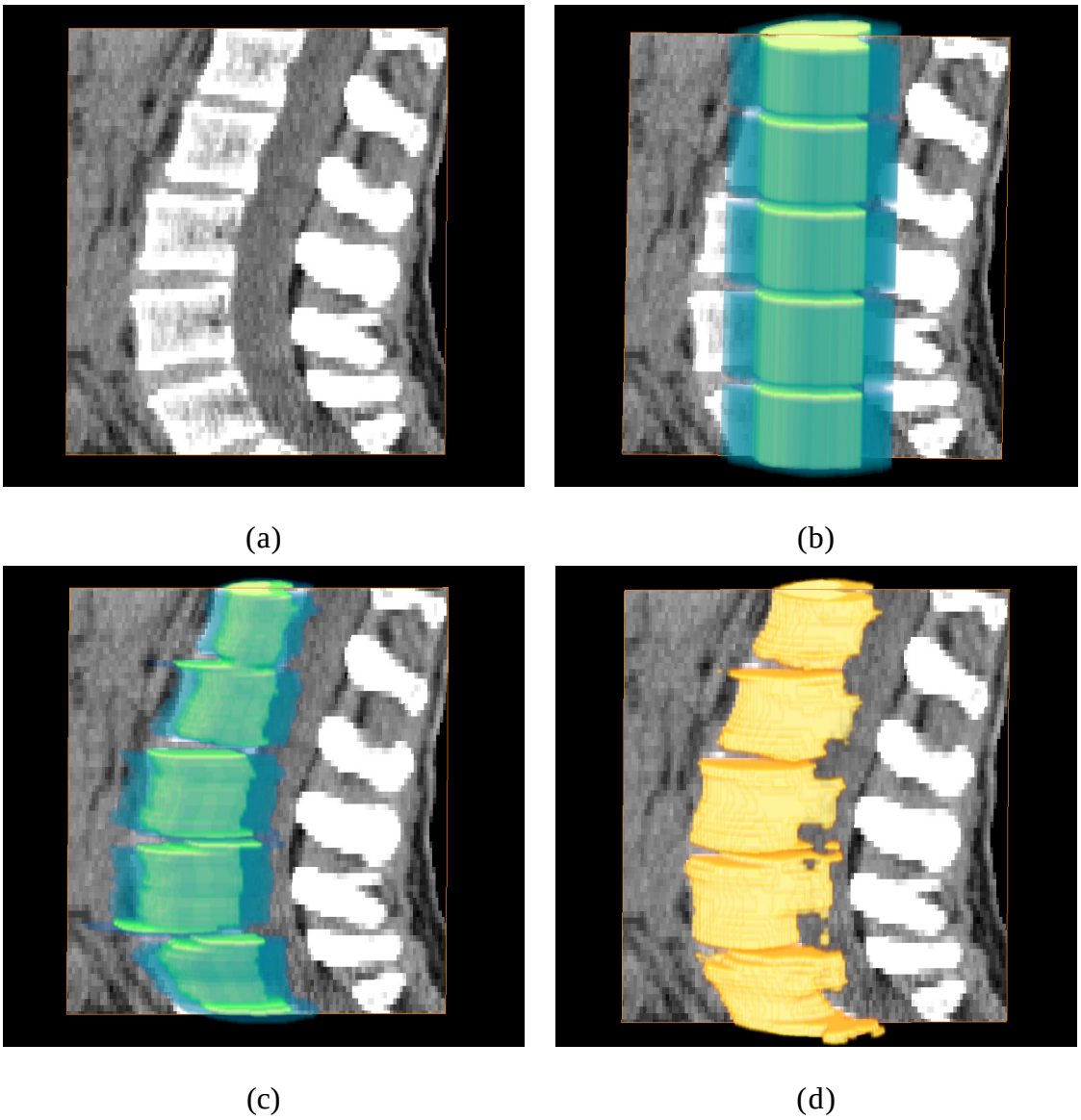

FIGURE 67 – The shape embedding and final segmentation results are shown in 3D views. (a) A CT data is shown in the sagittal axis (without the refinement). (b) The initial location of the shape models. 2D shape models are propagated in z-axis to form 3D models. The blue color (outer volume) shows the variability region, whereas the yellow color (inner volume) represents the object region. (c) The shape model after registration. (d) The final segmentation results using the three models.

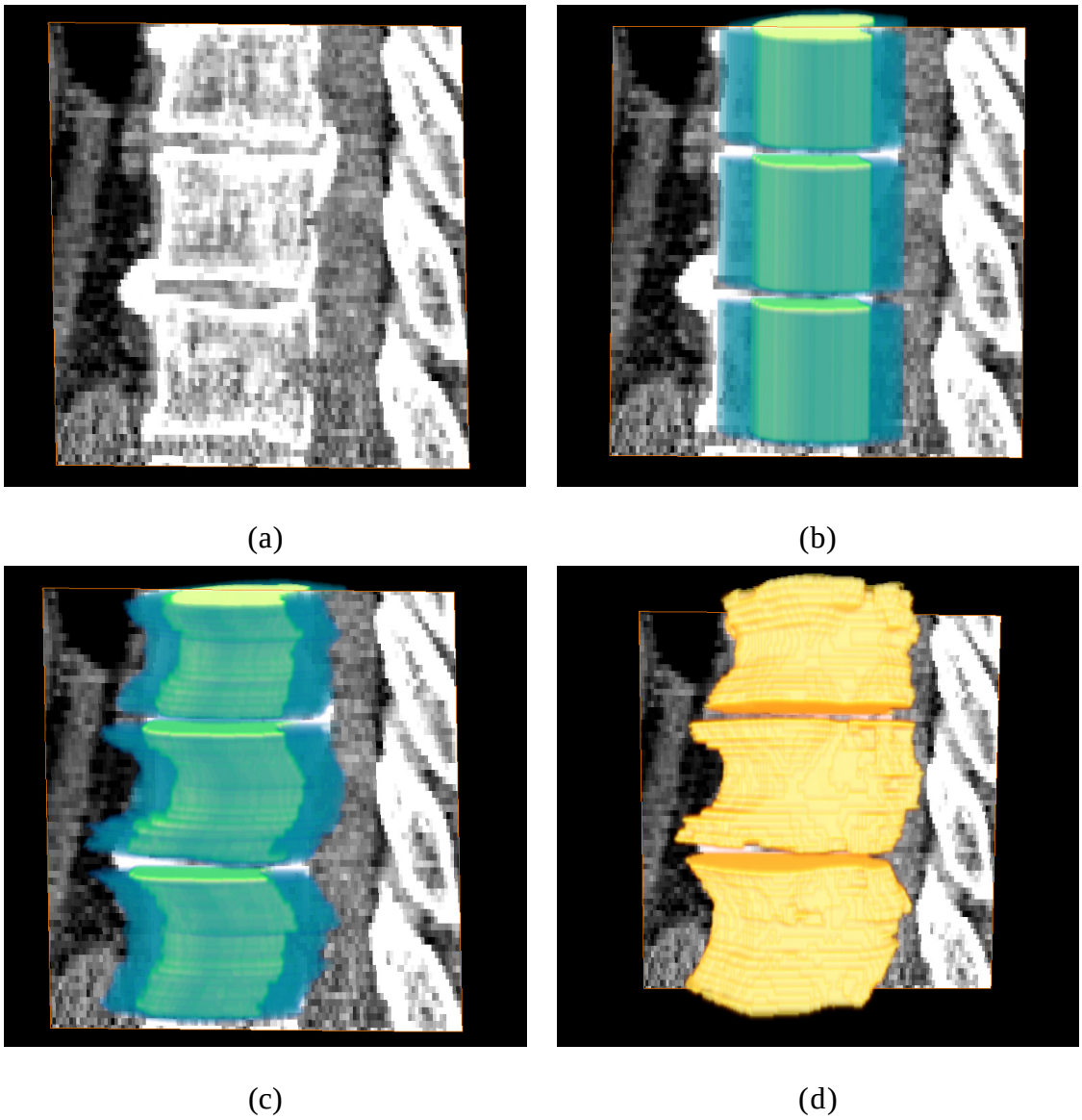

FIGURE 68 – The shape embedding and final segmentation results are shown in 3D views. (a) A CT data is shown in the sagittal axis (without the refinement). (b) The initial location of the shape models. 2D shape models are propagated in z-axis to form 3D models. The blue color (outer volume) shows the variability region, whereas the yellow color (inner volume) represents the object region. (c) The shape model after registration. (d) The final segmentation results using the three models.

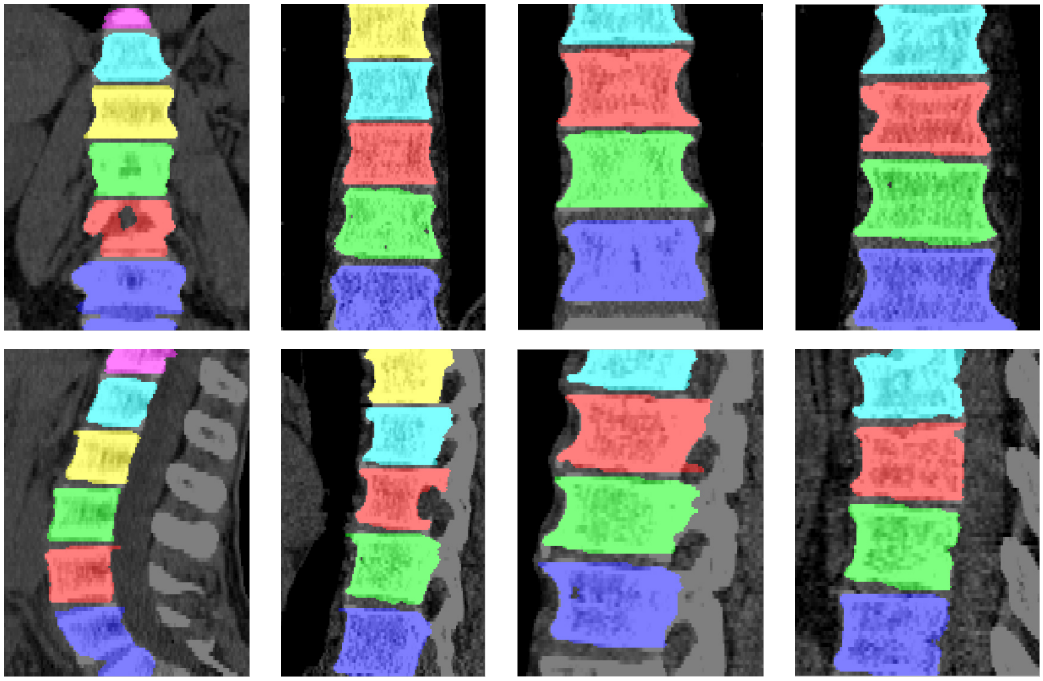

FIGURE 69 – Some segmentation results examples on coronal (the first row) and sagittal (the second row) views of 3D segmentation.

TABLE 5
AVERAGE EXECUTION TIME OF THE FRAMEWORK: THE AVERAGE TIME CALCULATION IS BASED ON 12 VBS / 96 CT SLICES.)

Framework Stages	**Execution Time, secs.**
Spinal Cord Extraction	15.7
VB Separation	18 (manual) / 45 (automatic)
Initial Segmentation	54.1
Shape Registration	32.6
Final Segmentation	46.8
Total	167.2 (*when manual VB separation is considered*)

TABLE 6
COMPARISON OF TWO PROPOSED METHODS DESCRIBED IN CHAPTER 2 AND 3

Features	**Chapter 2**	**Chapter 3**
Application	Generic	Only the VB region
Shape coefficients	Yes	No
Shape registration process	Iterative	Direct
Dice's Coefficient	93.1%	91.5%
Average execution time (min / 96 Ct slices)	~ 9 minutes	~ 3 minutes

ison with these two methods are very difficult, each feature is compared as shown in Table 4. Although the results are obtained using difference computer system for each method, the most important contribution of this work is to segment VBs in very low execution times with the acceptable segmentation accuracy. This dissertation claims that the proposed method can be applied in real time clinical studies. Table 6 shows the comparison of two proposed methods described in Chapters 2 and 3.

H. Discussion and Conclusion

In this work, a framework which is robust under segmentation challenges, appropriate for a clinical workflow, and has theoretical novelty is proposed. This work is validated with various noise levels and compared with three alternative methods. The segmentation quality is measured on controlled data sets (classified as 'H', 'L', Class A, Class B, and Class C). To transfer the developed software into the clinical usage, more experiments on much more data sets are necessary.

One of the most important contributions of this study is to offer a segmentation framework which can be suitable to the clinical works with acceptable results. The proposed method completes the VB segmentation in very low execution time.

It should be noted that any parallel programming or graphical acceleration option were not used in this work. However, if needed, the execution time can be reduced using such methods.

The gradient descent method to minimize the energy formulation is mostly used in the shape registration algorithms. However, this method is dependent on the initialization and it takes much longer to execute. Also, there are other possible registration methods such as procrustes algorithm, which is fast; however, it needs manual or automatic control points. In this dissertation, a faster shape registration method is used. The registration step is done slice by slice, hence the shape model can deform independently in 3D data sets. This approach gives deformation flexibility between slices. 3D shape registration was refrained to avoid the higher execution time since the rotation parameters should be estimated in 3D case.

Some shape models have weighting coefficients such as in [5, 14]. Using the shape coefficients, the shape model can be dynamically updated during the shape registration and segmentation optimization process. However, updating the shape weighting coefficients adds very high execution time which may not be accepted in clinical applications. In the proposed method, each training shape affects equally to form the shape model. Also, it should be noted that the end-plate slices are segmented successfully thanks to the shape registration process although the shape model is obtained using in-plane slices.

The final segmentation is done using the iterated conditional modes. A new shape constraint is added to the conventional ICM method to enhance the results. The implementation is fast and not dependent on the tuning the parameters of the spatial interaction. In some cases, small portions of spinal processes and ribs are segmented erroneously. Future work can be including to investigate to reduce the misclassifications.

Possible works to estimate how the segmentation quality affect the BMD measurements and fracture analysis can be analyzed. To assist the VB fracture

analysis, an automated point correspondence detection algorithm, such as scale-invariant feature transform (SIFT), can be tested to detect the VB height changes. In this problem, the corresponding points on the same patient, which is scanned at specific time intervals, should be detected successfully.

CHAPTER IV

EXTENSION STUDY OF SEGMENTATION USING GRAPH CUTS

In this chapter, an extension study of previously published [55] shape based graph cuts method is described. In [55], the probabilistic shape model was assumed to be registered in advance the segmentation process. In this chapter, the probabilistic shape model is automatically embedded to the image domain as proposed in [34].

The proposed framework has five phases: i) Shape model reconstruction, ii) the detection of the VB using the Matched filter, iii) initial segmentation using the intensity and spatial interaction models, iv) the registration of the shape prior and initially segmented image by matching a vector distance function (VDF), and v) final segmentation using graph cuts which integrates intensity, spatial interaction and shape prior. Figure 70 shows effects of each model on the segmentation.

A. Method

In this work, a 3D shape based segmentation method is proposed. To use the shape prior in the segmentation process, $\mathbf{I}$ and the shape prior are needed to be registered, as will be explained in section IV.A.2. Let $\mathbf{d}$ represent the probabilistic shape model. It should be noted that the shape model is obtained using training images registered to the ESP which can be represented as $\mathbf{J}$. In the registration process, $\mathbf{J}$ and $\mathbf{I}$ will be the source and target information, respectively. In this method, the objective is to find the desired labeling, $\mathbf{f}$ using the transformation matrix, $\mathbf{T}$. The overall segmentation framework is given in Algorithm 1. Figure 71 shows the steps of the proposed framework. There are two stages: training (offline)

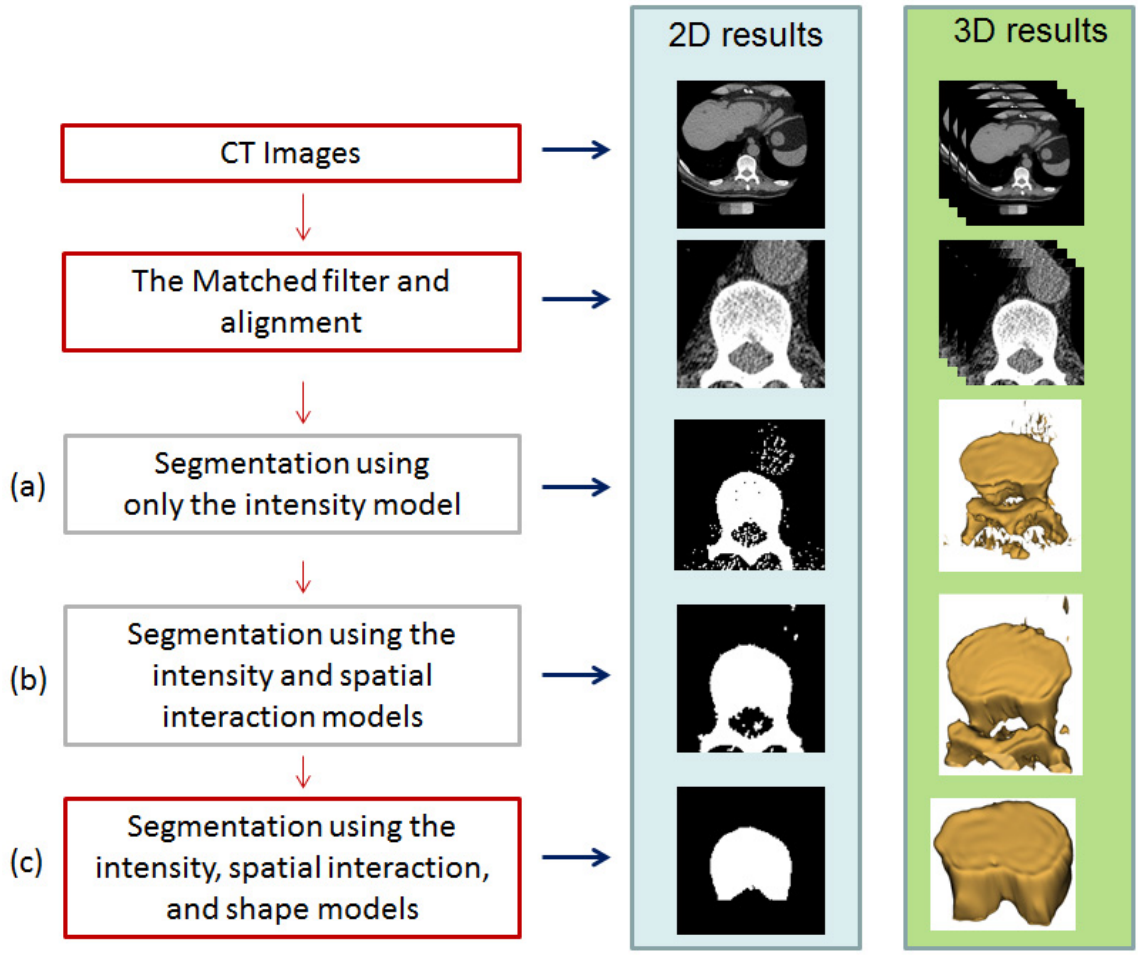

FIGURE 70 – Effects of each information is shown in 2D / 3D example. The Matched filter is employed to detect the VB region. (a) The segmentation result if only the intensity model is used. (b) The segmentation result if the intensity and spatial interaction models are used. (c) The segmentation result if the intensity, spatial interaction, and shape models are used. This is the proposed framework.

and testing (online) stages as described below.

Algorithm 4 Proposed framework

$Given$: The input image ($\mathbf{I}$ as the target information), the ESP ($\mathbf{J}$ as a source information), the probabilistic 3D shape model ($\mathbf{d}$).

$Objective$: To obtain the desired labeling ($\mathbf{f}$) using the required transformation matrix ($\mathbf{T}$).

0. Obtain the probabilistic shape model (offline).

1. The automatic detection of the VB region using the Matched filter.

2. Obtain the initial segmentation using graph cuts which integrates the intensity and spatial interaction models.

3. Register the shape prior to the initially segmented image by matching the VDF.

4. Final segmentation using graph cuts which integrates the intensity, spatial interaction, and shape prior models.

a. 3D Shape Model Construction (Offline): The 3D shape model of the VB is obtained from a training set of CT data. First, VBs are manually segmented (under supervision an expert). Then the segmented VBs are aligned using 2D registration. The aligned training images are shown in Figure 72. Finally, a shape volume represented as $\mathcal{P}_s = \mathcal{O} \bigcup \mathcal{B} \bigcup \mathcal{V}$ is generated. The white color represents the object or the VB ($\mathcal{O}$), the black color represents the background ($\mathcal{B}$), and the gray color represents the variability volume ($\mathcal{V}$). Some example views of 3D shape prior ($\mathcal{P}_s$) are shown in Figure 73. Algorithm 5 lists the steps of the probabilistic shape model reconstruction.

To model the shape variations in the variability volume $\mathcal{V}$, the distance probabilistic model is used. The distance probabilistic model describes the object (and background) in the variability volume as a function of the normal distance $d_p = min\|p - c\|$ (where $c \in \mathbf{C}_{\mathcal{OV}}$) from a pixel $p \in \mathcal{V}$ to the VB/variability surface $\mathbf{C}_{\mathcal{OV}}$. Each set of pixels located at an equal distance d_p from $\mathbf{C}_{\mathcal{OV}}$ constitutes an iso-surface $\mathbf{C}_{d_p}$ for $\mathbf{C}_{\mathcal{OV}}$. To estimate the marginal density of the VB, it is assumed

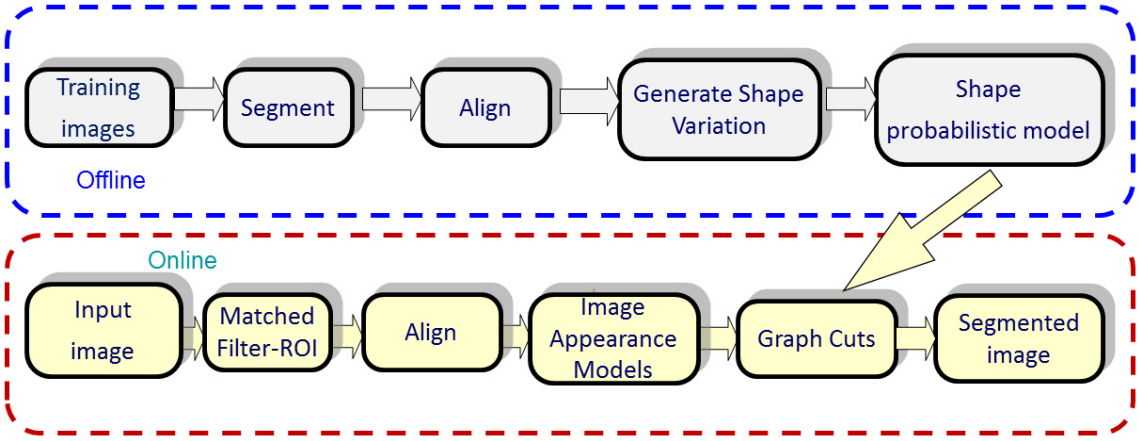

FIGURE 71 – Segmentation framework. There are two parts: Offline stage is the training step to obtain the 3D shape prior and probabilistic model. Online stage is the testing step to segment a clinical CT data.

Algorithm 5 Probabilistic 3D Shape Model Reconstruction (More Detailed)

1. Segment training images manually.

2. Align segmented images as described in the previous chapters.

3. Generate the shape volume $\mathcal{P}_s = \mathcal{O} \bigcup \mathcal{B} \bigcup \mathcal{V}$. $\mathcal{O}$ represents the object volume, $\mathcal{V}$ represents the variability volume, and $\mathcal{B}$ represents the background volume.

4. Generate the distance probabilistic model in $\mathcal{V}$.

$4.(a)$ Obtain the VB / variability surface $\mathbf{C}_{\mathcal{OV}}$ which corresponds to the outer surface of the object volume, $\mathcal{O}$.

$4.(b)$ Obtain iso-surfaces, $\mathbf{C}_{d_p}$, in $\mathcal{V}$ as a function of the normal distance $d_p = min\|p - c\|$ (where $c \in \mathbf{C}_{\mathcal{OV}}$) from a pixel $p \in \mathcal{V}$ to the VB / variability surface $\mathbf{C}_{\mathcal{OV}}$. There are several iso-surfaces located at an equal distance d_p from $\mathbf{C}_{\mathcal{OV}}$.

$4.(c)$ Obtain the probability of an iso-surface to be the object. This step is done by counting the number of object pixels of training set on each iso-surface (Follow Eqs. 70-72).

$4.(d)$ Obtain the probability of an iso-surface to be the background. This step is done by counting the number of background pixels of training set on each iso-surface (Follow Eqs. 73-75).

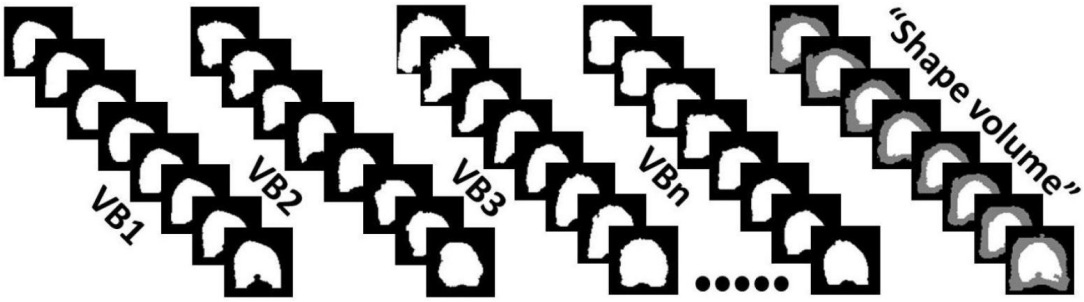

FIGURE 72 – Obtaining the shape prior volume. {VB1,...,VBn} training CT slices of different data sets. (n represents the number of training data). The last column shows the shape prior slices with variability volume.

that each iso-surface $\mathbf{C}_{d_p}$ is a normally propagated wave from $\mathbf{C}_{\mathcal{OV}}$ as shown in Figure 74. The probability of an iso-surface to be an object decays exponentially as the discrete d_p increases. The VB distance histogram is estimated as follows. The histogram entity of the object region at distance d_p is defined as

$$h(d_p \mid \mathcal{O}) = \sum_{i=1}^{M} \sum_{\ell=1}^{K} \sum_{p \in \mathbf{C}_{d_p}} \delta(p \in \mathcal{O}_{i\ell}) \tag{70}$$

where the indicator function $\delta(\mathcal{A})$ equals 1 when the condition $\mathcal{A}$ is true, and zero otherwise, M is the number of training data sets, K is the number of CT slices of each data set, and $\mathcal{O}_{i\ell}$ is the VB volume. The distance, d_p, is changed until the whole distance domain in the variability volume is covered. In pixel wise, this process can be done by obtaining the outer edge of the previous iso-surface. Then, the histogram is multiplied with shape prior value which is defined as follows:

$$\pi_{\mathcal{O}} = \frac{1}{M|\mathcal{V}|} \sum_{p \in \mathcal{V}} \delta(p \in \mathcal{O}). \tag{71}$$

The distance marginal density of the object region is calculated as

$$p(d_p \mid f_p = 1) = \frac{h(d_p \mid \mathcal{O})\, \pi_{\mathcal{O}}}{M|\mathbf{C}_{d_p}|}. \tag{72}$$

The same scenario is repeated to obtain the marginal density of the background. The histogram entity of the background region at distance d_p is defined

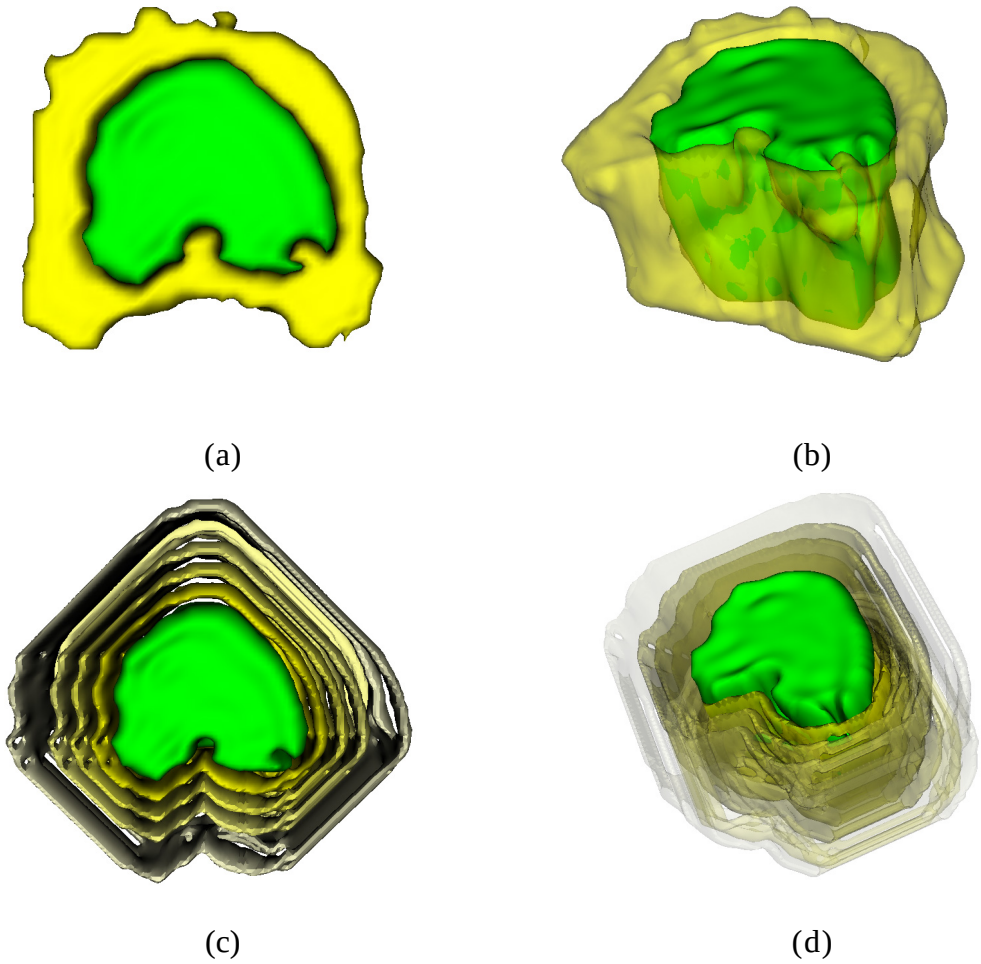

FIGURE 73 – Views of the 3D shape prior. The inner volume (the green color) shows the object volume $\mathcal{O}$, the outer volume (the yellow color) shows the variability volume $\mathcal{V}$. In (c) and (d) the variability volume is represented with several iso-surfaces.

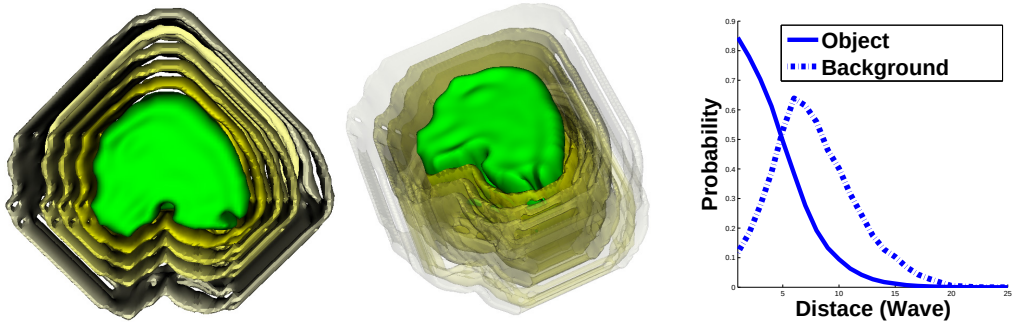

(a) (b) (c)

FIGURE 74 – (a-b) The 3D shape prior with object (the green color) and variability (iso-surfaces) volume. The green color represents the object volume, $\mathcal{O}$, the surface of the object volume represents the object / variability surface, $\mathbf{C}_{\mathcal{OV}}$, the waves represent the iso-surfaces, $\mathbf{C}_{d_p}$. (c) The probability of the object and background in the variability volume, $\mathcal{V}$, respect to each iso-surface, $\mathbf{C}_{d_p}$.

as

$$h(d_p \mid \mathcal{B}) = \sum_{i=1}^{M} \sum_{\ell=1}^{K} \sum_{p \in \mathbf{C}_{d_p}} \delta(p \in \mathcal{B}_{i\ell}) \tag{73}$$

where $\mathcal{B}_{i\ell}$ is the background region. Then, the histogram is multiplied with shape prior value which is defined as follows:

$$\pi_{\mathcal{B}} = \frac{1}{M|\mathcal{V}|} \sum_{p \in \mathcal{V}} \delta(p \in \mathcal{B}). \tag{74}$$

The distance marginal density of the background region is calculated as

$$p(d_p \mid f_p = 0) = \frac{h(d_p \mid \mathcal{B})\, \pi_{\mathcal{B}}}{M|\mathbf{C}_{d_p}|}. \tag{75}$$

An example of the distance marginal densities of the object and background region is shown in Figure 74 (c). The next section explains the testing segmentation stage.

1. Initial Segmentation

In the first step of the segmentation, the Matched filter [64] is employed to detect the VB region automatically. To estimate the initial labeling $\mathbf{f}^*$, the graph

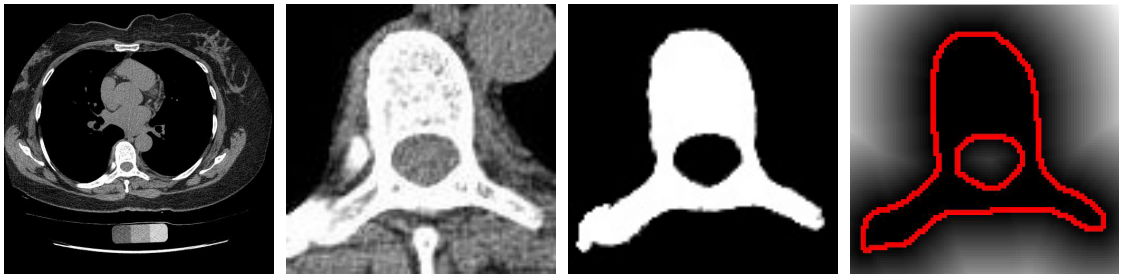

(a) (b) (c) (d)

FIGURE 75 – An example of the initial labeling. (a) Original CT image, (b) detection of the VB region, (c) the initial labeling, $\mathbf{f}^*$, and (d) the VDF of the initial segmentation which is used in the registration phase ($\Phi_{\mathbf{I}}$). Red color shows the zero level contour.

cuts which integrates the linear combination of gaussian (LCG) and MGRF model is used. The same method described in section IV.A.3 is used. It should be noted that the shape model is not used in this process. Initially segmented region is used to obtain the VDF which is required in the registration process. An example of the initial labeling is shown in Fig 75.

2. Variational Registration Approach

A vector distance function is used to represent contour and surfaces. In this section, the 2D transformation is discussed as the general case. The transformation has five parameters such as s_x, s_y (for scale, $\mathbf{S}$), θ (for rotation, $\mathbf{R}$), and t_x, t_y (for translation, $\mathbf{Tr}$). Let us define the result by β that is obtained by applying a transformation $\mathbf{A}$ to a given contour/surface α. In this study, β and α correspond to $\mathbf{I}$ and $\mathbf{J}$, respectively. The transformation can be written for any point $\mathbf{x}$ in the space as $\mathbf{X} = \mathbf{SRx} + \mathbf{Tr}$. Assume that applying the transformation to the given point results in the pair of points $\widehat{\mathbf{x}}, \widehat{\mathbf{x}}_0 \in \Omega_{\mathbf{I}}$. Then it can be shown that

$$\Phi_{\mathbf{I}}(\mathbf{X}) = \mathbf{SR}(\mathbf{x}_0 - \mathbf{x}) = \mathbf{SR}\Phi_{\mathbf{J}}(\mathbf{x}). \tag{76}$$

Since the vector representation is invariant to translation, the new vector can be obtained using rotation and scaling parameters.

The objective is to find the global transformation between the two given images $\mathbf{J}$ and $\mathbf{I}$ minimizing a certain energy function based on some dissimilarity

measure. The objective is to find a transformation $\mathbf{T}$ that gives pixel-wise vector correspondences between the two image representations $\Phi_{\mathbf{J}}$ and $\Phi_{\mathbf{I}}$. Abdelmunim [5] proposed that the vector dissimilarity measure can be used as

$$\mathbf{r} = \mathbf{SR}\Phi_{\mathbf{J}}(\mathbf{x}) - \Phi_{\mathbf{I}}(\mathbf{X}) \tag{77}$$

and the optimization energy function can be written as

$$E(\mathbf{S}, \mathbf{R}, \mathbf{Tr}) = \int_{\Omega} \delta_{\epsilon}(\Phi_{\mathbf{J}}, \Phi_{\mathbf{I}})\mathbf{r}^T\mathbf{r}d\Omega \tag{78}$$

where δ_{ϵ} is an indicator function defined as

$$\delta_{\epsilon}(\Phi_{\mathbf{J}}, \Phi_{\mathbf{I}}) = \begin{cases} 0 & \text{if } \min(|\Phi_{\mathbf{J}}|, |\Phi_{\mathbf{I}}|) > \epsilon \\ 1 & \text{if } \min(|\Phi_{\mathbf{J}}|, |\Phi_{\mathbf{I}}|) \leq \epsilon \end{cases} \tag{79}$$

The optimization of the given criterion can be done using the gradient descent method which can be written as

$$\begin{aligned} \frac{d}{dt}s &= 2\int_{\Omega} \delta_{\epsilon}\mathbf{r}^T[\nabla_s\mathbf{SR}\Phi_{\mathbf{J}}(\mathbf{x}) - \nabla\Phi_{\mathbf{I}}^T(\mathbf{X})\nabla_s\mathbf{X}]d\Omega \\ \frac{d}{dt}\theta &= 2\int_{\Omega} \delta_{\epsilon}\mathbf{r}^T[\mathbf{S}\nabla_{\theta}\mathbf{R}\Phi_{\mathbf{J}}(\mathbf{x}) - \nabla\Phi_{\mathbf{I}}^T(\mathbf{X})\nabla_{\theta}\mathbf{X}]d\Omega \\ \frac{d}{dt}tr &= 2\int_{\Omega} \delta_{\epsilon}\mathbf{r}^T[\nabla\Phi_{\mathbf{I}}(\mathbf{A})\nabla_{tr}\mathbf{A}]d\Omega \end{aligned} \tag{80}$$

where $s \in \{s_x, s_y\}$ and $tr \in \{t_x, t_y\}$. For more information, see [5].

An example of the registration step is shown in Figure 76.

3. Statistical Segmentation Approach

After the shape prior is registered to the initially segmented region, the graph cuts method integrating the intensity, spatial interaction, and shape models is used to obtain the final segmentation. In the graph cuts method, a *VB* (object) and surrounding organs (background) are represented using a gray level distribution models which are approximated by a linear combination of Gaussians (LCG) to better specify region borders between two classes (object and background). Then a weighted undirected graph is created with vertices corresponding to the set of volume voxels $\mathcal{P}$, and a set of edges connecting these vertices.

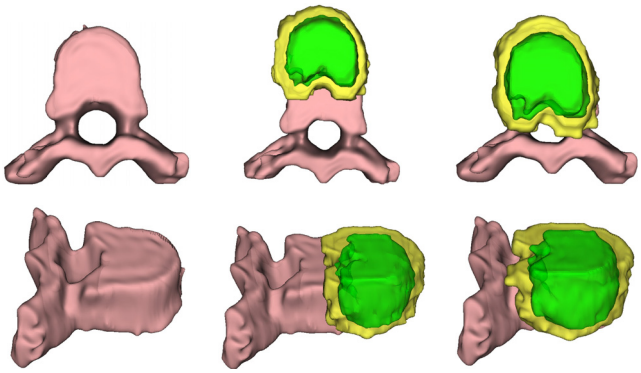

(a) (b) (c)

FIGURE 76 – The registration step. (a) The testing image (or initially segmented image) as shown with the pink color. The testing and 3D shape prior before and after the registration are shown in (b) and (c), respectively. Each row shows different views.

Each edge is assigned a nonnegative weight. The graph also contains two special terminal vertices s (source) "*VB*", and t (sink) "background". Consider a neighborhood system in $\mathcal{P}$, which is represented by a set $\mathcal{N}$ of all unordered pairs $\{p, q\}$ of neighboring voxels in $\mathcal{P}$. Let $\mathcal{L}$ the set of labels {"0", "1"}, correspond to *VB* and background regions respectively. Labeling is a mapping from $\mathcal{P}$ to $\mathcal{L}$, and the set of labeling is denoted by $\mathbf{f} = \{f_1, \ldots, f_p, \ldots, f_{|\mathcal{P}|}\}$. In other words, the label f_p, which is assigned to the voxel $p \in \mathcal{P}$, segments it into *VB* or background region. Now the goal is to find the optimal segmentation, best labeling $\mathbf{f}$, by minimizing the following energy function which combines region and boundary properties of segments as well as shape constraints. This function is defined as follows:

$$E(\mathbf{f}) = \sum_{p \in \mathcal{P}} S(f_p) + \sum_{p \in \mathcal{P}} D(f_p) + \sum_{\{p,q\} \in \mathcal{N}} V(f_p, f_q). \tag{81}$$

$S(f_p)$ measures how much assigning a label f_p to voxel p disagrees with the shape information. The shape penalty term is defined as $S(f_p) = -\log p(d_p|f_p)$. The distance marginal density of each class is calculated as

$$p(d_p \mid f_p) = \frac{h(d_p \mid \mathcal{O}, \mathcal{B})\, \pi_{\mathcal{O},\mathcal{B}}}{|\mathbf{C}_{d_p}|}. \tag{82}$$

These densities can be computed using Eqs. 70-75.

$D(f_p)$ measures how much assigning a label f_p to voxel p disagrees with the voxel intensity, I_p. $D_p(f_p) = -\log p(I_p \mid f_p)$ is formulated to represent the regional

properties of segments. To initially label the VB volume and to compute the data penalty term $D_p(f_p)$, the modified EM [22] method is used to approximate the gray level marginal density of each class f_p, VB and background region, using a LCG with $C^+_{f_p}$ positive and $C^-_{f_p}$ negative components as follows:

$$p(I_p \mid f_p) = \sum_{r=1}^{C^+_{f_p}} w^+_{f_p,r} \varphi(I_p \mid \theta^+_{f_p,r}) - \sum_{l=1}^{C^-_{f_p}} w^-_{f_p,l} \varphi(I_p \mid \theta^-_{f_p,l}), \tag{83}$$

where $\varphi(. \mid \theta)$ is a Gaussian density with parameter $\theta \equiv (\mu, \sigma^2)$ with mean μ and variance σ^2. $w^+_{f_p,r}$ means the rth positive weight in class f_p and $w^-_{f_p,l}$ means the lth negative weight in class f_p. These weights have a restriction $\sum_{r=1}^{C^+_{f_p}} w^+_{f_p,r} - \sum_{l=1}^{C^-_{f_p}} w^-_{f_p,l} = 1$.

$V(f_p, f_q)$ is the pairwise interaction model which represents the penalty for the discontinuity between voxels p and q. The simplest model of spatial interaction is the MGRF with the nearest 6-neighborhood. Therefore, for this specific model the Gibbs potential, γ, can be obtained analytically using the maximum likelihood estimator (MLE) for a generic MGRF in [26]. The Gibbs potential governing pairwise interaction is described as

$$V(f_p, f_q) = \gamma \delta(f_p \neq f_q). \tag{84}$$

In this equation γ is the potential value specifying the Gibbs potential. The approximate MLE of γ is:

$$\gamma^* = \frac{K^2}{K-1} \left(f_{\text{neq}}(\mathbf{f}) - \frac{1}{K} \right) \tag{85}$$

where $K = 2$ is the number of classes in the volume and $f_{\text{neq}}(\mathbf{f})$ denotes the relative frequency of the not equal labels in the voxel pairs.

The graph cuts method [88] is used as a energy minimization tool in the experiments. The goal is to find the optimal segmentation, and best labeling $\mathbf{f}$, by minimizing the following energy function in Eq. 81. To segment a VB, the volume is initially labeled based on its gray level probabilistic model. Initial segmentation based on the LCG models is then iteratively refined by using MGRF with

analytically estimated potentials. In this step, the graph cuts is used as a global optimization algorithm to find the segmented data that minimize a certain energy function, which integrates the LCG, MGRF, and 3D shape model. To segment a VB volume, a 3D graph where each vertex in this graph represents a voxel in the VB volume is used. A sample graph is shown in Figure 78. Let $\mathcal{G} = \{\mathcal{U}, \mathcal{E}\}$ be a graph with nonnegative edge weights where $\mathcal{U}$ and $\mathcal{E}$ represent the set of vertices and edges, respectively. The weight of each edge is defined as shown in Table 7. A weighted undirected graph is created with vertices corresponding to the set of volume voxels $\mathcal{T}$, and a set of edges connecting these vertices. Each edge is assigned a nonnegative weight. The graph also contains two special terminal vertices s (source) "*VB*", and t (sink) "background". Consider a neighborhood system in $\mathcal{T}$, which is represented by a set $\mathcal{N}$ of all unordered pairs $\{p, q\}$ of neighboring voxels in $\mathcal{T}$. Let $\mathcal{L}$ the set of labels, {"0", "1"}, correspond to the background and VB regions, respectively. Finally, the optimal segmentation surface between the VB and its background is obtained by finding the minimum cost cut on this graph. The minimum cost cut is computed exactly in polynomial time for two terminal graph cuts with positive edges weights via s/t Min-Cut/Max-Flow algorithm [88]. An example of the proposed segmentation is shown in Fig 77. (see [26,80,88] for more details).

B. Experiments and Discussion

The test results were achieved for 10 data sets of which the ground truths exist. The real data sets were scanned at 120kV and $1.0 - 3.0$mm slice thickness. All algorithms are run on a PC 3Ghz AMD Athlon 64 X2 Dual, and 3GB RAM. All implementations are in C++.

To compare the proposed method with other alternatives, VBs are subsequently segmented using other alternative methods. Finally, segmentation accuracy is measured for each method using the ground truths (expert segmentation). M1 represents the proposed algorithm. The alternative methods used in the ex-

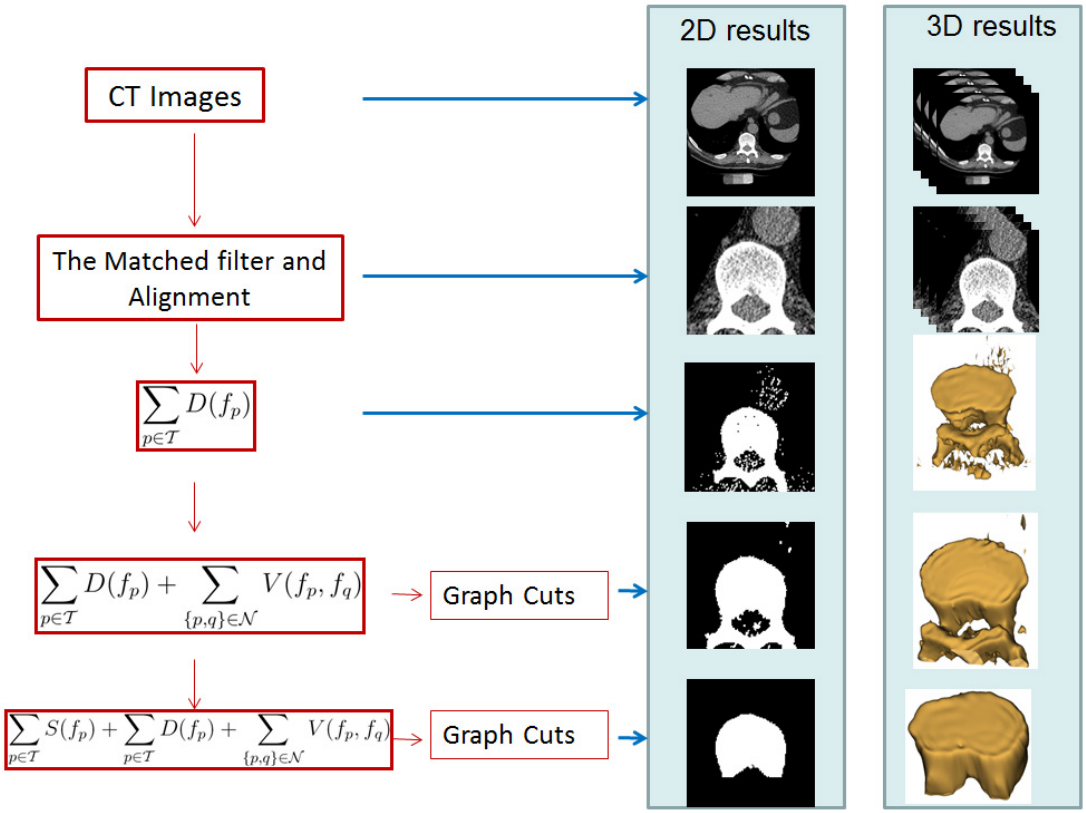

FIGURE 77 – An overall segmentation steps with 2D / 3D example. The Matched filter is employed to detect the VB region. Then, the initial segmentation using the LCG model is obtained. Finally the graph cuts method which integrates the LCG, MGRF, and shape probabilistic model is used to obtain the final segmentation.

TABLE 7
GRAPH WEIGHTS

Edge	Weight	for
$\{p,q\}$	γ	$f_p \neq f_q$
	0	$f_p = f_q$
$\{s,p\}$	$-ln[p(I_p \mid \text{“1”})p(d_p \mid \text{“1”})]$	$p \in \mathcal{U}$
	∞	$p \in \mathcal{O}$
	0	$p \in \mathcal{B}$
$\{p,t\}$	$-ln[p(I_p \mid \text{“0”})p(d_p \mid \text{“0”})]$	$p \in \mathcal{U}$
	0	$p \in \mathcal{O}$
	∞	$p \in \mathcal{B}$

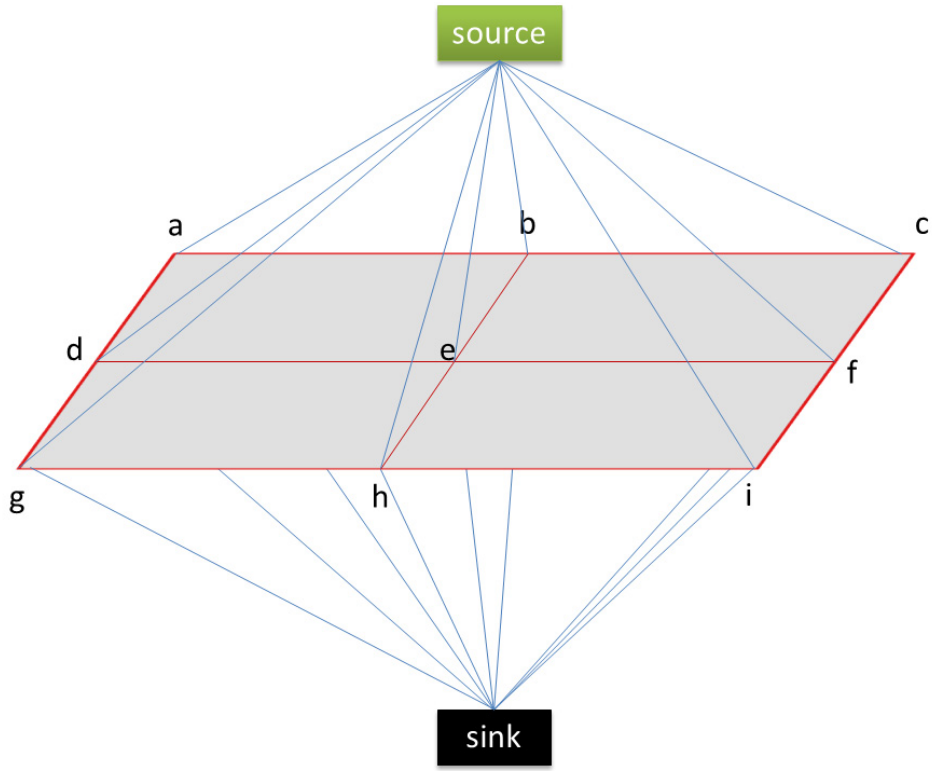

FIGURE 78 – An example of the graph $\mathcal{G} = \{\mathcal{U}, \mathcal{E}\}$. All vertices represented as $\mathcal{U} = \{\textit{source}, \textit{sink}, a, b, c, d, e, f, g, h, i\}$. *p-vertices* (pixels) are {a,...,i}. *l-vertices* (terminals or labels) are source (s) and sink (t). $\mathcal{E}$ is represented as lines connecting vertices. Lines connecting *p-vertices* to *l-vertices* represents *t-links*. Lines connecting each *p-vertex* with its neighboring *p-vertices* represent *n-links*. *n-links* are constructed for 4-neighboring system. (In the graph, the pixel e represents p in the equations.)

Algorithm 6 Proposed VB segmentation framework

Given : The input image, the ESP ($\mathbf{J}$ as a source information), the probabilistic 3D shape model ($\mathbf{d}$).

Objective : To obtain the desired labeling ($\mathbf{f}$) using the required transformation matrix ($\mathbf{T}$).

1. Detect the VB region using [27]

2. Obtain the initial segmentation ($\mathbf{f}^*$) using graph cuts which integrates the intensity and spatial interaction models only.

3. Register the shape prior to the initially segmented image. $\mathbf{J}$ and $\mathbf{f}^*$ will be the source and target information, respectively. After the transformation, the embedded shape model and its features are described as follows:

- After each point $\mathbf{x} \in \mathcal{P}_s$ is transformed to the new point $\mathbf{X}$, the shape model is registered to the image domain. New volumes $\mathcal{O}^{new}$, $\mathcal{B}^{new}$, and $\mathcal{V}^{new}$ are obtained.

- The the object / variability surface is updated and named as $\mathbf{C}_{\mathcal{OV}}^{new}$. The distance probabilistic model is obtained again as $d_r = \min_{r \in \mathbf{C}_{\mathcal{OV}}^{new}} \|r - c\|$, from a pixel $r \in \mathcal{V}^{new}$ to the organ / variability surface $\mathbf{C}_{\mathcal{OV}}^{new}$.

- The new probabilistic distance functions at each pixel $r \in \mathcal{V}^{new}$ is $p(d_r \mid \mathbf{I}) = p(d_p \mid \mathbf{I})$. Hence, new iso-surfaces at the same distance ($d_r = d_p$) will have the same probabilistic distance value with the iso-surfaces which are obtained before the registration. An example of the registration step is shown in Figure 76.

4. Compute the final segmentation ($\mathbf{f}$) using shape based graph cuts.

TABLE 8
ACCURACY AND TIME PERFORMANCE OF THE VB SEGMENTATION ON 10 DATA SETS.

	M1 (Proposed)	**M2**	**M3**	**M4**
Min. error, %	6.4	5.6	6.3	15.5
Max. error, %	9.2	86.5	90.9	105.7
Mean error, %	7.2	38.3	42.4	52.7
Stand. dev.,%	1.2	28.8	30.9	32.5
Average time,sec	34.1	8.3	41.5	8.9

periments are represented as M2 (for the graph cuts method without shape prior information), M3 (for b-spline-based interpolation), and M4 (for statistical level sets). To evaluate the results, the percentage segmentation error is calculated as follows:

$$error\% = 100(1 - \frac{S_a \bigcap S_m}{S_a \bigcup S_m}) \tag{86}$$

where S_m and S_a represent manually and automatically segmented volumes, respectively.

The statistical analysis of the proposed method is shown in Table 8. In this table, the results of the proposed segmentation method and three alternatives are shown. The average error of the VB segmentation on 10 clinical image sets is 7.2% for the proposed method. An example that shows 3D segmentation results of all tested methods for a clinical data set is shown in Fig 79. In this figure, the red color represents the misclassified voxels.

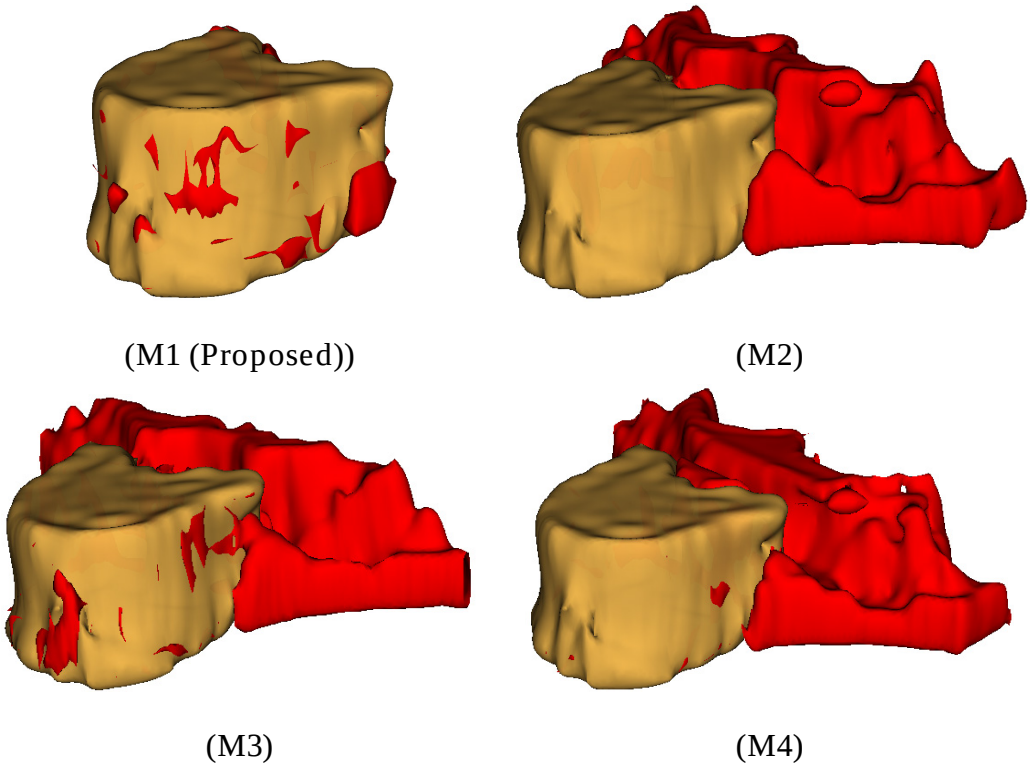

FIGURE 79 – 3D results of a clinical data set. (M1) The result of the proposed method, (M2) results of graph cuts without shape prior, (M3) results of the Level sets, and (M4) results of the b-spline based interpolation. The red color shows the segmentation errors.

CHAPTER V

CONCLUSION AND FUTURE WORK

This dissertation have presented image labeling using segmentation and registration methods with three pieces of information. More specifically, it focused on the shape modeling, shape registration, and selecting the optimization method to obtain the optimum labeling. The energy functionals were optimized using three different approaches which have different advantages: i) the level sets which uses the gradient descent and simplex optimizations, ii) the iterated conditional modes (ICM), and iii) Graph cuts.

A. What is Accomplished

In general, the dissertation accomplished followings:

- The proposed method solves the classical problems existing in the intensity-based frameworks.
- The shape model is embedded into the image domain automatically without any user interaction and point correspondence.
- The shape registration and hence the shape based segmentation results are greatly improved under various challenges as compared with the closest methods, which Paragios et al. [47], and Tsai et al. [14]. These methods have limitations to capture the object-of-interest if the source and target shapes have inhomogeneous scale differences. In this dissertation, the geometrical scaling is proposed as an approximation, since the SDF is not invariant to inhomogeneous scaling. New probabilistic shape models are proposed to enhance the conventional shape based segmentation results.

- The proposed methods are less variant to the shape initialization with respect to the some of methods such as [8, 9, 25, 81].
- The original ICM method, which was originally proposed by Besag [53], is extended by integrating the shape prior.
- The spinal processes, which is not required in the BMD measurements and fracture analysis, are eliminated using the shape prior.
- In the proposed methods, there is no any region restriction, and the proposed framework is processed on different regions.
- If the proposed method in the Chapter 3 is compared with most of the published bone segmentation methods (such as in [36,51,54]), the large execution time is reduced effectively.
- The proposed methods are not dependent on any the VB identification step thanks to the new universal shape model and its embedding step.
- An extension study of previously published method in [26] is extended in 3D form and improved to work automatically. In [26] the shape model is assumed to be registered in advance. In this dissertation, the probabilistic shape model is registered automatically to the image domain as in [34].

B. Directions to Future Works

Possible future works can be directed as follows:

- In the literature, the segmentation is coupled with the pose estimation such as Sandhu et al. proposed [33]. They present a nonrigid approach to jointly solving the tasks of 2D-3D pose estimation from a 2D scene and 2D image segmentation. The proposed work in Chapter II can be upgraded using the similar idea.

- The proposed methods handle the VB segmentation problem successfully. However, the automated VB separation algorithm in Chapter III can be enhanced to increase the accuracy.

- To assist the VB fracture analysis, an automated point correspondence detection algorithm, such as scale-invariant feature transform (SIFT), can be tested to detect the VB height changes. In this problem, the corresponding points on the same patient, which is scanned at specific time intervals, should be detected successfully.

- A possible BMD measurements and improvements can be studied. The broad literature review is required for this study since there is no information on this issue in this dissertation.

- The proposed shape based ICM method can be compared with other spatially discrete optimization methods such as simulated annealing, loopy belief propagation, graph cuts, and tree-reweighted message passing. One can read [50] for an example comparison.

REFERENCES

[1] D. Cremers. *Statistical Shape Knowledge in Variational Image Segmentation*. Ph.D Dissertation, 2002.

[2] A. Ali. *Image labeling by energy minimization with appearance and shape priors*. Ph.D Dissertation, University of Louisville, May, 2008.

[3] S. Geman and D. Geman. Stochastic relaxation, gibbs distributions, and the bayesian restoration of images. *IEEE Transactions on Pattern Analysis and Machine Intelligence*, 6:721–741, 1984.

[4] H. Derin and H. Elliott. Modeling and segmentation of noisy and textured images using gibbs random fields. *IEEE Transactions on Pattern Analysis and Machine Intelligence*, 9(1):39–55, 1987.

[5] H. Abd El Munim. *Implicit Curve/Surface Evolution with Application to the Image Segmentation Problem*. Ph.D Thesis, University of Louisville, May, 2007.

[6] N. D. Salih and D. C. L Ngo. An efficient boundary-based approach for shape representation. In *Information and Communication Technologies, 2006. ICTTA '06. 2nd*, 2006.

[7] T. F. Cootes, C. J. Taylor, Cooper D. H., and Graham J. Active shape models - their training and application. In *Computer Vision and Image Understanding*, volume 61, pages 38–51, 1995.

[8] T. F. Cootes, G. J. Edwards, and C. J. Taylor. Active appearance models. In *Proc. European Conference on Computer Vision*, 1998.

[9] T. F. Cootes, G. J. Edwards, and C. J. Taylor. Active appearance models. *IEEE Transactions on Pattern Analysis and Machine Intelligence*, 23(6):681–685, 2001.

[10] M. Kass, A. Witkin, and D. Terzopoulos. Snakes: Active contour models. *Int. J. of Computer Vision*, 1(4):321331, 1988.

[11] S. Osher and J. A. Sethian. Fronts propogating with curvature-dependent speed: algorithms based on hamilton-jacobi formulations. *J. Comp. Phys.*, 79:12–49, 1988.

[12] M. Leventon, E. Grimson, and O. Faugeras. Statistical shape influence in geodesic active contours. In *Proc. of International Conference on CVPR*, volume 1, pages 316–323, 2000.

[13] M. Rousson, N. Paragios, and R. Deriche. Implicit active shape models for 3d segmentation in mri imaging. In *Medical Image Computing and Computer Assisted Intervention (MICCAI)*, pages 209–216, 2004.

[14] A. Tsai, A. Yezzi, W. Wells, C. Tempany, D. Tucker, A. Fan, W. E. Grimson, and A. Willsky. A shape-based approach to the segmentation of medical imagery using level sets. *IEEE Trans. on Medical Imaging*, 22(2):137–154, 2003.

[15] D. Cremers, S. J. Osher, and S. Soatto. Kernel density estimation and intrinsic alignment for shape priors in level set segmentation. *International Journal of Computer Vision*, 69(3):335–351, 2006.

[16] D. Cremers, M. Rousson, and R. Deriche. A review of statistical approaches to level set segmentation: Integrating color, texture, motion, and shape. *International Journal of Computer Vision*, 72(2):195–215, 2007.

[17] T. Heimann and H. P. Meinzer. Statistical shape models for 3d medical image segmentation: a review. *Medical Image Analysis*, 13:543–563, 2009.

[18] D. Zhang and G. Lu. Review of shape representation and description techniques. *Pattern Recognition*, 37:1–19, 2004.

[19] R. Duda, P. Hart, and D. Stork. *Pattern Classification*. John Wiley and Sons Inc., 2001.

[20] S. Borman. The expectation maximization algorithm: A short tutorial. technical report available at http://www.seanborman.com/publications. 2004.

[21] T. Moon. The expectation-maximization algorithm. *IEEE Signal Processing Magazine*, 11:47–60, 1996.

[22] A.A. Farag, A. El-Baz, and G. Gimelfarb. Density estimation using modified expectation maximization for a linear combination of gaussians. In *Proceedings of the International Conference on Image Processing*, number 3, pages 1871–1874, 2004.

[23] T. F. Chan and L. A. Vese. Active contours without edges. *IEEE Trans. Image Process.*, 10(2):266277, 2001.

[24] A. A. Farag and H. Hassan. Adaptive segmentation of multi-modal 3d data using robust level set techniques. In *Proc. of International Conference on Medical Image Computing and Computer-Assisted Intervention*, pages 143–150, 2004.

[25] C. Li, C. Xu, C. Gui, and M. D. Fox. Level set evolution without re-initialization: A new variational formulation. In *Proc. of the 2005 IEEE Computer Society Conference on Computer Vision and Pattern Recognition*, 2005.

[26] A. M. Ali and A. A. Farag. Automatic lung segmentation of volumetric low-dose ct scans using graph cuts. In *Proceedings of the International Symposium on Visual Computing (ISVC'08)*, pages 258–267, 2008.

[27] M. S. Aslan, A. Ali, H. Rara, B. Arnold, A. A. Farag, R. Fahmi, and P. Xiang. A novel 3d segmentation of vertebral bones from volumetric ct images using graph cuts. In *Proceedings of 5th International Symposium on Visual Computing (ISVC'09)*, pages 519–528, 2009.

[28] Y. Boykov, O. Veksler, and R. Zabih. Fast approximation energy minimization via garph cuts. *IEEE Transactions on Pattern Analysis and Machine Intelligence*, 23(11):12221239, 2001.

[29] Y. Boykov, V. S. Lee, H. Rusinek, and R. Bansal. Segmentation of dynamic n-d data sets via graph cuts using markov models. In *Proceedings of MICCAI-2001, LNCS, 2208, pp.1058-1066*, 2001.

[30] M. S. Aslan, H. Abdemunim, and A. A. Farag. A probabilistic shape-based segmentation using level sets. In *1st IEEE Workshop on Information Theory in Computer Vision and Pattern Recognition (ICCV workshop)*.

[31] X. Huang, N. Paragios, and D. Metaxas. Shape registration in implicit spaces using information theory and free form deformations. *IEEE Trans. Pattern Analysis and Machine Intelligence*, 28(8):1303– 1318, 2006.

[32] M. Taron, N. Paragios, and M. P. Jolly. Registration with uncertainties and statistical modelling of shapes with variabile metric kernels. *IEEE Trans. on Pattern Analysis and Machine Intelligence*, 1(8):1–14, 2007.

[33] R. Sandhu, S. Dambreville, A. Yezzi, and A. Tannenbaum. A nonrigid kernel-based framework for 2d-3d pose estimation and 2d image segmentation. *IEEE Transactions on Pattern Analysis and Machine Intelligence*, 33(6):1098–1115, 2011.

[34] M. S. Aslan, A. Ali, A. A. Farag, H. Abdelmunim, B. Arnold, and P. Xiang. A new segmentation and registration approach for vertebral body analysis. In *Proceedings of 5th International Symposium on Biomedical Imaging (ISBI'11)*, pages 2006–2009, 2011.

[35] M. B. Stegmann. *Active appearance models: theory, extensions, and cases*. Master Thesis, Technical University of Denmark, 2000.

[36] T. Klinder, J. Ostermann, M. Ehm, A. Franz, R. Kneser, and C. Lorenz. Automated model-based vertebra detection, identification, and segmentation in ct images. *Medical Image Analysis*, 13:471–482, 2009.

[37] M. Roberts, T. Cootes, , and J. Adams. Vertebral shape: Automatic measurement with dynamically sequenced active appearance models. In *Proceedings of the International Conference on Medical Image Computing and Computer Assisted Intervention*, number 2, pages 733–740, 2005.

[38] S. S. Mahdavi, N. Chng, I Spadinger, W. J. Morris, and S. E. Salcudean. Semi-automatic segmentation for prostate interventions. *Medical Image Analysis*, 15:226–237, 2011.

[39] J. Schmid, J. Kim, and M. N. Thalmann. Robust statistical shape models for mri bone segmentation in presence of small field of view. *Medical Image Analysis*, 15:155–168, 2011.

[40] G. Tsechpenakis and S. P. Chatzis. Deformable probability maps: Probabilistic shape and appearance-based object segmentation. *Computer Vision and Image Understanding*, 115:1157–1169, 2011.

[41] P. Yan, S. Xu, B. Turkbey, and J. Kruecker. Adaptively learning local shape statistics for prostate segmentation in ultrasound. *IEEE Transactions on Biomedical Engineering*, 58:633–641, 2011.

[42] P. K. Saha, G. Liang, J. M. Elkings, A. Coimbra, L. T. Duong, D. S. Williams, and M. Sonka. A new osteophyte segmentation algorithm using the partial shape model and its applications to rabbit femur anterior cruciate ligament transection via micro-ct imaging. *IEEE Transactions on Biomedical Engineering*, 58(8):2212–2238, 2011.

[43] D. S. Pu, J. Pail, X. Meng, J. E. Roos, and G. D. Rubin. Shape break-and-repair strategy and its application to automated medical image segmentation. *IEEE Transactions on Visualization and Computer Graphics*, 17(1):115–125, 2011.

[44] J. Feulner, S. K. Zhou, M. Hammon, S. Seifert, M. Huber, D. Comanicie, J. Hornegger, and A. Cavallaro. A probabilistic model for automatic segmentation of the esophagus in 3-d ct scans. *IEEE Transactions on Medical Imaging*, 30(6):1252–1265, 2011.

[45] A. Gostasby. Image registration tutorial. In *Proc. of Computer Vision and Pattern Recognition*, 2004.

[46] J. M. Fitzpatrick, D. L. G. Hill, and Jr. C. R. Maurer. *Image Registration*. Chapter 8 of ”Handbook of Medical Imaging,Milan Sonka and J. Michael Fitzpatrick, eds., SPIE Press, 2000.

[47] N. Paragios, M. Rousson, and V Ramesh. Matching distance functions: A shape-to-area variational approach for global-to- local registration. In *Proc. Seventh European Conf. Computer Vision*, volume 79, pages 775–789, 2002.

[48] L. K. Nielsen. *Elastic Registration of Medical MR Images*. Cand. Scient. Thesis in Computational Science, University of Bergen, 2003.

[49] X. Gao, B. Wang, D. Tao, and X. Li. A relay level set method for automatic image segmentation. *IEEE Transactions on Systems, Man, Cybernetics.*, 41(2):518–526, 2011.

[50] R. Szeliski, R. Zabih, D. Scharstein, O. Veksler, V. Kolmogorov, A. Agarwala, M. F. Tappen, and C. Rother. A comparative study of energy minimization methods for markov random fields. In *In Proceedings of ECCV*, 2006.

[51] A. Mastmeyer, K. Engelke, C. Fuchs, and W. A. Kalender. A hierarchical 3d segmentation method and the definition of vertebral body coordinate systems for qct of the lumbar spine. *Medical Image Analysis*, 10(4):560–577, 2006.

[52] J. Yao, S. D O’Connor, and R. M. Summers. Automated spinal column extraction and partitioning. In *Proceedings of IEEE International Symposium on Biomedical Imaging*, 2006.

[53] J. E. Besag. On the statistical analysis of dirty pictures. *Journal of the Royal Statistical Society, Series B*, 48:259–302, 1986.

[54] J Kaminsky, P. Klinge, M. Bokemeyer, W. Luedemann, and M. Samii. Specially adapted interactive tools for an improved 3d-segmentation of the spine. *Computerized Medical Imaging and Graphics*, 28(3):119–127, 2004.

[55] A. Ali, A. A. Farag, and A. El-Baz. Graph cuts framework for kidney segmentation with prior shape constraints. In *Proc. of International Conference on Medical Image Computing and Computer-Assisted Intervention (MICCAI'07)*, pages 384–392, 2007.

[56] S. Mahmoodi. Shape-based active contours for fast video segmentation. *IEEE Transactions on Signal Processing Letters*, 16(10):857–860, 2009.

[57] D. Mumford and J. Shah. Optimal approximations by piecewise smooth functions and associated variational problems. *Xommun. Pure. Appl. Math.*, 42(4):577688, 1989.

[58] Y. Gao, R. Sandhu, G. Fichtinger, and A. R. Tannenbaum. A coupled global registration and segmentation framework with application to magnetic resonance prostate imagery. *IEEE Transactions on Medical Imaging*, 29:1781–1794, 2010.

[59] Y. Zhu, X. Papademetris, A. J. Sinusas, and J. Duncan. Segmentation of the left ventricle from cardiac mr images using a subject-specific dynamical model. *IEEE Trans. on Medical Imaging*, 29(3):669687, 2010.

[60] F. Heckel, O. Konrad, H. K. Hahn, and H. O. Peitgen. Interactive 3d medical image sementation with energy-minimizing implicit functions. *Computer and Graphics*, 35:275–287, 2011.

[61] T. Shen, H. Li, and X. Huang. Active volume models for medical image segmentation. *IEEE Transactions on Medical Imaging*, 30(3):774–792, 2011.

[62] A. Dawoud. Lung segmentation in chest radiographs by fusing shape information in iterative thresholding. *IET Computer Vision*, 5(3):185–190, 2011.

[63] J. Lee, S. Kim, S. Kim, and W. K. Chung. Automated segmentation of the lumbar pedicle in ct images for spinal fusion surgery. *IEEE Transactions on Biomedical Engineering*, 58(7):2051–2064, 2011.

[64] B. V. K. V. Kumar, M. Savvides, and C. Xie. Correlation pattern recognition for face recognition. In *Proceedings of the IEEE*, number 94(11), pages 1963–1976, 2006.

[65] A. J. Nelder and R. Mead. A simplex method for function minimization. *Computer Journal*, 7:308313, 1968.

[66] J. S. Lagarias, J. A. Reeds, M. H. Wright, and P. E. Wright. Convergence properties of the nelder-mead simplex method in low dimensions. *SIAM Journal of Optimization*, 9(1):112–147, 1998.

[67] N. Paragios and R. Deriche. Mayfield handbook of technical and scientific writing. In *IEEE Int. Conf. on Computer Vision and Pattern Recognition (CVPR'99)*, volume 2, pages 300–305, 1999.

[68] W. A. Kalender, D. Felsenberg, H. Genant, M. Fischer, J. Dequeker, and J. Reeve. The european spine phantom - a tool for standardization and quality control in spinal bone measurements by dxa and qct. *European J. Radiology*, 20:83–92, 1995.

[69] G. M. Blake, H. W. Wahner, and I. Fogelman. *Dual energy x-ray absorptiometry and ultrasoung in clinical practice*. Martin Dunitz, 1999.

[70] S. Tapp. *A markov model of secondary prevention of osteoporotic hip fractures*. Ph.D Dissertation, 2003.

[71] Department of Health and Human Services. *A report of the surgeon general: Bone Health and Osteoporosis*. U. S. Public Health Service, 2004.

[72] www.ghcchina.com/images.

[73] www.actonel.com.

[74] www.naturalhealthvision.com.

[75] P. Szulc and P. D Delmas. *Vertebral fracture initiative resource pack*. International Osteoporosis Foundation, 2005.

[76] K. Kang, K. Engelke, and W. A. Kalender. New accurate and precise 3d segmentation method for skeletal structures in volumetric ct data. *IEEE Transaction on Medical Imaging (TMI)*, 22(5):586–598, 2003.

[77] Y. Kim and D. Kim. A fully automatic vertebra segmentation method using 3d deformable fences. *Computerized Medical Imaging and Graphics*, 33:343–352, 2009.

[78] S. Tan, J. Yao, M. M. Ward, L. Yao, and R. M. Summers. Computer aided evaluation of ankylosing spondylitis using high-resolution ct. *IEEE Transaction on Medical Imaging (TMI)*, 27(9):1252–1267, 2008.

[79] T. B. Sebastiana, H. Teka, J. J. Criscob, and B. B. Kimia. Segmentation of carpal bones from ct images using skeletally coupled deformable models. *Medical Image Analysis*, 7(1):21–45, 2003.

[80] M. S. Aslan, A. Ali, A. A. Farag, H. Rara, B. Arnold, and P. Xiang. 3d vertebral body segmentation using shape based graph cuts. In *Proceedings of 5th International Conference on Pattern Recognition (ICPR'10)*, pages 3951–3954, 2010.

[81] M. S. Aslan, E. Mostafa, H. Abdelmunim, A. Shalaby, and A. A. Farag. A novel probabilistic simultaneous segmentation and registration using level set. In *Proceedings of the International Conference on Image Processing*, volume 94, pages 2161 – 2164, 2011.

[82] R. C. Dubes and A. K Jain. Random field models in image analysis. *Journal of Applied Statistics*, 16:131–164, 1989.

[83] A. Ali, A. A. Farag, and G. Gimel'farb. A comparative study of energy minimization methods for markov random fields. In *In Proceedings of ECCV*, 2008.

[84] O. H. North. An analysis of the factors which determine signal / noise discrimination in pulsed-carrier svstems. In *Proceedings of IEEE:RCA Labs., Princeton, NJ, Rep. PTR-6C.*, pages 1016–1063, 1943.

[85] G. L. Turin. An introduction to matched filters. *IEEE Transactions on Information Theory*, 6(3):311–329, 1960.

[86] M. S. Aslan, A. Ali, H. Rara, and A. A. Farag. An automated vertebra identification and segmentation in ct images. In *Proceedings of 5th International Conference on Image Processing (ICIP'10)*, pages 233–236, 2010.

[87] L. W. Goldman. Principles of ct: Radiation dose and image quality. *Journal of Nuclear Medicine Technology*, 35:213–225, 2007.

[88] Y. Boykov and V. Kolmogorov. An experiment comparison of min-cut / max-flowalgorithms for energy minimization in vision. *IEEE Transaction on Pattern Analysis and Machine Intelligence*, 26:1124–1137, 2004.

[89] S. Z. Li. *Markov random field modeling in image analysis*. Springer: Computer science workbench, 2001.

APPENDIX I

SPATIAL INTERACTION MODELLING USING MGRF

1. Spatial Interaction Model

Spatial interaction helps correcting errors and recovering missing information in the image labeling problem [26]. Dubes and Jain discussed many random field models. The objective is to estimate the optimum unconditional probability distribution of the desired map (labeling), $p(\mathbf{f})$. In reality, the random field F is not directly observable in the experiment. The realized configuration of F, which is $\mathbf{f}$ based on the observation $\mathbf{I}$, is need to be estimated based on the likelihood function $p(\mathbf{I} \mid \mathbf{f})$ [88].

Let $\mathcal{N}$ be a neighborhood system for Ω. It is defined as

$$\mathcal{N} = \{\mathcal{N}_i \mid \forall i \in \Omega\}. \tag{87}$$

Figure 80 shows orders of a neighboring system. In the first order system (4-neighborhood system), every site (pixel) has four neighbors. In the second order system (8-neighborhood system), there are eight neighbors around the interior site, $\mathbf{p}$. The numbers in Fig. 80 represents the order of neighboring sites.

An MRF is characterized by its local property. Maximum-A-Posteriori (MAP) probability is one of the most popular statistical criteria in MRF labeling [89]. The MRF is defined as follows:

Definition 1 (*Markov Random Field*). *F is said to be a Markov random field on Ω with respect to a neighboring system $\mathcal{N}$ if and only if positivity, markovianity, and homogeneity conditions are satisfied:*

FIGURE 80 – Order of the neighboring system .

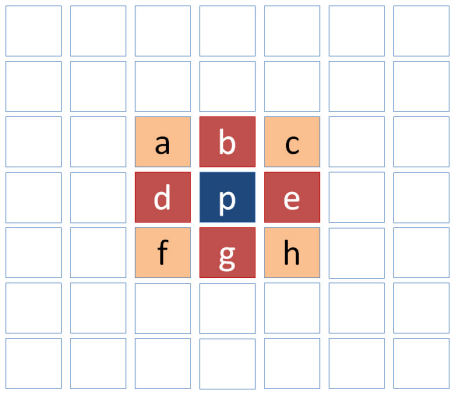

FIGURE 81 – Second order of the neighboring system.

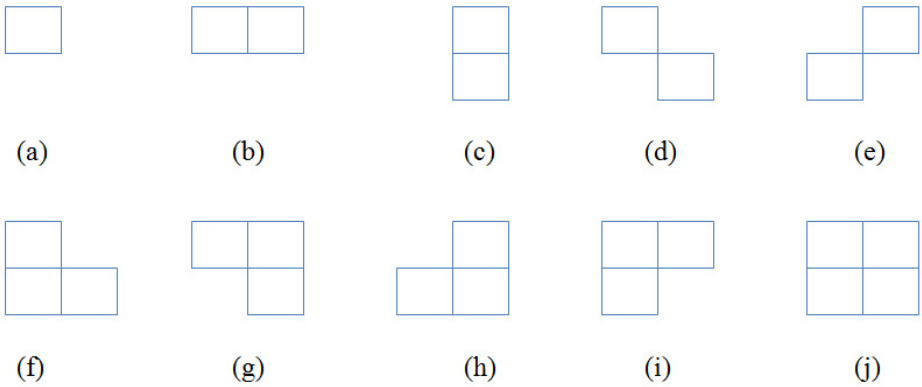

FIGURE 82 – Cliques types of the second order neighborhood.

- $p(F = \mathbf{f}) > 0$ *(positivity)*
- $p(F = f_i \mid F = f_{\Omega-\{i\}}) = p(F = f_i \mid F = f_{N_i})$ *(markovianity), where* $f_{\Omega-\{i\}}$ *stands for all pixels except* i*, and* $f_{N_i} = \{f_{i'} \mid i' \in N_i\}$ *denotes for the set of labels at the sites neighboring* i*.*
- $p(F = f_{\Omega_i} \mid F = f_{\mathcal{N}_i})$ *is same for all sites* i *(homogeneity)*

A GRF describes the joint distribution of pixel labels. The GRF is characterized by its global property. The definition of the GRF is defined as follows:

Definition 2 (*Gibbs Random Field*). *F is said to be a Gibbs random field (GRF) on Ω with respect to a neighboring system $\mathcal{N}$ if and only if random variables in F obey a Gibbs distribution.*

A Gibbs distribution takes the following form

$$p(\mathbf{f}) = \frac{1}{Z}\exp(-\frac{U(\mathbf{f})}{T}) \tag{88}$$

where

$$Z = \sum_{f \in F}\exp(-\frac{U(\mathbf{f})}{T}) \tag{89}$$

is a normalizing constant called the partition function, T is a control parameter called the temperature which is assumed to be 1 unless otherwise stated, and $U(\mathbf{f})$ is the Gibss energy function. The energy is a sum of clique functions $V_c(\mathbf{f})$ over all possible cliques $\mathcal{C}$ as

$$U(\mathbf{f}) = \sum_{c \in \mathcal{C}} V_c(\mathbf{f}). \tag{90}$$

A clique is a set of sites in which all pairs of sites are neighbors. There are $K(\geq 2)$ discrete labels in the label set, $L = \{0, \ldots, K-1\}$. A clique potential depends on the type "c" related to size, shape, and orientation of the clique. The clique potentials can be defined by

$$V_c(f) = \begin{cases} \zeta_c & \text{if all sites on } c \text{ have the same label} \\ -\zeta_c & \text{otherwise} \end{cases} \tag{91}$$

where ζ_c is the potential for type-c cliques. Using Derin-Elliott model [4], the clique potential can also be expressed as follows:

$$V_1(f_i) = \gamma_0 f_i, V_2(f_i, f_j) = \begin{cases} \beta_r & \text{if} f_i = f_j, \\ -\beta_r & \text{otherwise} \end{cases}$$

where γ_0 represents the potential of single-size cliques as shown in the Figure 82(a), and $\beta_r = \{\beta_1, \beta_2, \beta_3, \beta_4\}$ represent the potentials of "two-site" cliques as shown in the Figure 82(b-e). Farag et al. [22] proposed an analytic method to estimate the parameter of a specific MGRF model.

Theorem 1 (*The Hammersler-Clifford theorem*). *The Hammersler-Clifford theorem (1971) states that F is an MRF on Ω with respect to $\mathcal{N}$ if and only if F is a GRF on Ω with respect to $\mathcal{N}$.*

A proof that a GRF is an MRF is given as follows. In the proof, it is needed to find that $p(f_i \mid f_{\Omega-\{i\}}) = p(f_i \mid f_{N_i})$.

Proof 1 (*The Hammersler-Clifford theorem*). *Let $p(\mathbf{f})$ be a Gibbs distribution on Ω with respect to $\mathcal{N}$. Conditional probability can be written as*

$$p(f_i \mid f_{\Omega-\{i\}}) = \frac{p(f_i, f_{\Omega-\{i\}})}{p(f_{\Omega-\{i\}})} = \frac{p(\mathbf{f})}{\sum_{f_i' \in \mathcal{L}} p(\mathbf{f}')} \tag{92}$$

where $\mathbf{f}' = \{f_1, \ldots, f_{i-1}, f_i', \ldots, f_m\}$ is any set of random variables which agrees with $\mathbf{f}$ at all sites except possibly i.

From Eq. 88, it can be written

$$p(\mathbf{f}) = \frac{1}{Z} \exp(-\sum_{c \in \mathcal{C}} V_c(\mathbf{f})) \tag{93}$$

which provides a formula for calculating the conditional probability $p(f_i \mid f_{\Omega-\{i\}})$. Hence, using the Eqs. 92 and 93, the following equation can be written

$$p(f_i \mid f_{\Omega-\{i\}}) = \frac{\exp(-\sum_{c \in \mathcal{C}} V_c(\mathbf{f}))}{\sum_{f_i'} \exp(-\sum_{c \in \mathcal{C}} V_c(\mathbf{f}'))}. \tag{94}$$

Let divide $\mathcal{C}$ into two set $\mathcal{A}$ and $\mathcal{B}$ with assuming $\mathcal{A}$ consists of cliques containing i, and $\mathcal{B}$ does not consist of cliques containing i. Then Eq. 94 can be written as

$$\begin{aligned} p(f_i \mid f_{\Omega-\{i\}}) &= \frac{\exp[-(\sum_{c\in\mathcal{A}} V_c(\mathbf{f}) + \sum_{c\in\mathcal{B}} V_c(\mathbf{f})]}{\sum_{f_i'}\{\exp[-(\sum_{c\in\mathcal{A}} V_c(\mathbf{f}') + \sum_{c\in\mathcal{B}} V_c(\mathbf{f}'))]\}} \\ &= \frac{[\exp(-\sum_{c\in\mathcal{A}} V_c(\mathbf{f}))][\exp(-\sum_{c\in\mathcal{B}} V_c(\mathbf{f}))]}{\sum_{f_i'}\{[\exp(-\sum_{c\in\mathcal{A}} V_c(\mathbf{f}'))][\exp(-\sum_{c\in\mathcal{B}} V_c(\mathbf{f}'))]\}}. \end{aligned} \tag{95}$$

If $V_c(\mathbf{f}) = V_c(\mathbf{f}')$ for any clique c which does not contain i. Hence, $\exp(-\sum_{c\in\mathcal{B}} V_c(\mathbf{f}))$ cancels from both numerator and denominator. Finally, the probability depends only on the potential of the cliques containing i

$$p(f_i \mid f_{\Omega-\{i\}}) = \frac{\exp(-\sum_{c\in\mathcal{A}} V_c(\mathbf{f}))}{\sum_{f_i'}(\exp(-\sum_{c\in\mathcal{A}} V_c(\mathbf{f}')))}. \tag{96}$$

Eq. 96 indicates that the probability depends on labels at i' s neighbors. This proves that a Gibbs random field is a Markov random field can be shown as

$$p(f_i \mid f_{\Omega-\{i\}}) = \frac{\exp(-\sum_{c\in\mathcal{A}} V_c(\mathbf{f}))}{\sum_{f_i'}(\exp(-\sum_{c\in\mathcal{A}} V_c(\mathbf{f}')))} = p(f_i \mid f_{N_i}). \tag{97}$$

CURRICULUM VITAE

A. Contact Information

Melih Seref Aslan
melih.aslan@louisville.edu
melihaslantr@yahoo.com
1-502-345-2182

B. Research Interests

Medical Imaging, Image Processing, Pattern Recognition, Statistical Shape Models, Segmentation and Registration Methods.

C. Education

University of Louisville, Louisville, Kentucky USA

Ph.D., Electrical & Computer Engineering, May, 2012,

- Dissertation Topic: "Probabilistic and Geometric Shape Based Segmentation Methods"
- GPA: 3.60
- Advisor: Aly A. Farag

University of South Alabama, Mobile, AL, USA

M.Sc., Electrical & Computer Engineering, August, 2007

Fatih University, Istanbul, TURKEY

B.Sc., Electronics Engineering, July, 2005

- Full Tuition Waive Award.

D. Honors and Awards

- University of Louisville Graduate Dean's Citation Award, 2012.
- Graduate Research Assistantship for PhD study at University of Louisville (under supervision of Dr. Aly A. Farag).
- Graduate Research Assistantship for Master study at University of South Alabama(under supervision of Dr. Mohamed S. Alam).
- Full Scholarship to include all tuition and fees waived by Fatih University.

E. Publications

1. **Melih S. Aslan**, Aly A. Farag, Ben Arnold, Ping Xiang, "Statistical shape based segmentation of vertebral bodies," under review.
2. **Melih S. Aslan**, Hossam Abdelmunim, Aly A. Farag, "A Probabilistic Shape-based Segmentation Approach Using Level Sets," under review.
3. **Melih S. Aslan**, Hossam Abdelmunim, Aly A. Farag, "A Probabilistic Shape-based Segmentation Using Level Sets," International Conference of Computer Vision (ICCV)-Workshop, 2011.
4. **Melih S. Aslan**, Hossam Abdelmunim, Aly A. Farag, Ben Arnold, Eslam Mustafa, Ping Xiang, "A new shape based segmentation framework using statistical and variational methods," Proc. of 2011 IEEE International Conference on Image Processing (ICIP), 2011.
5. **Melih S. Aslan**, Eslam Mustafa,Hossam Abdelmunim, Ahmed Shalaby, Aly A. Farag, and Ben Arnold, "A novel probabilistic simultaneous segmentation and registration using level set," Proc. of 2011 IEEE International Conference on Image Processing (ICIP), 2011. 2011.
6. **Melih S. Aslan**, Aly A. Farag, Ben Arnold, and Ping Xiang, "Segmentation of vertebrae using level sets with expectation maximization algorithm," Proc. of 2011 IEEE International Symposium on Biomedical Imaging (ISBI), 2011.
7. **Melih S. Aslan**, Asem Ali, Aly A. Farag, Hossam Abdelmunim, Ben Arnold, and Ping Xiang, "A new segmentation and registration approach for vertebral body analysis," Proc. of 2011 IEEE International Symposium on Biomedical Imaging (ISBI), 2011.
8. **Melih S. Aslan**, Asem Ali, Ham Rara, and Aly A. Farag, "An Automated Vertebra Identification and Segmentation in CT Images," Proc. of 2010 IEEE International Conference on Image Processing (ICIP), pp. 233-236, 2010.
9. **Melih S. Aslan**, Asem Ali, Dongqing Chen, Ben Arnold, Aly A. Farag, and Ping Xiang, "3D Vertebrae Segmentation Using Graph Cuts With Shape Prior Constraints," Proc. of 2010 IEEE International Conference on Image Processing (ICIP), pp. 2193-2196, 2010.
10. **Melih S. Aslan**, Asem Ali, Aly A. Farag, Ham Rara, Ben Arnold, and Ping Xiang, "3D Vertebral Body Segmentation Using Shape Based Graph Cuts," Proceedings of the International Conference on Pattern Recognition (ICPR), pp. 3951-3954, 2010.

11. **Melih S. Aslan**, Asem Ali, Aly A. Farag, Ben Arnold, Dongqing Chen, and Ping Xiang, ”3D Vertebrae Segmentation in CT Images with Random Noises” Proceedings of the International Conference on Pattern Recognition (ICPR), pp.2290-2293, 2010.

12. **Melih S. Aslan**, Asem Ali, Ham Rara, Ben Arnold, Rachid Fahmi, Aly Farag, and Ping Xiang, ”A Novel, Fast, and Complete 3D Segmentation of Vertebral Bones” International Conference on Acoustic, Speech, and Signal Processing, ICASSP 2010, March 2010.

13. **Melih S. Aslan**, Aly A. Farag, Hossam Abdelmunim, and Mohamed A. El-Ghar, ”Assessment of kidney function using dynamic contrast enhanced MRI techniques,” Book Chapter of Biomedical Image Analysis and Machine Learning Technologies: Application and Techniques, Editors: Fabio Gonzalez and Eduardo Romero, 2009.

14. **Melih S. Aslan**, Asem Ali, Ben Arnold, Rachid Fahmi, Aly A. Farag, and Ping Xiang, ”Segmentation of trabecular bones from vertebral bodies in volumetric CT spine images,” Proc. of IEEE International Conference on Image Processing (ICIP’09),Cairo, Egypt, November 7-11, 2009.

15. **Melih S. Aslan**, Asem Ali, Ham Rara, Ben Arnold , Aly A. Farag, Rachid Fahmi, and Ping Xiang , ”A Novel 3D Segmentation of Vertebral Bones from Volumetric CT Images Using Graph Cuts,” 5th International Symposium on Visual Computing (ISVC-09) , Las Vegas, Neveda, Nov 30-Dec 2, 2009.

F. Reviewer

- Reviewer for the Journal of Computerized Medical Imaging and Graphics (2009-Present).
- Reviewer for the Journal of IET (2009-Present).
- Reviewer for the IEEE International Conference on Image Processing (2009-Present).
- Reviewer for the IEEE International Conference on Pattern Recognition (2012).

G. Software Programming

- Matlab
- C/C++
- AutoCad

H. Biography

Melih S. Aslan has been a PhD student and Research Assistant in ECE Department. He received the bachelor degree from Fatih University, Turkey in 2005

and the MS degree from University of South Alabama, USA in 2007. His area of expertise includes segmentation and registration methods based on the intensity, spatial interaction, and shape information. More specifically, his objective was to segment vertebral bodies of spine bones accurately to assist the bone mineral density measurements and fracture analysis. He developed a robust segmentation software for the vertebral bodies. He has over 14 publications in his PhD study.

I. Languages

- **Turkish** (Mother Tongue)
- **English** Fluent (Read / Write)

J. Membership

- Secretary of Turkish American Association of Kentucky, non-profit organization (2008-2012)
- Member of Institute of Electrical and Electronics Engineering (IEEE) Student Branch in Fatih University, Region 8 TURKEY Section, (2003-2005).
- Fatih University IEEE Student Branch, Vice President of Educational Programs, (2005).
- Fatih University IEEE Student Branch, Internet Seminars member of the coordinator team for IT Week in 2003, (2003).